Optimized Extraction of InSAR derived Along-Track Deformation during Glacial Surges

towards a better understanding of the Dyngjujökull glacier

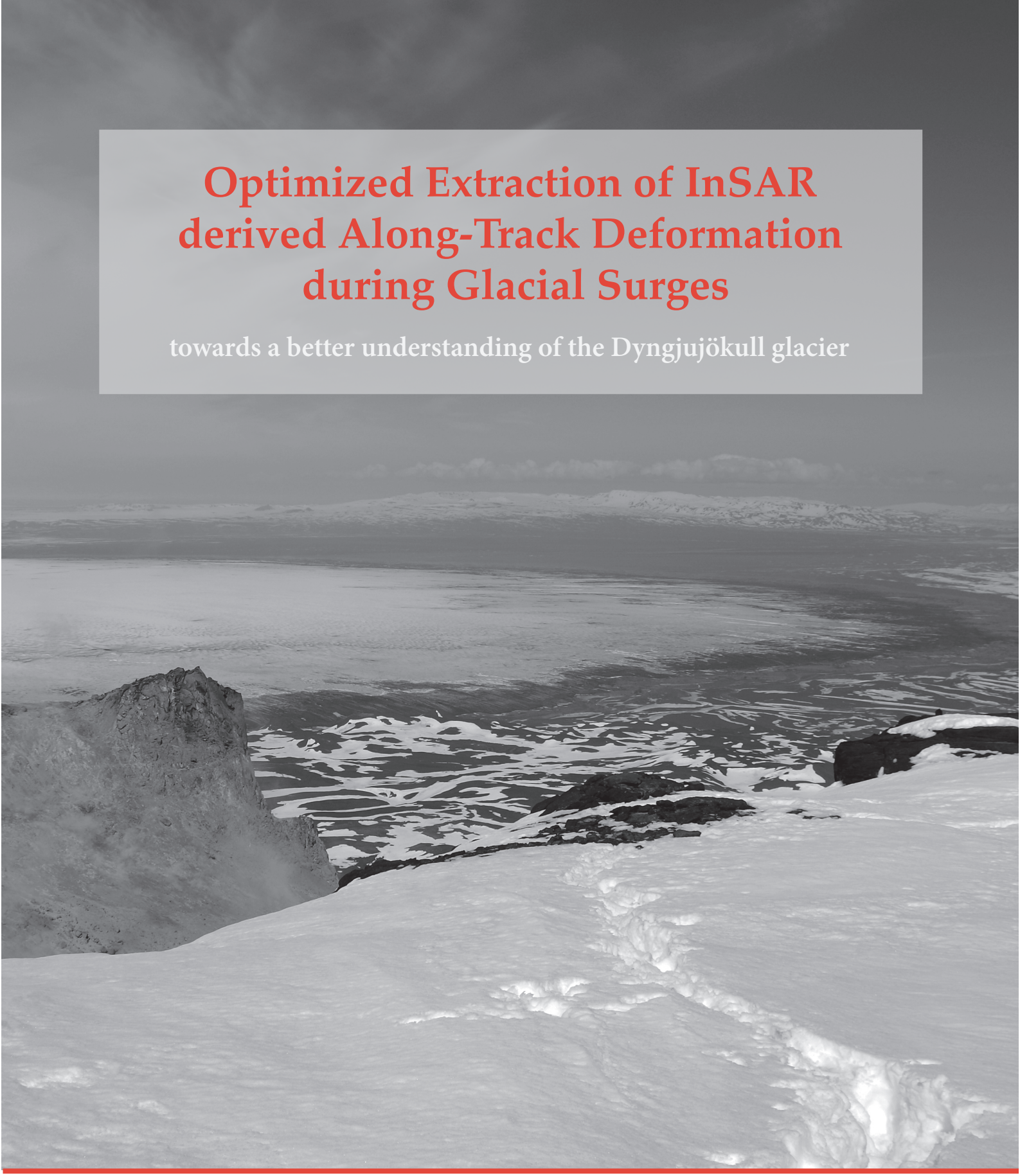

TU Delft Delft University of Technology

HÁSKÓLI ÍSLANDS

J.G. van Oostveen

January 2014

Dyngjujökull glacier seen from Kverkfjöll on June 6^{th}, 2013
Image courtesy of Hannah Reynolds

Optimized Extraction of InSAR derived Along-Track deformation during Glacial Surges

Towards a better understanding of the Dyngjujökull glacier in surge state

J.G. van Oostveen
Department of Geoscience and Remote Sensing
Delft University of Technology, The Netherlands

February 2014

A thesis submitted to the TU Delft
in partial fulfillment of the degree of Master of Science

I seemed to vow to myself that some day I would go to the region of ice and snow and go on and on till I came to one of the poles of the Earth, the end of the axis upon which this great round ball turns.

Ernest Shackleton

Preface

With this document I conclude my long journey at the Technical University in Delft, that led me to the area, glaciology and climate change, I found out to like most. In September 2004, I started of with Architecture to follow a childs dream to become an architect. After two years I switched to Maritime Technology to get myself more technically trained. By adding a minor in Computer Science, I completed the cocktail that eventually got me into the interfacultairy master program of Geomatics. This, apart from the fact that the program is terminated now and all the struggles that came with it, is one of the best decisions I have made during the last 9,5 years. With this, I conclude my student life in Delft as well. All the years I spent on rowing, travelling, organizing events make up almost a decade that is well worth remembering.

When I started off searching for a thesis subject, I only knew I wanted to do something with ice and preferably carry the project out abroad. Andy Hooper, at the time assistant professor at the Department of Geoscience and Remote Sensing, and who initially tried to convince me to take on a project on volcanology, knew a colleague at the glaciology department of the University of Iceland (Háskóli Íslands). They, Eyjólfur Magnússon and Andy, thought of a combined project of which the result is presented here. The technical and InSAR related part has been carried out in Delft, while the glaciology case-study element got the most attention during a nearly 4-month stay in Iceland. In this project several important research aspects are touched upon; from a theoretical framework, working with real data and designing tools to get around unexpected distortions in the outputs, to the simulation of synthetic data and the application of an external method to get to meaningful results.

This thesis would not have been a success without the help and guidance of my main supervisor Andy, now full professor at the School of the Earth and the Environment in Leeds. Plenty of thanks goes to Anneleen Oyen, my principal daily supervisor, for all the times I came knocking at her door with stupid questions, for her patience and overall assistance. I am grateful for the supervision of professor Ramon Hanssen and the opportunity to be a part of his research group for almost a year. Thanks as well to Prabu Dheenathayalan, my co-reader Tjeu Lemmens and my external examiner Bastiaan van Loenen for being a part of my committee. Many thanks to Eyfi for having me at the Institute of Earth Sciences, taking me on several field trips and for supervising me, both in Reykjavik as through lengthy Skype conversations.

Jelte van Oostveen
January 2014

Summary

During 1997-2000 Dyngjujökull, one of the major outlet glaciers of the main Icelandic ice cap Vatnajökull, surged. Water plays an important role in the dynamics of glaciers, and thus in the surging mechanism. To what extend it influences the specific movement of surging glaciers is still subject to debate. The prevailing hypothesis is that in the non-surging, or quiescent, period the meltwater is transported through a system of semi-circular tunnels. Whereas during surge events, a system of linked cavities forms in areas normally drained by a tunnel system. The alleged size of the cavities and the transportation streams impedes the easy transport of water. The high effective water pressure associated with it, forces the water to be distributed over the bed. This can facilitate basal sliding leading to increased velocities or surging behavior. Vertical movement of the glacier, which can be showed by deriving 3D flow fields, can point to water accumulation or depletion at the glacier bed, thereby confirming the existence of a mechanism of linked cavities.

The surge event was captured by ERS1 and 2 satellites flying in tandem mode, thereby enabling the use of InSAR to monitor the motion of the glacier using four interferometric pairs. A major limitation of InSAR is its sensitivity to deformation in only one dimension. As most geophysical phenomena, glacial flow is better characterized using geodetic data in three dimensions. One way to extend the capabilities of InSAR is the extraction of along-track deformation by means of methods often used to improve coregistration accuracy. The currently available methods that are assessed, both theoretically as through application on real data, include Multiple Aperture InSAR (MAI), Spectral Diversity (SD), both based on the spectral properties of the data, and spatial offset tracking methods like Coherent-, and Incoherent Cross Correlation (CCC and ICC respectively), both based on the apparent speckle noise. By searching for the most accurate method of extracting azimuthal deformation using InSAR, information is provided about the subglacial hydrology of a glacier in surge.

Results of a theoretical assessment, carried out by comparing measurement uncertainty formulas of the available methods, show that MAI is a particular instance of SD. Regarding the hypothesized similarity of CCC and SD, it is found that both are theoretically comparable, but not equal. CCC, reaching the Cramer Rao bound, performs a fraction better in terms of accuracy. ICC is theoretically worse than CCC and SD, because it only utilizes the amplitude of the signal. The variances of ICC and CCC vary by a factor of approximately 1.8 when the limit of the interferometric coherence approaches 1.

Results of the application of SD and ICC on real data show that the methods are comparable. Overall, SD leads to more accurate results in terms of standard deviations, however the differences are not as theoretically expected. This applicational discrepancy is believed to be caused by the appearance of features, which are tracked instead of the speckle pattern and thereby help to improve the cross correlation accuracy. The implementation of SD has advantages in speed

and pixel density, although unwrapping may be a problem when large deformation is expected. There, ICC may provide an alternative. An assessment of the equality of SD and CCC has not been made due to implementation limitations.

The outcomes of processing with SD show the presence of azimuthal shifts corresponding to TEC variations in the Earth's ionosphere, which partly distort the along-track deformation. To solve this, the nature of the signal is studied and a 2D FFT interpolation filter is designed taking the strong directionality of the streaks into account. The filter takes advantage of the low frequency character of the disturbances. Interpolation is applied to deforming- and low coherent areas, using Smart Pixel Selection. This involves identification of pixels to mask based on a coherence threshold in combination with a LOS phase gradient filter.

The corrected azimuth interferograms are used jointly with LOS interferometric data in a Markov Random Field method optimized by Simulated Annealing to derive 3D flow fields of the Dyngjujökull glacier in surge. This glaciology method is tested for its response behavior using synthetic data. The testing involved assessing the influence of different weighting factors in the optimization of the 3D flow outcomes and noise propagation, which is shown to be linear.

Derived 3D glacial flow fields demonstrate that all the observed motion can be explained by the mass continuity equation, indicating that the vertical component caused by a system of linked cavities is not large enough to be detected with this method. This does not mean that the presumed subglacial hydrologic system is not present. In the derived horizontal flow fields the movement of the glacier as a 'block' partly confirms the theory of interconnected cavities as the distribution of water across the bed enhances basal sliding in this particular way. Lastly, the obtained vertical motion rates correspond to the the total gain or loss estimated over the whole surge, if the derived vertical velocities would be extrapolated to the total duration of the event.

Table of Contents

List of Figures

List of Tables

Abbreviations

ASTER	Advanced Spaceborne Thermal Emission and Reflection Radiometer
CBF	Common Band Filter
CCC	Coherent Cross Correlation
DEM	Digital Elevation Model
DORIS	Delft Object-oriented Radar Interferometric Software
ERS	European Remote-Sensing Satellite
ESA	European Space Agency
FFT	Fast Fourier Transform
GIM	Global Ionopsheric Maps
HI	Háskóli Íslands
ICC	Incoherent Cross Correlation (speckle tracking)
InSAR	Interferometric SAR
IRF	Impulse Response Function
LOS	Line Of Sight
MAI	Multiple Aperture InSAR
MLE	Maximum Likelihood Estimator
MRF	Markov Random Field
PRF	Pulse Repetition Frequency
Radar	Radio Detection and Ranging
RAR	Real Aperture Radar
RMS	Root Mean Square
ROI_PAC	Repeat Orbit Interferometry PACkage
SAR	Synthetic Aperture Radar
SD	Spectral Diversity
SLC	Single Look Complex
SNAPHU	Statistical-cost, Network-flow Algorithm for Phase Unwrapping
SNR	Signal to Noise Ratio
StaMPS	Stanford Method for Persistant Scatterers
TEC	Total Electron Content

Part I

INTRODUCTION

Chapter 1

General introduction, problem statement and project setup

At present time about 10% of the Earths surface is covered with glacial ice, of which about 99% is located on the *ice sheets* in Antarctica and Greenland. Due to the inaccessibility of those regions, glacial monitoring and related research is often carried out in less remote areas like Iceland or Alaska. Glaciers are the worlds largest reservoir of fresh water, thus the importance of conducting research on them is obvious when it comes to water security and the potential of altering our global sea levels. More recently, the discussion on climate change has driven more attention to the field of glaciology as glaciers are a key and visible indicator of a changing environment. This makes ongoing research on glaciers, the way they move and the way they react to altering conditions on our planet more profound.

The size and often remote location of glaciers and ice caps compel glaciologists to use geodetic techniques that enable them to regularly monitor the whole area of interest. Spaceborne remote sensing platforms can provide the necessary spatial and temporal coverage to keep track of the advancement or retreat and speed of the glacier under investigation. Specifically satellite radar interferometry has provided researchers with an important tool to constrain motion of glaciers. This method was first applied by Goldstein et al. [1993] to monitor flow and grounding line positions of ice streams in Antarctica. Following the example set, many studies using *Interferometric SAR (InSAR)* have been carried out since then. Early adopters Joughin et al. [1996], Kwok and Fahnestock [1996] and Rignot [1996] are well known examples.

As one of the more accessible locations to study glaciers in every aspect, Iceland is currently covered by 11.400 km^2 of glaciers containing over 3.600 km^3 of ice. This corresponds to about 10% of the total area of Iceland, which in turn is roughly three times the size of The Netherlands. If all the ice, of which the oldest parts are about 800 years old, is melted away it would contribute to about 1 cm eustatic sea level rise. Since the end of the 19th century, Iceland's largest ice cap Vatnajökull (see Figure 1.1) decreased about 10% in total volume, corresponding to about 1 mm in global sea level rise, not taking local influences into account.

The main mechanism of ice discharge is through *outlet glaciers* on the edges of the ice cap. Twenty six Icelandic outlet glaciers are known to be of a surging type (Ingolfsson, 2013 - to be published). *Glacial surges* are periodical events

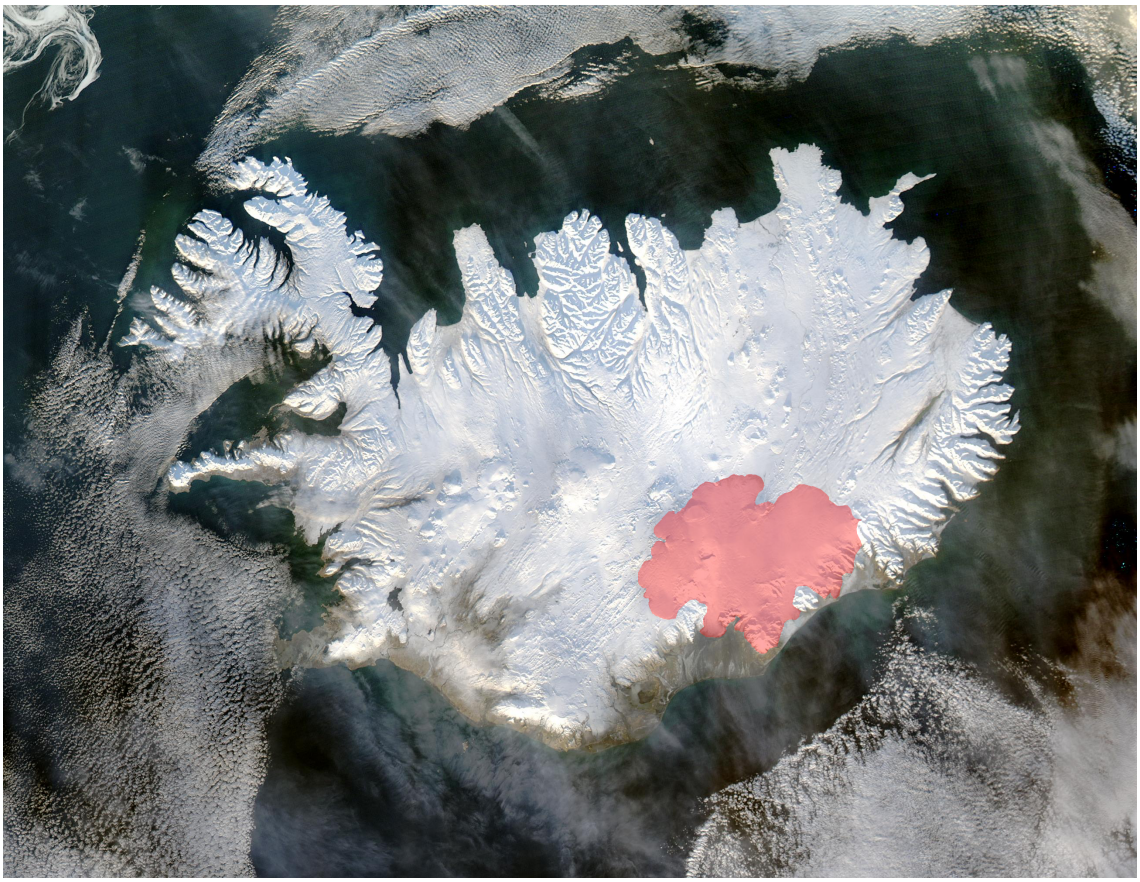

FIGURE 1.1: Iceland in wintertime, acquired by the Moderate Resolution Imaging Spectroradiometer (MODIS) on NASA's Terra satellite on January 28, 2004. In transparent red, the main ice cap Vatnajökull is displayed. Image courtesy of MODIS Rapid Response Project at NASA/GSFC.

where the glacier advances through rapid movement, up to 100 times faster than normal. About 10% of the total mass transport of the Icelandic ice caps to ablation areas during the 20th century is accounted for by surges of the principal outlet glaciers. Being one of the least understood physical phenomena within the field of glaciology, surges have to be studied more comprehensively to provide more reliable estimates of the future development of the ice caps. The last surge event in 1999-2000 of Dyngjujökull, a major outlet glacier located on the Northern side of Vatnajökull, is captured byEuropean Space Agency (ESA)'s European Remote-Sensing Satellite (ERS) 1 and ERS 2. The ERS 2 spacecraft was flying in tandem mode, i.e. it followed ERS 1 in the same trajectory with one day separation time. This short interval between the two acquisitions was needed to constrain the motions that varied from 1 up to $40\,\mathrm{m\,d^{-1}}$.

A major limitation of InSAR is its sensitivity to deformation in only one dimension, being the direction in which the radar pulse is send. However, most geophysical phenomena, including glacial flow, are better characterized using geodetic data in three dimensions. To overcome this drawback many solutions have been proposed in the past. Multiple satellite passes of the area of interest, both in ascending and descending orbit, can resolve the horizontal and vertical

deformation. With two of the necessary three motion components available, external constraints can be added to solve for the missing third. However, some areas are not recorded frequently from different satellite geometries in which case the aforementioned combination of tracks cannot be applied. Other techniques like the tracking of image features or *speckle* noise, can help to find deformation in *azimuth* direction. The latter one is better known as *offset tracking* or *(in)coherent cross correlation* (*ICC* and *CCC*). Offset tracking with an application on glaciology was first introduced by Gray and Mattar [1998]. Later this method has often been used to derive ice velocities, i.a. by Gray et al. [2001], Joughin [2002] and Rignot et al. [2008].

Next to offset tracking other methods are available that make use of the spectral properties of the data. Increased attention is drawn to these techniques after the introduction of *Multiple Aperture InSAR (MAI)* by Bechor and Zebker [2006] and the improvements suggested by i.a. Jung et al. [2009]. However, MAI turned out to be a special case of the previously introduced *Spectral Diversity (SD)* method [Scheiber and Moreira, 2000], specifically in azimuth direction. In this thesis, where MAI is not specifically discussed, the method is referred to as SD in azimuth.

The aforementioned methods are seemingly random applied to different datasets by different research groups. Consequently, several statements have been made about theoretical accuracy and the applicability of the available methods, but no clear overview has been presented so far.

In the following sections the motivation, objectives and setup of this research project are discussed. In Section 1.1 the main problems that are addressed in this thesis will be formally noted, including the overall research question. Section 1.2 and Section 1.3 discuss the flow of the project and the corresponding reading guidance to the remainder of this thesis. Jointly with the conclusions and recommendations (these can be found in Chapter 7 and Chapter 8 respectively), the purpose of this chapter is to give a complete overview of the executed work.

1.1 Problem statement

A full problem statement is covered by the motivation to carry out certain research and the questions that lead to the execution of the research. Subsection 1.1.1 encompasses the discussion of the current scientific challenges and corresponding research objectives that form the basis for this project. To frame the scope of the work, a research question and associated subquestions are introduced in Subsection 1.1.2.

1.1.1 Motivation and objectives

Based on the rationale introduced in the leading part of this chapter the motives for conducting this research can be listed. Firstly, this overview of gaps in current research helps to demarcate the boundaries of the project. Secondly, this synopsis can also help to focus on the parts that are important in order to lead to useful conclusions.

- Not everyone within in the InSAR community is convinced that there is a clear difference between the spectral (i.a. MAI, SD) and spatial cross-correlation methods (ICC, CCC) available to extract along track deformation from a single InSAR pair. The discussion is ongoing and no clear resolution is published yet, albeit several publications handle the derivation of accuracies for the different methods. The alleged similarity between the spatial cross correlation- and spectral methods is linked to the theoretical accuracy that can be reached with the different methods. To what extent the methods are the same or comparable, both theoretically as well as application-wise, is one of the main issues that will be addressed in this thesis.
- Water plays an important role in the dynamics of glaciers, and thus in the surging mechanism. To what extend it influences the specific movement of surging glaciers is still subject to debate. The prevailing hypothesis is that in the non-surging, or quiescent, period the meltwater is transported through a system of semi-circular tunnels. Whereas during surge events, a system of interconnected cavities forms in areas normally drained by a tunnel system [Björnsson, 1998], [Cuffey and Paterson, 2010]. The alleged size of the cavities and the transportation streams impedes the easy transport of water. This can facilitate basal sliding, leading to increased velocities or surging behavior. Information about vertical movement can point to water accumulation or depletion. In an interferogram these areas are often visible as *bulls-eye* patterns. Since the Dyngjujökull glacier is only sparsely covered by different satellite acquisitions and because its main orientation is to the North, there is limited data available using conventional InSAR. Therefore, the extraction of along track deformation from a single interferometric pair is important to confine the number of assumptions that have to be made when deriving 3D flow fields.

Based on the preceding motivation two research goals are set for this project:

- Optimize the extraction of deformation in azimuth direction using InSAR data
- Increase the understanding of surging glaciers

This project seeks to find the best estimate for each point on the surging glacier, i.e. the optimal approach, which can result in a combination or adaption of existing methods. To resolve this, a similarity assessment between spectral and spatial cross-correlation methods will be carried out, both theoretically as through application on real data. The second goal is focused on the extraction of information to gain knowledge of the vertical ice motions and thereby increasing understanding of glacier surge dynamics.

1.1.2 Research question

The problem statements and corresponding objectives can be translated into the following general research question:

What is the most accurate way to extract azimuthal deformation using InSAR data to increase understanding of a glacier in surge state?

This general research question can be subdivided into several subquestions, grouped by common subjects. First the general subject of extraction of along-track deformation using InSAR data will be treated:

- *What are currently used methods to obtain azimuthal deformation (with the object(s) of interest, glaciers, in mind)?*
- *What are their drawbacks/characteristics?*
- *What are the assumptions that support these methods?*
- *To what extent are spatial offset tracking and spectral methods theoretically different?*
- *When are the results of SD and spatial offset tracking comparable?*

In order to assess the possible improvements of the current methods it is necessary to investigate the characteristics and the assumptions supporting each method by means of literature study. Furthermore the benefits and shortcomings of each method need to be investigated. The unresolved issue of a potential similarity between SD and offset tracking is also addressed, both theoretically and methodologically.

To address the glaciology part of this thesis, the focus will be on the background of surging glaciers; the creation of 3D flow fields using InSAR and the extra understanding of glacial surging behavior using the additional information about vertical ice movements. To be able to deduce information from the processed InSAR data, an existing method that uses a Markov Random Field (MRF), or a set of Random Vectors in Delft terminology, algorithm with Simulated Annealing will be utilized [Gudmundsson, 2002], [Magnússon, 2008]. In MRF an image is

interpreted as a network of random variables, where the value of each pixel in an image is only dependent on its nearest neighbors. To find the optimal value for each pixel, i.e. a global optimum for given functions and boundary conditions, Simulated Annealing is implemented. This relates to the heating and cooling of a system to derive a minimum energy level contained in that system, corresponding to an optimal solution. The following questions are composed with this method for deriving 3D flow fields in mind.

- *What is the current state of research on the surge of Dyngjujökul and surging glaciers in general?*
- *What are the different approaches to obtain 3D ice movements of (surging) glaciers?*
- *How do the current methods need to be adapted to derive 3D flow fields using only one InSAR pair?*
- *What extra information would the addition of an azimuthal component to the 3D flow derivation yield?*

By answering these questions the surge of Dyngjujökull will be better understood. Improvements of the current method to derive 3D flow fields, by adding the along-track component to the input data, will yield the possibility of application to other glacial events.

1.2 Project setup

The project is divided into three different phases, which are discussed below and visible in Figure 1.2.

1. *Phase 1: introductory part*: In this stage the focus will be on creating a solid background necessary to carry out this research project. This will mainly be done by means of literature study, gathering acquired data and getting acquainted with the processing methodologies.
2. *Phase 2: theoretical and applicational framework*: The theoretical similarity assessment of azimuthal extraction methods will be addressed. The outcomes of this will be converted to application of the methods on the available real data. Also, this leaves room for potential improvement of these methods in any form.
3. *Phase 3: glaciology*: This phase will be used to relate the work of the previous phases to the work that is conducted in Iceland. Also, the focus will be on interpreting the different azimuth offset images, the creation of 3D velocity fields and on learning about glaciology and corresponding research.

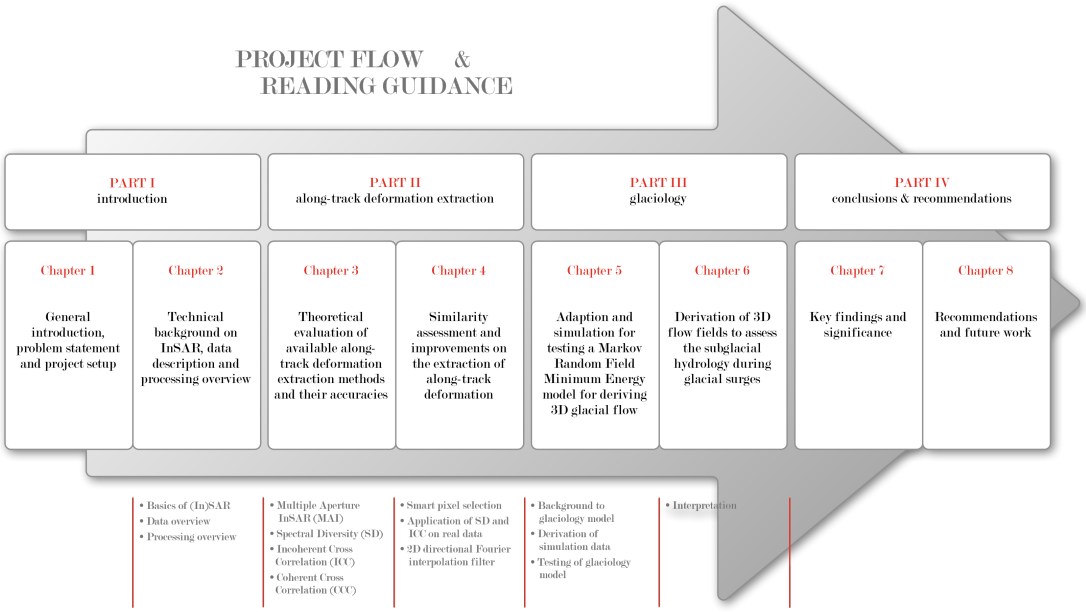

FIGURE 1.2: The flow of the project as discussed in Section 1.2 is translated into a flow diagram that shows the general setup of the project. The structure of the thesis, as denoted in Section 1.3, is clearly visible. This diagram supports the reading guidance and the Table of Contents. In the upper row the different parts (I-IV) are visible, followed by the chapter titles in the lower row. Below the arrow some keywords of subjects that are covered in the different chapters are listed.

1.3 Reading guidance

This thesis is divided into several parts of which Part I, II and III roughly correspond to the project phases discussed in Section 1.2. An introductory part, Part I, comprises this chapter and the relevant background to the main geodetic technique and the used data. The latter is discussed in Chapter 2 (p.11). Part II covers a theoretical assessment of available along-track deformation extraction methods and their accuracies in Chapter 3 (p.27) and an application of these techniques including some improvements in Chapter 4 (p.41). The glaciology aspect of this work is can be found in Part III. The method for deriving 3D glacial flow fields is tested using simulated data in Chapter 5 (p.60). Subsequently, outcomes of this model using real input data are presented and discussed in Chapter 6 (p.72). The final part summarizes the key findings and highlights the significance of this work in Chapter 7 (p.92). The final Chapter 8 (p.98) gives an overview of possible future work. All parts, corresponding chapter titles and some keywords are visible in Figure 1.2.

* * *

Chapter 2

Technical background on InSAR, data description and processing overview

This chapter serves as a reference to the main techniques, the data and the corresponding processes used in this thesis. The basic principles of radar, SAR and InSAR are discussed in Section 2.1. This is followed by an overview of data availability in Section 2.2 and the processing flow as it has been used throughout this project in Section 2.3.

2.1 Radar system theory

Radio Detection and Ranging (Radar) is a method, system or technique that uses electromagnetic radiation to, inter alia, detect, find or range objects. Radar secretly developed during the second world war and is used ever since in a wide range of applications varying from antimissile systems and astronomy to ocean surveillance systems. A short introduction to the particular application for geodesic purposes is denoted in this section. More specifically, Subsection 2.1.1 will introduce the concept of Synthetic Aperture Radar (SAR) followed by the basics of Interferometric SAR (InSAR) in Subsection 2.1.3. The latter one being the principle technique used in this thesis.

2.1.1 Real and Synthetic Aperture Radar

Radar works by the principle of transmitting microwave radio pulses to an object and subsequently measuring the two-way travel time and the strength, or *intensity* of the returned signal. This radar return is called the *echo* or *backscatter* and gives valuable information on e.g. the shape and the roughness of the surface [Hanssen, 2001]. When mounted to a space- or airborne platform radar systems can be used to map these scattering characteristics of the Earth's surface with a regular repetition. Typically, radar systems use X-band (8 to 12 GHz) , C-band (4 to 8 GHz) and L-band (1 to 2 GHz) for *imaging* purposes. Their respective wavelengths are approximately 3 cm, 5.6 cm and 24 cm. The choice of frequency band is dependent on the desired application. A larger wavelength results in an increasing penetration depth of the surface, which can be useful when areas with

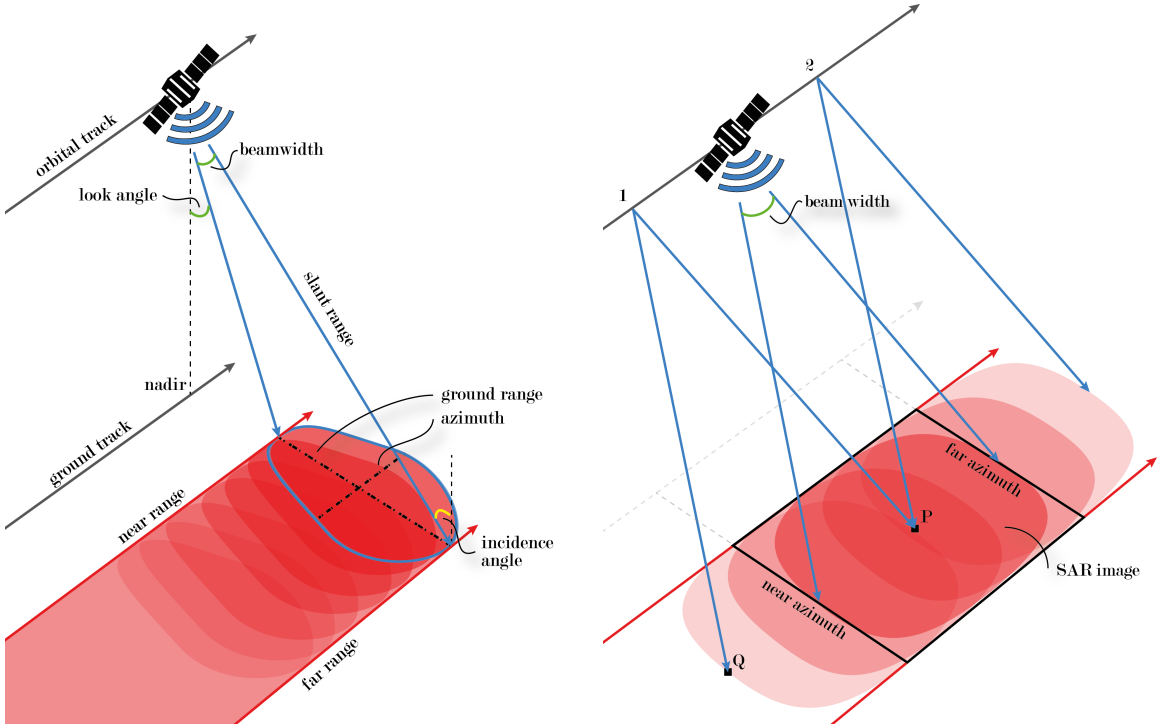

FIGURE 2.1: **Left**: a schematic overview of the imaging geometry of a side looking SAR mounted on a satellite. The radar illuminates a swath (colored in red) parallel to the ground track. **Right**: The SAR principle shown schematically. The echoes from the first pulse until the last pulse that hit point *P* are recorded to create an artificially long antenna.

rapidly changing surface conditions are investigated. This penetration ability is also applicable to clouds, making the method weather independent.

The part of the Earth that is illuminated by the transmitted radar beam is called the *swath*. Within that beam footprint, the direction in which the beam is send is known as the *Line Of Sight (LOS)* direction. The often side-looking viewing geometry causes the beam to be emitted in the across-track, or *range* direction, perpendicular to the flight direction of the platform. In range, a differentiation has to be made between ground range and slant range. The former is the across-track range distance. The latter being the distance of a point towards the satellite. The other direction, along-track, is referred to as *azimuth*. All variables mentioned in this paragraph are visible in Figure 2.1.

Real Aperture Radar (RAR) and Synthetic Aperture Radar (SAR) are examples of imaging radars, both working with a single antenna. To be able to send pulses and receive echoes with one antenna, pulses are not transmitted continuously. During the time that there is no transmittance, echoes can be received. The frequency by which a pulse is transmitted is called the Pulse Repetition Frequency (PRF). The pulse duration (or pulse length) τ is a direct measure for the slant range resolution. The minimum separation distance to distinguish two objects equals the distance the signal can travel within its pulse length. For example, in

case of ERS, $\tau = 37\,\text{ms}$. This leads to a minimum separation distance of 5.5 km according to

$$\Delta_r = \frac{c\tau}{2} = \frac{c}{2B} \tag{2.1}$$

where c equals the speed of light and B equals the signal bandwidth. To resolve this highly unpractical slant range resolution a *chirp* is modulated (coded) onto the pulse. A chirp is a signal where the frequency increases with time over the pulse length. The chirp waveform is compressed and then transmitted. When received back, the signal is compared with a replica of the transmitted chirp. By applying the pulse compression technique, the pulse length is now inversely proportional to the bandwidth of the chirp. Taking the example of ERS, the chirp bandwidth B equals (15.5 MHz). Consequently, the slant range resolution improved to 9.6 m. The result of this process is the transmittance of a long pulse that has a bandwidth corresponding to a short pulse. This corresponds to better signal reception and a fine range resolution respectively.

In azimuth the resolution Δ_a is dependent on the beam width β of the pulse. The beam width is determined by the ratio of the wavelength over the antenna length:

$$\beta_a = \frac{\lambda}{L} \tag{2.2}$$

The aforementioned ERS satellite uses C-band, has an antenna length of 10 m and is flying at a height of 850 km. With Equation 2.2 a beam angle of 0.005 rad is obtained. If ERS would be a RAR system the resulting azimuth ground resolution would end up being larger than 4 km. This is obviously too coarse for most applications. To improve this resolution a kilometer-long physical antenna has to be created, which is practically impossible.

A signal processing advancement makes it possible to combine the echoes of all the pulses transmitted when the object of interest is within the swath of the moving satellite. By combining or *synthesizing* the different echoes, an artificially long antenna is created. During the entire time of illumination the relative velocity of the object with respect to the antenna changes. This causes a *Doppler*-like effect [Hanssen, 2001]. The Doppler structure of the echoes is stored and later used in SAR processing to *focus* the data. The azimuth resolution is now dependent on the azimuth Doppler bandwidth and the velocity of the satellite. It can be shown that their ratio is equal to the length of the physical antenna L divided by 2:

$$\Delta_a = \frac{L}{2} \tag{2.3}$$

The azimuth resolution improves almost three orders of magnitude. To complete the example of ERS, the new along-track resolution is 5 m. This technique is known as Synthetic Aperture Radar (SAR) and is used as the basic idea behind the method described in Subsection 2.1.3.

2.1.2 On the Doppler bandwidth and azimuth resolution

The basic principle of SAR is discussed in the last paragraph of Subsection 2.1.1. In this subsection the construction of the signal and its properties are discussed in more detail.

In azimuth, the beam has a width denoted by β_a. It conceivable that it is impossible to differentiate between the echoes returning from the same distance when only one pulse is send. Take point P in the right image of Figure 2.1. If the backscatter of the pulse at instant 1 is examined, the echoes of point P, *far azimuth* and the identical point Q, *near azimuth*, have the same travel time and thus arrive at the same moment at the antenna. In this case, there is no possibility to know that there are two scatterers responsible for the received signal.

As discussed before, the platforms velocity with respect to the scatterer (point P) alters with every pulse. The frequency of the echo changes depending on the position of the object with respect to the satellite. That Doppler frequency f_D, for a target approaching with ground velocity $v_{s/c}$ in SAR geometry is denoted according to Hanssen [2001] as follows:

$$f_D = \frac{2v_{s/c}}{\lambda} \sin\alpha_s \sin\theta \tag{2.4}$$

where θ equals the look angle (see Figure 2.1) and $\lambda = 5.656\,\text{cm}$. The introduction of α_s is treated below. According to Equation 2.4, the Doppler frequency gets smaller as the satellite approaches point P perpendicular and grows again when the satellite moves away from the point. Synthesizing the echoes of the different pulses as long as point P is within the illuminated area (between instant 1 and 2), creates a Doppler history of point P. Thus, the pixel of point P is viewed from different angles at different times, making the point distinguishable from point Q. This can be easily understood by imagining that every pulse is equal to one azimuth pixel of an azimuth line in the image denoted by the black box in Figure 2.1b. The history of varying Doppler frequencies when the object passes through the synthesized beam is called the *Doppler bandwidth*, B_a and is defined as:

$$B_a = \frac{2\beta_a v_{s/c}}{\lambda} \tag{2.5}$$

In case of ERS the Doppler bandwidth is close to 1377 Hz. An example of an azimuth frequency spectrum can be seen in Figure 2.2. The spectrum shows a sinus cardinalis, or *sinc*, as a result of the antenna pattern. The empty region is set to zero to avoid aliasing when complex multiplying two SAR images. This *oversampling* is the ratio between the PRF and the Doppler bandwidth:

$$\frac{PRF}{B_a} \approx 1.22 \tag{2.6}$$

When to look direction is perpendicular to the satellites flight directory, the Doppler frequency is zero. This is commonly referred to as $f_D = 0 = f_{D0}$, the *zero-Doppler* frequency. One would expect that the spectrum is symmetrical with

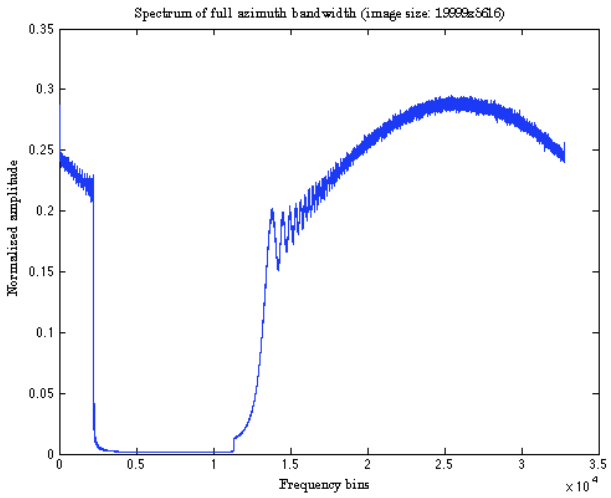

FIGURE 2.2: The amplitude of the average of the spectra an entire image of 19999 azimuth lines. This graph shows the azimuth Doppler bandwidth frequencies. The frequencies are divided over 32768 bins, a number larger than the amount of azimuth lines. Note that the horizontal axis does not show the sampling frequency (or PRF). Sidelobes caused by the antenna pattern are clearly visible close to the 15000 frequency bin. The Doppler frequency f_{Dc} would be expected to lie where the amplitude of the spectrum is the highest. However, the spectrum is shifted due to the squint angle.

respect to the zero-Doppler, but it is centered around f_{Dc}, the *Doppler centroid* of the beam. During the recording of the echoes from consecutive pulses, the Earth rotates with respect to the platform causing a shift in the recordings. The antenna of ERS can be electronically adjusted to compensate for this *Doppler shift*, but there will always be a slight *squint angle* α_s, steering the antenna pattern away from the zero-Doppler.

According to Equation 2.6 the sampling in azimuth is defined by the PRF. If the PRF equals the azimuth bandwidth, then the pixelspacing is equal to the azimuth resolution. But due to the requirement of oversampling the pixelspacing, or *posting*, is 4.4905 m, compared to Δ_a of $\pm$ 5.5 m.

The azimuth bandwidth and corresponding formulas are of major significance in the discussion on split-bandwidth methods to derive along-track deformation, as will be dealt with in Chapter 3.

2.1.3 Radar Interferometry

If two SAR images are available, separated in either space or time, their phase difference can provide information about the surface topography or change in the surface topography. The technique that exploits these differential phases is known as Interferometric SAR (InSAR). The result of the implementation of the InSAR procedure is an *interferogram*, characterized by wrapped (in modulo 2π) phase differences called *fringes*. Some preprocessing is required before an

interferogram is obtained. The image that is taken at a more recent point in time is denoted as *slave*. The oldest image is commonly referred to the *master*. To obtain the phase differences, the slave pixels have to correspond with the same pixels in the master image. The subpixel estimation of the spatial shifts between the images is called *coregistration*. After several coregistration steps the slave is resampled onto the master. By complex multiplication of the master and the slave a final interferogram is obtained. Residual phases as the topography of the region and orbital effects that would be present if the Earth is assumed to match the reference ellipsoid, have to be removed. The fringes in the final interferogram can then be unwrapped to obtain the desired deformation signal. In case of ERS data, one fringe in range direction corresponds to approximately 2.83 cm LOS displacement.

The wave equation corresponding to the signal emitted by a SAR satellite has a complex character. It consists of an amplitude ($|y_1|$) and a phase (ϕ_1) term:

$$y_1 = |y_1| exp(j\phi_1) \tag{2.7}$$

The preservation of both the phase and the amplitude of the signal, makes SAR a coherent system. Generally, *coherence* γ serves a measure for the quality of the interferometric phase. Two signals are coherent if there exists a fixed relation between the phase of each separate signal. Zebker and Villasenor [1992] denoted several *decorrelation* sources that have an effect on the coherence of an interferogram. *Geometrical* decorrelation is coupled to physical distance between the acquisition position of the master and the slave. The larger this *perpendicular baseline*, the more loss of coherence. During the time separating the two acquisitions, the terrain can change physically. This *temporal* decorrelation can for example be caused by snowfall, canopy growth or movement of the ground.

The 'salt-and-pepper' image noise apparent in SAR images is commonly referred to as *speckle* [Rees, 2001]. The energy of the individual scatterers within a resolution cel is summed coherently. Dependent on apparent constructive or destructive interference within the pixel, this summation is either high or low. By multilooking (averaging of independent pixels) or filtering processes, this speckle pattern is often reduced.

An other major limitation of InSAR is the insensitivity to motion in the along-track direction of the satellite. One way to partially overcome this is by combining data from multiple look angles (e.g. using data from ascending and descending orbits, variable beam angles or satellites that look both left and right) [Wright, 2004]. However, the instruments on board of current satellites are not capable of providing the necessary technical conditions to obtain two sided image acquisition. Besides this practical limitation, to use a combination of ascending and descending tracks often good coverage of the areas of interest is required, which is not always the case.

More in-depth information about radar interferometry can be found in e.g. Bamler and Hartl [1998] and Hanssen [2001].

2.2 Data availability

The Dyngjujökull surge is covered by four different interferometric pairs captured by the ERS 1 and 2 satellites. From the launch of ERS 2 in 1995 to the failure of ERS 1 in 2000, these were flying regularly in tandem mode (following the same orbital track) with a temporal baseline of 1 day. The normal revisit time of both ERS satellites was 35 days. To be able to process these SAR images, an external Digital Elevation Model (DEM) is necessary. This section will give an overview of the available SAR data in Subsection 2.2.1 and an explanation on the construction of the external DEM in Subsection 2.2.2.

2.2.1 Data overview

Three scenes cover the beginning of the surge period; January 6/7 1999 and February 8/9 1999 (both ascending, track 44) and February 27/28 1999 (the only descending scene that is available). The fourth pair, January 26/27 2000, covers the end of the event, where a fully developed surge can be clearly seen. The data used in this project is available in two different levels of processing, e.g. level 0 products: raw data in Envisat format (.e1, .e2) and level 1 products: Single Look Complex (SLC) data in .CEOS format (.001). Both raw and SLC images are used in the processing as discussed in Section 2.3.

SLC data
In ascending orbit the area of interest is split in two frames: 1305 and 1287, resulting in 12 images. The descending scene covers the full length of the glacier, but the glacier is not fully covered in width, see Figure 2.3. To be able to use this pair, the images have to be processed in raw format, because the width of the SLC images is often limited due to the focussing procedure. The 14 SLC images (7 image pairs) that are used in this study are presented in Table 2.1.

Some SLC's were made available by Thomas Nagler from ENVEO IT GmbH in Innsbruck. However, all data is reordered from ESA (project code NLHR2469 - C1F.3538) to guarantee homogeneity in processed results. The ENVEO data was processes to SLC using different settings than the basic ESA .CEOS format. This made a combined use of ENVEO and .CEOS data impossible.

Raw-data
As discussed before, the SLC images do not fully cover the area of interest. Since 2006, ESA also offers ERS SAR images in raw Envisat format. This raw format contains the whole swath-width of 5616 pixels. As an extra advantage, sensing start- and stop times can be chosen manually when the data is ordered. Thus, by processing raw data, the aforementioned problems with SLC imagery are resolved. The 8 raw-images (4 image pairs) that are used in this study are presented in Figure 2.4 and the corresponding data can be seen in Table 2.2.

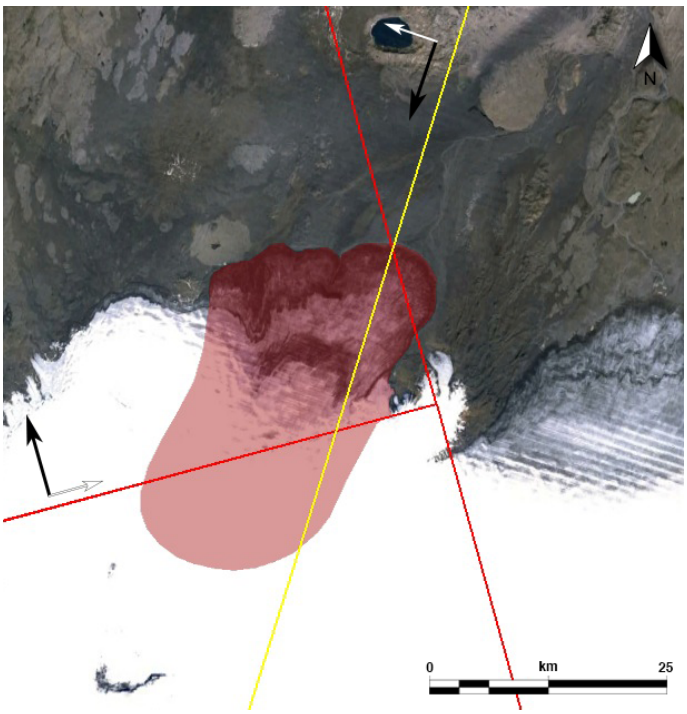

Figure 2.3: The reduced width of SLC's processed by the ESA has its limitations on the usability of the images. The glacier is, both in the ascending (red) and descending (yellow) case, partly outside of the images. Next to the inconvenient swath width, the glacier is covered by two seperate SLC's when the satellite is in ascending orbit. This results in twice as much interferometric processing. For these two reasons the data is re-ordered in raw ERS-Enivsat format.

		Ascending / descending	PP baseline (SLC track 1287)	PP baseline (SLC track 1305)
Pair 1:	6 January 1999	asc.	124 [m]	113 [m]
	7 January 1999	asc.		
Pair 2:	10 February 1999	asc.	113 [m]	109 [m]
	11 February 1999	asc.		
Pair 3:	27 February 1999	desc.	104 [m]	-
	28 February 1999	desc.		
Pair 4:	26 January 2000	asc.	73 [m]	70 [m]
	27 January 2000	asc.		

Table 2.1: An overview of available SLC data is presented in this table. Each first acquisition is taken by ERS1, followed by an aquisition of ERS2 the next day. The perpendicular (PP) baseline information is given as well. The perpendicular baselines for ascending scenes are taken from Fischer et al. [2003]. The information for the descending pair is derived during processing of the SLC data.

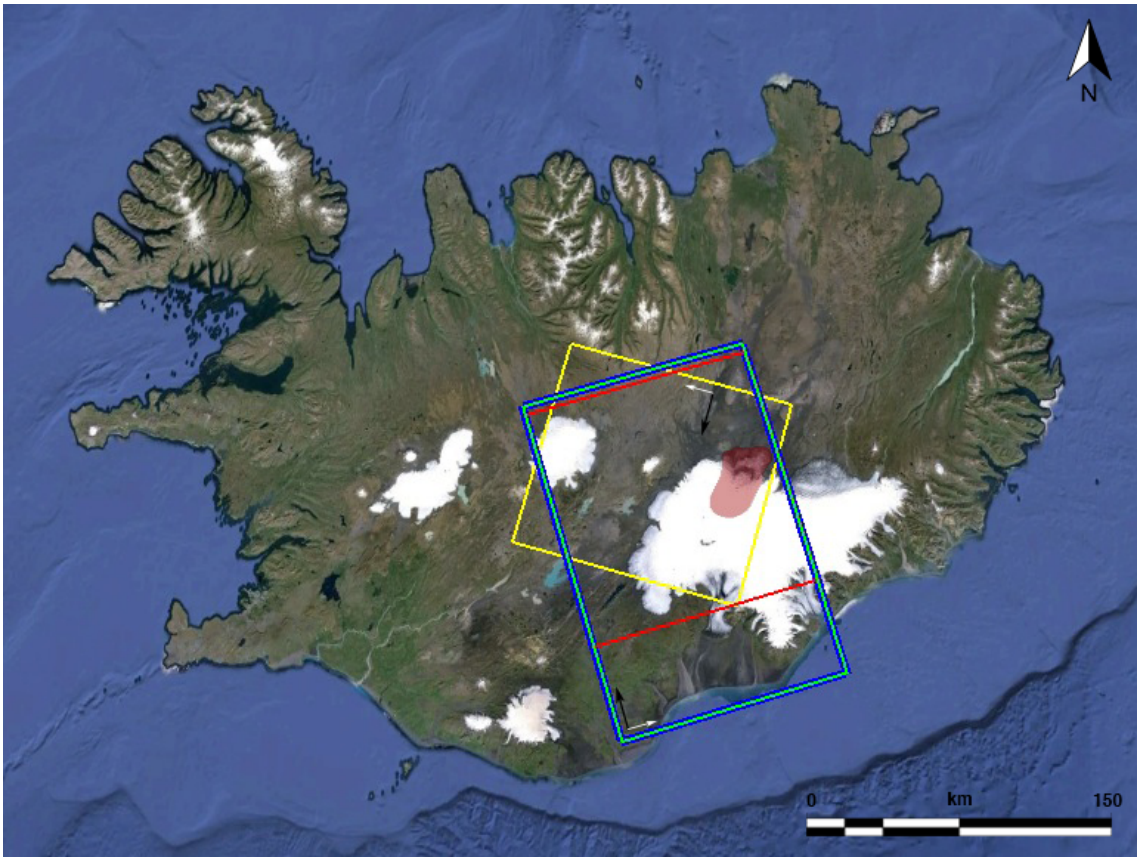

FIGURE 2.4: Available raw images wrapped on a Google Earth map of Iceland. The red semi-transparant area represents the cut-out that has to be made to obtain the region of interest. Three ascending pairs are used (colors corresponding to the frames displayed in the figure): 6-7 January 1999, 10-11 February 1999 and 26-27 January 2000 and one descending pair: 27-28 February 1999.

		Ascending / descending	Heading w.r.t. N.	Perpendicular Baseline
Pair 1:	6 January 1999	asc.	-21.16 °	118 [m]
	7 January 1999	asc.		
Pair 2:	10 February 1999	asc.	-21.02 °	103 [m]
	11 February 1999	asc.		
Pair 3:	27 February 1999	desc.	-158.72 °	105 [m]
	28 February 1999	desc.		
Pair 4:	26 January 2000	asc.	-21.04 °	71 [m]
	27 January 2000	asc.		

TABLE 2.2: An overview of available raw data is presented in this table. Each first acquisition is taken by ERS1, followed by an acquisition of ERS2 the next day. The heading of the interferometric pair and perpendicular baseline information are given as well. The information is derived during processing of the raw data.

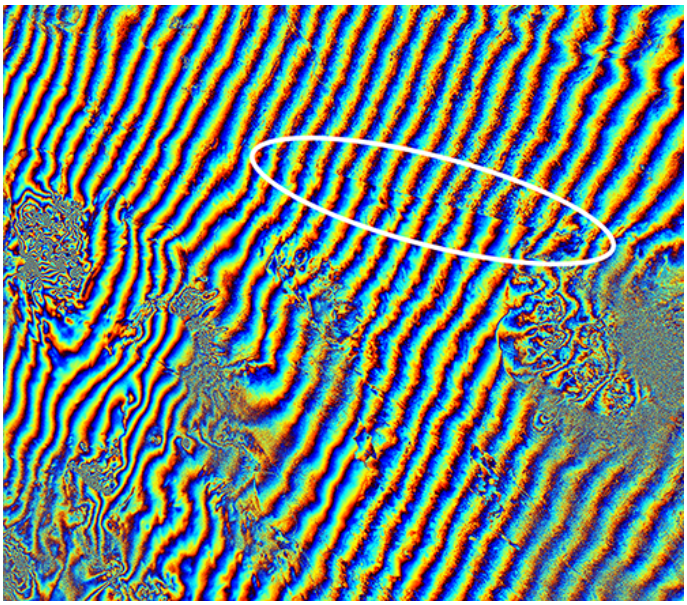

Figure 2.5: Non-geocoded interferogram (from the 27-28 February 1999 pair) where a phase ramp due to processing of raw data with SLC statevectors is visible. The phase ramp is removed by counting the fringes and subsequently subtracting a corresponding amount of phase from each individual pixel. The white circle emphasizes a phase offset visible due to processing with a DEM which is the result of a combination of the ASTER-DEM V2 and the 2000-DEM from HI. This phase offset is not corrected since it is outside of the area of interest.

Availability of unwrapped interferograms
All scenes, with exception of the descending pair, have been unwrapped before [Magnússon, 2008]. The data used for deriving these interferograms are SLC images, with the limitations as discussed in Subsection 2.3.2. The main subject of this thesis results in a limited focus on deriving new LOS interferograms. For that reason only the 27-28 February 1999 interferogram is produced and unwrapped, see Section 6.3. The remaining three interferograms (see Appendix A) are provided by E. Magnússon (Háskóli Íslands (HI)).

2.2.2 Digital Elevation Models

Two DEM's (UTM28) in geoid height will be used during the interferometric processing. Both have an accuracy of tens of meters in the surging areas due to elevation changes caused by the surge [Pálsson et al., 2002]. The first DEM was created in 1999, at the beginning of the surge event. When the surge was fully developed in 2000, another DEM was produced. Both DEM's are limited to the boundaries of the ice cap. To be used in the processing chain, the boundaries have to be extended to meet the edges of the SAR scenes. By merging Advanced Spaceborne Thermal Emission and Reflection Radiometer (ASTER)-DEM V2 [NASA Land Processes Distributed Active Archive Center (LP DAAC), 2001] and the aforementioned DEM's, full coverage of the scenes is obtained, under the assumption that the areas outside of the glacier and ice cap have not changed significantly from 1999 to 2011. An interferogram showing a small phase offset due to the merging process is visible in Figure 2.5. The phase shift is not removed because it is only apparent outside of the area of interest.

2.3 Data processing

Data processing is done with Stanford Method for Persistant Scatterers (StaMPS) [Hooper et al., 2012], Repeat Orbit Interferometry PACkage (ROI_PAC) [Rosen et al., 2004] and Delft Object-oriented Radar Interferometric Software (DORIS) [Kampes et al., 2003]. A standalone version of DORIS can only work with SLC data as input. Since the initially ordered SLC data has some width-limitations (as can be seen in Figure 2.3), the scenes are reordered in raw format. To get imagery focussed in zero-Doppler ROI_PAC is used, after which DORIS served as the processing engine for the remaining steps. StaMPS serves as a top shell to be able to work with both interferometric processors. The processing flows to get to offset tracking results, normal LOS and SD interferograms are displayed and discussed in Subsection 2.3.1, followed by explanations of the improvements on the processing of raw data in Subsection 2.3.2.

2.3.1 Processing flows

An overview of the main processing flow is visible in Figure 2.6. After focussing the raw input data the standard interferometric processing is carried out until the slave is resampled onto the master. A key step is the azimuth filtering, which selects the common azimuth bandwidth between the master and slave. Non-overlapping parts of the spectrum are discarded from further processing. The quality of both the SD interferogram as well as the offset tracking result clearly benefit from running this azimuth filtering step. After filtering the master and slave for their common Doppler bandwidth, for an accurate determination of the offsets by means of SD or speckle tracking, the coregistration parameters have to be determined without the deforming regions included. This is done by choosing the coordinates of the coregistration windows manually. Inter alia for this purpose, a masking procedure is created, see Section 4.2.

From the resampling on, three different routes can be taken. The common route is the creation of LOS interferograms by complex multiplication of the master and its resampled slave, as described in the DORIS manual [, DEOS].

The second route is to 'trick' DORIS to do another fine coregistration to obtain residual offsets. This is done by updating the *slave.res* logfile. The values corresponding to the cropped image have to be replaced by the values corresponding to the resampled image. This method is better known as Incoherent Cross Correlation (speckle tracking) (ICC) or speckle tracking. From the obtained pixel patch shifts atmospheric noise or deformation can be estimated, as can be seen in Chapter 4.

The third possibility is to split the azimuth bandwidth of the master and the resampled slave into two by means of a band pass filter. From the resulting four images a forward- and backward looking interferogram can be created. This is done by complex multiplication of the overlapping master- and slave subbands.

A final SD interferogram is found by subtraction of the backward looking interferogram from the forward looking interferogram.

For more details on ICC and SD, see Chapter 3. For an overview of DORIS input cards for general processing and speckle tracking, the reader is referred to Appendix B and C respectively.

2.3.2 Improvements on raw processing

Due to a failure of the ERS-1 Precise Range and Range-Rate Equipment (PRARE) system and poor tracking using Satellite Laser Ranging (SLR), external orbits are not available for ERS-1 after 1996. The raw data delivered by ESA is offered in Envisat format. Only one orbit statevector is included in the header of the datafile, which means that no external orbit files are available to focus the raw data to SLC images. To bypass this problem the five orbit statevectors included in the SLC (.CEOS format) header files (lea_01.001) are extracted and used during the focussing of the raw data. To be able to use the statevectors several adaptations to the source code of ROI_PAC and StaMPS are made.

The script *extract_statevectors* gets the statevectors from the SLC header file and stores them in *hdr_data_points_$FILE_DATE.rsc*. Here *$FILE_DATE* represents the date of the SLC file. The .rsc file has to be placed in the folder where the raw data is located. By running the StaMPS script *step_slc_ers_envi* in the master folder, the raw data will be focussed. The code uses a specific combination of year, month and satellite type to either read or skip the .rsc file. In this way the script can still be used to read normal ERS-Envisat data with external orbits. Other adaptions have been made to the scripts *make_raw_ers.pl* and *roipac2doris*.

The particular way of focussing the raw ERS-Envisat data results in a (non-linear) phase ramp. This is visible in the final interferogram, after subtraction of the flat-Earth and DEM reference phases (see Figure 2.5). Since non-linear phase ramps are only apparent in the LOS interferograms that are not unwrapped in this thesis, no correction of the orbit vectors is applied. For the remaining pair the phase ramp is assumed to be linear and removed accordingly using *cpxdetrend.m* available in the DORIS Matlab toolbox.

* * *

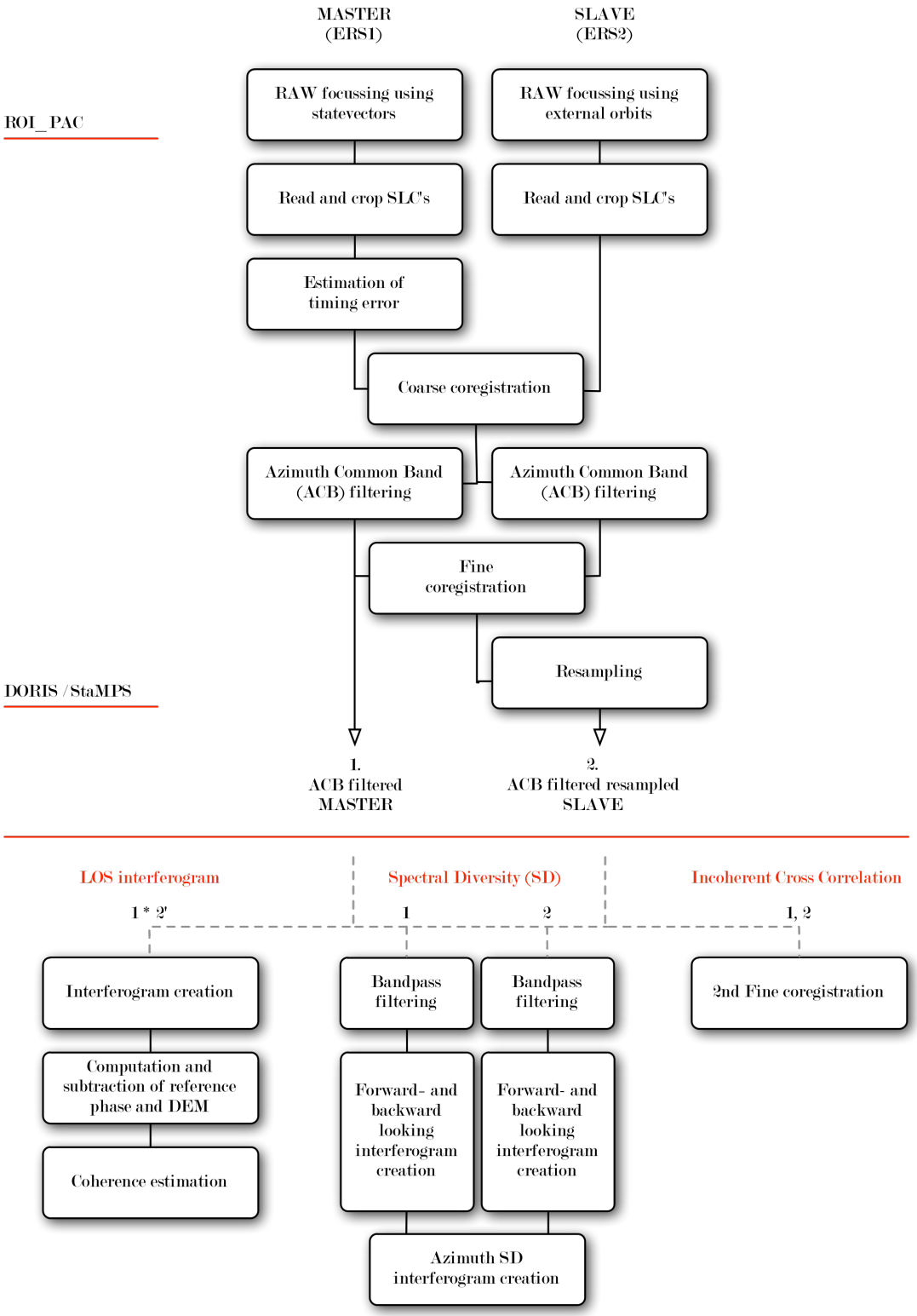

FIGURE 2.6: An overview of the general processing chain is displayed in the top half of the diagram using both ROI_PAC and DORIS. After resampling of the slave onto the master the two outputs (the azimuth common band (ACB) filtered master and an ACB filtered, resampled slave) can be used for three different operations. These are displayed in the bottom part of the flowchart: a) creation of a normal LOS interferogram, b) a SD interferogram or c) a offset tracking result.

Part II

THEORETICAL AND APPLICATIONAL FRAMEWORK

Chapter 3

Theoretical assessment of available along-track deformation extraction methods and their accuracies

The methods that will be discussed in this chapter are often used as a means of correcting an erroneous shift when coregistering two SAR images. However, the 'error' that can be found by applying these techniques can hold information about the along-track deformation or about the state of the upper atmosphere when the signal travels forth and back to the satellite. Several algorithms are available to determine shift estimates between two SAR acquisitions. All methods with their accuracies, corresponding derivations and their relations or interdependencies will be reviewed here. An overview of the algorithms that make use of the spectral properties of the data will be given in Section 3.1. The cross correlation procedures that are better known as offset tracking, will be presented in Section 3.2. The presumed similarity [Rocca, 2012] between SD, or MAI, and Coherent Cross Correlation (CCC) will be treated in Section 3.3.

Knowledge of a few definitions will give a better understanding of the subjects treated in this chapter.

In the derivation of accuracy formulas, parameter N_L is used to denote the number of independent looks in an estimation window. When a Doppler spectrum is divided into a number of bins, these subsets are referred to as *looks*. The averaging, or summation, of independent looks is useful to reduce speckle. In interferometry applications, the SAR data is often processed as single-look [Hanssen, 2001] (hence the abbreviation Single Look Complex (SLC)). When summation of independent looks occurs during interferometric processing, this is known as *multilooking*. The same term is used for simple averaging neighboring resolution cells to reduce noise. The interdependence of the pixels after averaging of the looks has to be compensated in the estimation of the accuracy. When used in the theoretical derivation of accuracy formulas, N_L corresponds to the number of looks used in the estimation window (for example, a 32x32 moving average or a similar sized cross correlation window gives 1024 independent samples if applied to SLC data).

The total correlation, or γ, used in the derivation of accuracy formulas is found to be [Zebker and Villasenor, 1992]:

$$\gamma = |\gamma_{spatial,temporal,thermal}| = |\gamma_{spatial,temporal}| \frac{1}{1 + \frac{1}{SNR}} \tag{3.1}$$

where SNR equals the Signal to Noise Ratio (SNR) and is dependent on the SAR system properties like the gain factor and antenna characteristics [Hanssen, 2001]. $\gamma_{spatial}$ is related to the geometric baseline separating the two acquisitions. Temporal decorrelation $\gamma_{temporal}$, is related to physical changes in the scattering properties of the surface. These changes comprise e.g. precipitation (snowfall), canopy growth and deformation. The real value of the complex coherence derived during interferometric processing, is used in practice as the total correlation γ.

For clarity, the master and slave SAR images are defined as c_1 and c_2.

3.1 Available split-bandwidth methods

The 'recent' introduction of MAI by Bechor and Zebker [2006] and the improvements suggested by several researchers, drew renewed attention to the subject of deriving azimuth deformation by means of split-bandwidth methods. It will be shown in Subsection 3.1.3 that MAI is not really a new technique, but an application of SD to measure azimuthal movement. Being older and the original method, SD is treated first in Subsection 3.1.1, followed by MAI in Subsection 3.1.2.

3.1.1 Spectral Diversity

Spectral diversity is introduced by Scheiber and Moreira [2000] as a technique to determine relative misregistration when coregistering two SAR images and can be performed in both range and azimuth direction. The original algorithm was published by Madsen et al. [1993] for absolute phase determination, but Scheiber and Moreira [2000] thus used it to improve the coregistration accuracy. In this subsection only the azimuth component will be discussed because the method works analogous in range and especially azimuth is of importance in this thesis. For more information on the split bandwidth in range, consult Moreira and Scheiber [1998], Scheiber and Moreira [1999] and/or Scheiber and Moreira [2000].

Background
The spectral diversity technique is applied to an interferometric pair by calculating the phase differences between the interferograms generated from two

band pass filtered images. This corresponds to precisely measuring the misregistration between image amplitudes [Erten et al., 2010]. The method works in essence by exploiting a linear phase component of the Impulse Response Function (IRF). The amplitude of an azimuth IRF is modulated by the position of the backscatter in the azimuth antenna pattern as the satellite flies over the target. To obtain the real echo, this modulation is removed by matched filtering, a procedure also known as *azimuth beam inversion*. Without going into detail, a reference signal, build from the Doppler history of consecutive pulses for each point on the ground, is compared with the received IRF and removed subsequently. This leads to a demodulated IRF. In azimuth such a response function is defined as:

$$c_1(t) = e^{j\phi_1} e^{j2\pi f_{Dc_1}(t-t_0)} sinc\left(\pi B_{a_1}(t-t_0)\right) \tag{3.2}$$

where $c_1(t)$ denotes a complex IRF of the master acquisition, dependent on the integration time variable t. t_0 equals the zero Doppler frequency position, f_{D0}, in time. The first part of this formula defines the obtained signal phase ϕ_1. The *sinc* function is the $sinx/x$ and is related to the *amplitude* of the IRF. The remaining part, the second term in Equation 3.2 denoted by $e^{j2\pi f_{Dc_1}(t-t_0)}$, is related to the *linear phase variation* of the IRF. This component is introduced by a Doppler centroid frequency being unequal to zero. Consequently, the linear phase component is only visible if $f_{Dc_1} \neq f_{D0}$.

By considering a second SAR acquisition, a similar expression for an IRF can be obtained:

$$c_2(t) = e^{j\phi_2} e^{j2\pi f_{Dc_2}(t-t_0-\Delta t)} sinc\left(\pi B_{a_2}(t-t_0-\Delta t)\right) \tag{3.3}$$

where $c_2(t)$ denotes a complex IRF of the slave acquisition.

Three differences between Equation 3.2 and Equation 3.3 are present. First, the slave IRF has a different Doppler bandwidth, B_{a_2}, and a different Doppler centroid frequency, f_{Dc_2}. However, after applying a Common Band Filter (CBF), see Figure 3.1, these parameters are equal:

$$B_a = B_{a_1} = B_{a_2} \tag{3.4a}$$

$$f_{Dc} = f_{Dc_1} = f_{Dc_2} \tag{3.4b}$$

The second difference is the addition of a relative time shift, Δt, in the second and third term of the IRF, equal to a misregistration of the slave onto the master. Third, the signal phases ϕ_1 and ϕ_2 between the acquisitions differ. If Δt would be equal to zero, the second and third term would drop out when an interferogram is formed, leaving only the relative phase differences.

In case of misregistration, an additional phase ϕ_{misreg} dependent on the timing shift, will appear:

$$\phi_{misreg} = 2\pi f_{Dc} \Delta_t \tag{3.5}$$

Since Δt is present in both the amplitude and linear phase component of the IRF, the estimation of Δt can be used to derive the misregistration in pixel offset. This will be dealt with later in this section.

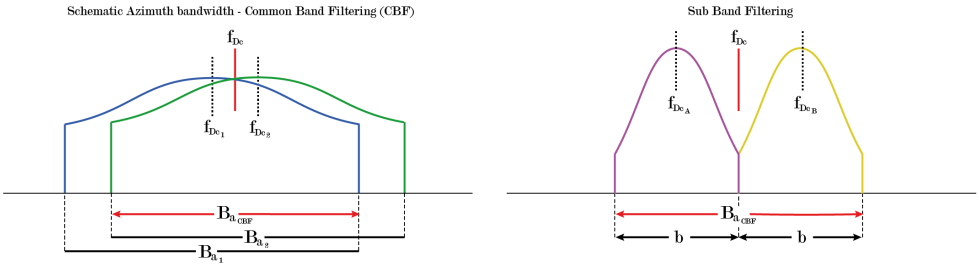

FIGURE 3.1: **Left**: Schematic representation of azimuth CBF to obtain a Doppler bandwidth $B_{a_{CBF}}$ covered by both master and slave. **Right**: Schematic representation of Gaussian weighted sub band filters to obtain a split bandwidth SD interferogram.

To always make use of the principle of a linearly varying Doppler centroid to determine the timing shift Δt, the available bandwidth is split in two equal parts to obtain four subimages: f_1^A, f_1^B, f_2^A, and f_2^B. Here A denotes subband one and B denotes subband two, as can be seen on the right in Figure 3.1. The creation of sublooks expressed as IRF's yields:

$$c_1^A(t) = e^{j\phi_1} e^{j2\pi f_{Dc}^A (t-t_0)} sinc\left(\pi B_a (t-t_0)\right) \tag{3.6a}$$

$$c_1^B(t) = e^{j\phi_1} e^{j2\pi f_{Dc}^B (t-t_0)} sinc\left(\pi B_a (t-t_0)\right) \tag{3.6b}$$

$$c_2^A(t) = e^{j\phi_2} e^{j2\pi f_{Dc}^A (t-t_0-\Delta t)} sinc\left(\pi B_a (t-t_0-\Delta t)\right) \tag{3.6c}$$

$$c_2^B(t) = e^{j\phi_2} e^{j2\pi f_{Dc}^B (t-t_0-\Delta t)} sinc\left(\pi B_a (t-t_0-\Delta t)\right) \tag{3.6d}$$

By complex multiplication of the corresponding subands in the master and its conjugate slave, the following upper and lower interferograms are found:

$$v_l = c_1^A c_2^{A*} = |c_1^A||c_2^A| e^{j\phi_1^A - \phi_2^A} \tag{3.7a}$$

$$v_u = c_1^B c_2^{B*} = |c_1^B||c_2^B| e^{j\phi_1^B - \phi_2^B} \tag{3.7b}$$

where $\phi_l = \phi_1^A - \phi_2^A$ and $\phi_u = \phi_1^B - \phi_2^B$. When the phases of these two interferograms are subtracted, according to:

$$\phi_{SD} = \phi_l - \phi_u \tag{3.8}$$

differential SD phases are obtained. In short, the two subband interferograms are subtracted from each to obtain a final differential interferogram. The differential phase is then converted to timing error by using Equation 3.5:

$$\Delta t = \frac{\phi_{SD}}{2\pi(f_c^A - f_c^B)} \tag{3.9}$$

It is important to note that Equation 3.9 is dependent on the relative difference in Doppler centroid of the two subbands, rather that the absolute values. Next,

to convert from timing errors to spatial misalignment in pixel offsets, the misregistration error has to be multiplied by the azimuth common band filtered bandwidth:

$$\Delta\hat{x} = \Delta t \cdot B_a \tag{3.10}$$

And for conversion to offsets in meters, the pixel offsets have to be multiplied by the pixelspacing:

$$\Delta x_{azimuth} = \Delta\hat{x} \cdot pixelspacing \tag{3.11}$$

This pixelspacing is in case of ERS data approximately 4.49 m.

Misalignment during coregistration can also be a measure for deformation in azimuth. The fringe density is lower in a SD interferogram compared to a conventional interferogram. The size of one fringe is dependent on the azimuth bandwidth and the Doppler centroid difference between the sub bands. Taking the example of 6/7 January 1999, the CBF Doppler bandwidth equals 1211.91 Hz. Given a Doppler centroid difference Δf_{Dc} of 410.69 Hz, a phase difference of 2π corresponding to one fringe, results in $\pm$ 13.25 m d^{-1} according to Equation 3.9, 3.10 and 3.11.

To clarify the convenient use of the split bandwidth method, the subband filters do not necessarily have to split the Doppler bandwidth in two. In some particular cases, e.g. for Delta-K systems, a bandwidth gap can be introduced. For example, in case of a fifty-fifty split, the subband width b equals $B_a/2$ and analogous for a bandwidth gap of third of the full azimuth bandwidth: $b = B_a/3$. This band split is covered by the estimation of the relative Doppler centroid difference $(f_c^A - f_c^B)$ between subband A and B in Equation 3.9, but can alternatively be denoted as:

$$\Delta\hat{x} = \frac{\phi_{SD}}{2\pi}\frac{B_a}{B_a - b} \tag{3.12}$$

Derivation of accuracy formula

Bamler and Eineder [2004] derived the estimation error of the spectral diversity method, for different subband widths b. For a single LOS interferogram like v_l and v_u, the phase noise can be estimated by [Hagberg et al., 1995]:

$$\sigma_\phi = \sigma_{\phi_u} = \sigma_{\phi_l} = \frac{1}{\sqrt{2N_b}}\frac{\sqrt{(1-\gamma^2)}}{\gamma} \tag{3.13}$$

under the assumption that N_b is large enough > 10. In Equation 3.13, N_b is:

$$N_b = N_L\frac{b}{B_a} \tag{3.14}$$

The number of independent looks in the estimation window to obtain the phase noise expression are reduced by the amount the full Doppler bandwidth is diminished, hence the scaling factor b/B_a.

To obtain an expression for the phase noise in a along-track SD interferogram,

the standard deviation of a sum of two random variables is given by:

$$\sigma_{\phi_{SD}} = \sqrt{var(\phi_l) + var(\phi_u) - 2cov(\phi_l, \phi_u)} = \sqrt{\sigma_{\phi_l}^2 + \sigma_{\phi_u}^2 - 2\sigma_{\phi_{l,u}}^2} \tag{3.15}$$

Since it is assumed that the subbands do not overlap, the covariance $cov(\phi_l, \phi_u)$ of the two variables is 0, leaving Equation 3.15 to be simplified to $\sigma_{\phi_{SD}} = \sqrt{2}|\sigma_\phi|$.

By expressing Equation 3.16a in terms of accuracy, the following equation is obtained:

$$\sigma_{\Delta\hat{x}} = \frac{\sigma_{\phi_{SD}}}{2\pi} \frac{B_a}{B_a - b} \tag{3.16a}$$

$$\sigma_{\Delta\hat{x}} = \frac{\sqrt{2}\sigma_\phi}{2\pi} \frac{B_a}{B_a - b} \tag{3.16b}$$

Substituting Equation 3.13 and Equation 3.14 gives:

$$\sigma_{\Delta\hat{x}} = \frac{1}{\sqrt{N_L \frac{b}{B_a}}} \frac{\sqrt{(1-\gamma^2)}}{\gamma} \frac{1}{2\pi} \frac{B_a}{B_a - b} \tag{3.16c}$$

where $\sqrt{2}$ drops out. Consequently, Equation 3.16c can be rewritten as:

$$\sigma_{SD} = \sigma_{\Delta\hat{x}} = \frac{1}{2} \frac{B_a}{B_a - b} \sqrt{\frac{B_a}{b}} \frac{1}{\sqrt{N_L}} \frac{\sqrt{1-\gamma^2}}{\pi\gamma} \tag{3.17}$$

The final expression is such that for any subband, for example in case of Delta-K systems, the corresponding accuracy can be derived.

3.1.2 Multiple Aperture InSAR

Multiple Aperture InSAR is introduced by Bechor and Zebker [2006] as a new method to extract along-track displacements from InSAR data. Like SD, MAI is based on split beam processing of the Doppler bandwidth, although technically the method is introduced from the perspective of the satellite geometry instead of the splitting of the full azimuth bandwidth. The suggested implementation involves filtering of the available raw SAR images with band pass filters to obtain two forward and two backward looking SLC's. The concept of band pass filtering is discussed in Subsection 3.1.1 and visualized in Figure 3.2. After the creation of the four separate SLC's, a forward- and a backward looking interferogram are produced.

Background
The middle of the antenna beam has a squint angle α_s with respect to the zero-Doppler frequency f_{D0}, as discussed in Subsection 2.1.2. This angle is 'squinted' further by adding or subtracting a part of the full antenna angular beamwidth β_a. The squinting is expressed in the parameter n, or *normalized squint*, where $n = 1$ represents the full beamwidth. In the case of MAI the extra squint angle

is equal to half the azimuth beamwidth, leading to a normalized squint factor of $n = 0.5$. The initial squint angle α_s is due the satellite geometry, whereas the extra squinting is done by signal processing after acquisition. The MAI interferometric phase is then constructed by subtracting the two separate forward- ϕ_f and backward ϕ_b looking phases from each other:

$$\phi_{MAI} = \phi_f - \phi_b = -\frac{4\pi}{l} n d_{az} \tag{3.18}$$

where d_{az} is the along-track surface deformation and l the effective antenna length. Recalling the parameters $\lambda = 5.6\,\text{cm}$ and $l = 10\,\text{m}$ from Chapter 2, one fringe leads to 10 m in along-track offset. The symmetry between forward and backward looking geometries results in a range component and troposphere in the forward and backward looking interferograms that are almost identical. Consequently, the topographic and tropospheric contributions to the phase cancel out when creating the final interferogram [Gourmelen et al., 2011].

Jung et al. [2009] takes the idea further by examining the effects of flat-Earth and topographic phases on the derivation of the MAI phase. The effects of flat-Earth and topographic phases are caused by a difference in perpendicular baselines between the forward and backward looking interferograms because of non-parallel orbit trajectories during the acquisition of the master and slave. Thus, small deviations in the satellites orbit may result in significant flat-Earth phases. Additionally, the extra squinting of the master and slave separately can lead to topographic phase errors, related to the different geometrical squint angle between the two individual images. However, the topographic phase is often much smaller than the additional flat-Earth phase, so in terms of processing one might consider to ignore the topographic phase. Next to this, detailed processing steps are presented by Jung et al. with particular attention given to coherence improvement and computational efficiency. However, the suggested processing scheme recommends filtering steps and corrections to the perpendicular baselines of the backward looking pair with respect to the forward looking pair, that are not applicable since the particular implementation used in this thesis works from a full bandwidth master and resampled slave, see Subsection 4.1.1.

Derivation of accuracy formula

The derivation of the accuracy formula according to Bechor and Zebker [2006] is based on inverting Equation 3.18 and expressing it in terms of uncertainties. For a band split of $n = 0.5$, this results in the following:

$$\sigma_{d_{az}} = \frac{l}{2\pi} \sigma_{\phi_{MAI}} \tag{3.19}$$

where σ_ϕ is the standard deviation of the MAI phase and $\sigma_{d_{az}}$ the standard deviation of the azimuth displacements.

The Cramer-Rao bound for the phase standard deviation σ_ϕ of a normal LOS interferogram was shown by Rodriguez (- to be published) to be:

$$\sigma_\phi = \langle (\hat{\phi} - \langle \hat{\phi} \rangle)^2 \rangle^{1/2} = \frac{1}{\sqrt{2N_L}} \frac{\sqrt{(1-\gamma^2)}}{\gamma} \tag{3.20}$$

In this equation, according to Rodriguez and Martin [1992], N_L is the number of looks to be averaged and total correlation γ. When the along-track integration time is reduced because of the bandwidth split, the SNR that determines γ will be smaller.

Using Equation 3.20 for both the forward- and backward looking interferogram, the standard deviation for a differential interferogram is [Jung et al., 2009]:

$$\sigma_{\phi_{MAI}} = \sqrt{var(\phi_f) + var(\phi_b) - 2cov(\phi_f, \phi_b)} = \sqrt{\sigma^2_{\phi_f} + \sigma^2_{\phi_b} - 2\sigma^2_{\phi_{f,b}}} \tag{3.21}$$

Because the subbands do not overlap they are statistically independent, leading to: $cov(\phi_f, \phi_b) = 0$. By further expanding this equation, the obtained MAI phase standard deviation is found:

$$\sigma_{\phi_{MAI}} = \frac{1}{\sqrt{N_L}} \frac{\sqrt{(1-\gamma^2)}}{\gamma} \tag{3.22}$$

When applying MAI, the number of looks N_L taken to determine the standard deviation has to be reduced by a factor of $1 - n$, because the resolution is reduced by splitting the synthetic aperture in two.

3.1.3 Equality of Multiple Aperture InSAR and Spectral Diversity

In essence MAI is a particular instance of the SD method in azimuth, processed with a perfect band split of $b = B_a/2$. By conducting a theoretical comparison of the two methods, one can deduce that both rely on the same spectral properties of the signal. First, the formulas to estimate shifts in azimuth are discussed for both methods, after which the comparison of the accuracy formulas will be addressed.

Equality in terms of shift estimates
The shift estimate of SD as introduced by Bamler and Eineder [2005] is denoted as:

$$\Delta\hat{x}_{SD} = \frac{\phi_{SD}}{2\pi} \frac{B_a}{B_a - b} \tag{3.16a}$$

in units of along-track resolution elements. As noted before, B_a equals the full bandwidth and b equals the subband bandwidth. For $b = B_a/2$, Equation 3.16a simplifies to:

$$\Delta\hat{x}_{SD} = \frac{\phi_{SD}}{\pi} \tag{3.23}$$

again in units of azimuth resolution elements.

The shift estimate for MAI, expressed in d_{az} [m] according to Bechor and Zebker [2006], Jung et al. [2009] and Hu et al. [2012b] is:

$$d_{az} = \frac{l}{4\pi}\frac{1}{n}\phi_{MAI} \tag{3.18}$$

where n equals the split factor. Splitting the bandwidth in two parts gives $n = 0.5$. Equation 3.18 then simplifies to:

$$d_{az} = \frac{\phi_{MAI}}{\pi}\frac{l}{2} \tag{3.24}$$

And since the along track resolution for SAR is theoretically equal to $\delta_{az} = l/2$, Equation 3.23 and Equation 3.24 are the same.

Equality in terms of accuracy formulas

A similar comparison can be made with both expressions of accuracy for SD and MAI. When Equation 3.22 is substituted in Equation 3.24, the following formulation is derived:

$$\sigma_{d_{az}} = \frac{1}{\sqrt{N_L(1-n)}}\frac{\sqrt{(1-\gamma^2)}}{\pi\gamma} \tag{3.25}$$

where N_L is reduced by a factor $(1-n)$ to compensate for the resolution degradation because of the reduced azimuth bandwidth. Now recalling the expression Equation 3.17 for the accuracy of SD, and completing with a band split of $b = B_a/2$:

$$\sigma_{\Delta\hat{x}} = \sqrt{2}\frac{1}{\sqrt{N_L}}\frac{\sqrt{1-\gamma^2}}{\pi\gamma} \tag{3.26}$$

where $\sqrt{2}$ is due to $\sqrt{B_a/b}$ when $b = B_a/2$. Based on Equation 3.25 and Equation 3.26, it can be concluded that both methods are the same.

On the band split operation

To visualize the splitting of the bandwidth into forward and backward looking images, Figure 3.2 is of use. The complete (in terms of a full Doppler bandwidth) master and slave are denoted as AC and BD respectively. By applying band pass operations, both the master and slave are split in two parts and four separate SAR images are obtained. To create a lower band/forward looking interferogram, images A and B are multiplied in the complex domain. Analogous, this holds for a upper band/backward looking interferogram as well. Finally, a differential interferogram is obtained by another complex multiplication of the lower band/forward looking interferogram and the complex conjugate of the upper band/backward looking interferogram. Expressed in terms of phases:

$$\phi_{SD} = \phi_{MAI} = \phi_A - \phi_B - (\phi_C - \phi_D) \tag{3.27}$$

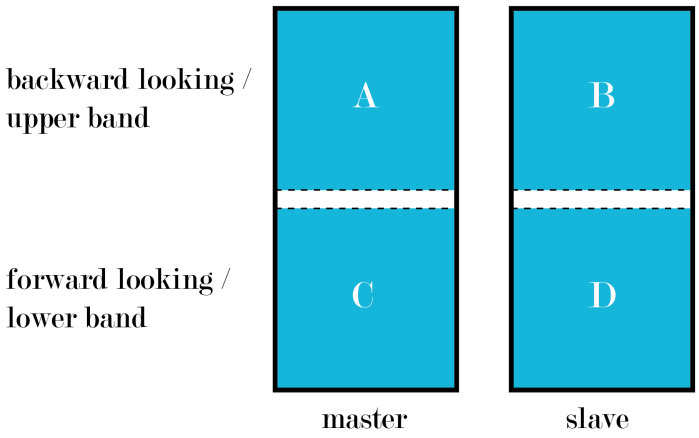

FIGURE 3.2: Schematic visualization of obtaining a differential SD or MAI interferogram. The master and slave are denoted as AC and BD respectively. By means of splitting the master and slave azimuth bandwidth into two, four SAR images are generated. Complex multiplication creates an upper/backward (AB^*)- and lower/forward looking (CD^*) interferogram. Lastly, the differential phases are calculated by $\phi_{SD} = \phi_{MAI} = \phi_{AB^*} - \phi_{CD^*}$.

3.2 Available offset tracking methods

Coherent Cross Correlation (CCC), also known as coherent speckle tracking, and Incoherent Cross Correlation (speckle tracking) (ICC), or (incoherent) speckle tracking, are both instances of the generic offset tracking. Offset tracking also includes coherence- and feature tracking. The former is not considered here since coherence tracking is not widely used, and no analytical expressions are available for this method. The latter, the tracking of point scatterers, is also not considered here. The difference between coherent and incoherent speckle tracking is due to the cross correlation operation which is respectively complex (phase and amplitude are preserved), CCC or only based on the magnitude of the signal, ICC.

The result of the cross correlation procedure are two pixel offset vectors, one in azimuth and one in range direction. To convert the pixel offsets to meters, they have to be multiplied with the pixelspacing according to:

$$\Delta x_{azimuth} = \Delta x_{misreg} \cdot pixelspacing \tag{3.28}$$

Image patch cross correlation is often used as an alternative to InSAR processing when there is severe loss of coherence or as an addition to LOS InSAR processing to obtain the displacement estimates in azimuth direction. Speckle tracking is specifically focused on the correlation of the speckle pattern of the two images, whereas feature tracking uses all traceable scatterers (like rocks, crevasses or volcanic ash lines) to track the movement of, in this particular case, ice [Joughin et al., 2010]. With this distinction it will be clear that speckle tracking works even

in the most featureless regions as long as the speckle pattern remains coherent [Gray and Mattar, 1998]. Feature tracking on the other hand is useful when the speckle pattern is completely decorrelated but distinct features are clearly visible. Results from these offset tracking procedures are very dependent on the size of the correlation windows, thus the amount of spatial averaging during processing.

In Subsection 3.2.1 the specifics about CCC and corresponding accuracy formula will be treated, whereas ICC will be discussed in Subsection 3.2.2.

3.2.1 Coherent Cross Correlation

The optimum Maximum Likelihood Estimator (MLE) for mutual shift of partially correlated stationary circular Gaussian signals is the cross correlation operation [Bamler, 2000]. This means that no shift estimates can be obtained more accurately with the available data. The derivation of the accuracy formula is given for homogeneous image patches, i.e. no images features are extant in the data. The presence of image features can improve the methods accuracy because the return of the bright image feature is being tracked instead of the speckle pattern.

Measurement uncertainty, expressed in the standard deviation of displacement for CCC, see Equation 3.29 is given by Bamler and Eineder [2004, 2005]. The equation is a function of the real coherence γ and N_L:

$$\sigma_{ccc} = \sqrt{\frac{3}{2N_L}} \frac{\sqrt{1-\gamma^2}}{\pi\gamma} \tag{3.29}$$

The derivation of this equation has been given by Bamler [2000]. The comparison between CCC and SD will be assessed in Section 3.3.

3.2.2 Incoherent Cross Correlation

Incoherent speckle tracking, or ICC, is based on pixel level cross correlation of the amplitude signal of two SAR images [Gray and Mattar, 1998, Joughin et al., 1998]. The procedure is identical to CCC, except for the use of the amplitude instead of the full complex signal.

Until recently, no expression for ICC was available because of difficulty deriving an analytical expression taking into account the statistical interdependence between neighboring pixels when cross correlating intensity images [Bamler and Eineder, 2005]. De Zan [2013] gave a full derivation of this equation by finding an expression dependent on the curvature of the cross correlation peak to find the shift for which the correlation is maximum. The uncertainty for ICC is given

by:

$$\sigma_{icc} = \sqrt{\frac{3}{10N_L}} \frac{\sqrt{2+5\gamma^2-7\gamma^4}}{\pi\gamma} \tag{3.30}$$

3.3 Similariy assessment of Spectral Diversity and Coherent Cross Correlation

Two methods can be compared by assessing the quality formulations, or accuracy equations. If two methods give the same results in terms of accuracy, then the methods can be thought of as statistically equal. A theoretical comparison of the accuracy formulas of SD and CCC is given by Bamler and Eineder [2004] and Bamler and Eineder [2005] as the ratio between their measurement uncertainty equations σ_{SD}/σ_{CCC}.

Recalling Equation 3.17 and Equation 3.29, the following expression is noted down:

$$\frac{\sigma_{SD}}{\sigma_{CCC}} = \frac{\frac{1}{2}\frac{B_a}{B_a-b}\sqrt{\frac{B_a}{b}}\frac{1}{\sqrt{N_L}}\frac{\sqrt{1-\gamma^2}}{\pi\gamma}}{\sqrt{\frac{3}{2N_L}}\frac{\sqrt{1-\gamma^2}}{\pi\gamma}} \tag{3.31a}$$

$$\frac{\sigma_{SD}}{\sigma_{CCC}} = \frac{\frac{1}{2}\frac{B_a}{B_a-b}\sqrt{\frac{B_a}{b}}\frac{1}{\sqrt{N_L}}}{\sqrt{\frac{3}{2}}\frac{1}{\sqrt{N_L}}} \tag{3.31b}$$

Further simplification leads to:

$$\frac{\sigma_{SD}}{\sigma_{CCC}} = \frac{1}{\sqrt{6}}\frac{B_a}{B_a-b}\sqrt{\frac{B_a}{b}} \tag{3.31c}$$

When Equation 3.31c is plotted for different subband widths B_a/b with corresponding gaps, the line in Figure 3.3 is obtained. The minimum of this curve lies on $B_a/b = 1/3$ meaning the full Doppler bandwidth is divided into three parts of equal size, creating a bandwidth gap of $1/3$ of the entire azimuth bandwidth. By substituting this into Equation 3.31c, the following ratio for this specific band split can be obtained:

$$\sigma_{SD} = 1.061\sigma_{CCC} \tag{3.32a}$$

And for a 50% band split, equal to $B_a/b = 1/2$:

$$\sigma_{SD} = 1.155\sigma_{CCC} \tag{3.32b}$$

The curve in Figure 3.3 shows the course of Equation 3.31c and can be interpreted as a measure for the similarity of the two methods. The ratio never equals 1, but in the case of an ideal bandwidth split of $1/3$, SD only differs from the MLE by approximately 6%, leading to the conclusion that **SD and CCC are**

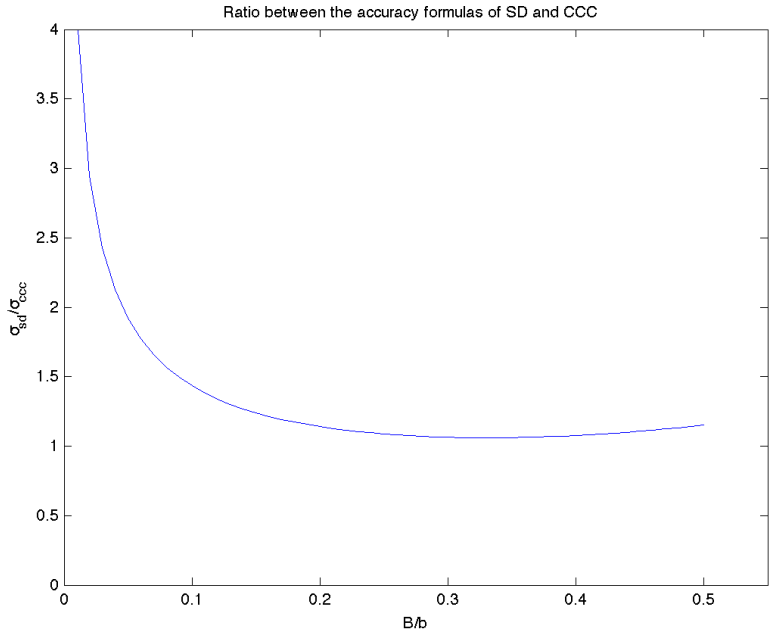

FIGURE 3.3: The ratio between SD and ICC for different band split configurations B_a/b is given. According to this graph, a band split of $1/3$ is optimal, meaning the performance of SD is close to the MLE.

comparable in theoretical accuracy, but **SD and CCC give approximately equal results when implemented properly**. The latter statement is assumed to be true because the 6% difference in accuracy is neglectable when these methods are applied to real data. As discussed before, the theoretical accuracy of CCC assumes homogeneous (circular white Gaussian) data. Real data never meets this criterium, mainly due to the presence of bright scatterers like nunataks (rocks piercing through the ice), rock ridges or stable crevasses. The apparent features are thus tracked instead of the speckle pattern for the pixel under investigation.

On the equality of ICC with respect to CCC

According to the comparison between SD and ICC, the performance enhancement of Equation 3.29 over Equation 3.30 is given by the ratio between them. Bamler and Eineder [2005] gave the suggestion that ICC would perform at least $\sqrt{2}$ worse because ICC uses half of the available information by only exploiting the amplitude of the signal. Simulations showed that this is only true for very high coherence values. De Zan [2013] denoted a full derivation of the speckle tracking measurement uncertainty, enabling a theoretical comparison. **When γ approaches 1 in the limit, CCC outperforms ICC by a factor of 1.8 for the variance comparison ratio $\sigma^2_{ICC}/\sigma^2_{CCC}$.**

* * *

Chapter 4

Improvements on the extraction of along-track deformation

In the previous chapter, 3, all different methods to extract along-track deformation from SAR data are introduced. Their theoretically achievable accuracy is derived and a similarity assessment between SD, CCC and ICC is discussed. In this chapter, two of the aforementioned methods, ICC and SD, will be applied to real data to confirm the theoretical findings. This will be dealt with in Section 4.1. To use the obtained SD data for glaciology purposes, all distortions present in the scenes have to be removed. Section 4.2 will deal with a masking method to separate the signal of interest from its surroundings when applying filtering procedures as discussed in Section 4.3.

4.1 Application of different azimuthal deformation extraction techniques

From the techniques discussed in Chapter 3, two are implemented in StaMPS [Hooper et al., 2012] and DORIS [Kampes et al., 2003]. Incoherent Cross Correlation (speckle tracking) is implemented as a method to obtain sub-pixel offsets when coregistering the slave onto the master. Spectral Diversity is implemented as an optional step in StaMPS when the slave has been resampled onto the master. The methods and corresponding results of the application of these two methods on real data will be given in Subsection 4.1.1 and Subsection 4.1.2 respectively. The outcomes of the procedures will be compared to each other, both visually and by means of gross statistics, in Subsection 4.1.3.

Coherent Cross Correlation (CCC) is not implemented and therefore not compared to ICC and SD. To implement coherent cross correlation, the flat-Earth (the residual phase caused by the reference surface) and phases due to the topography of the scene have to be removed from both the master as well as the slave separately. These steps have to be carried out before the actual complex cross correlation takes place. This is different from the removal of flat-Earth and topographic phases in conventional InSAR processing, where these phases are removed after interferogram formation.

4.1.1 Spectral Diversity

Authors Scheiber and Moreira [2000] who introduced SD did not give a particular implementation for the split-bandwidth routines. However, Bechor and Zebker [2006] who reintroduced SD in azimuth as MAI, and Jung et al. [2009] who improved the processing of MAI, presented a processing overview to be able to get the final MAI interferogram. Since it is shown in Chapter 3 that they are equal, the processing chain of MAI can be followed. The steps in that chain consisted of the splitting of the azimuth bandwidth for the master and slave separately. Then conventional InSAR processing was applied to get two interferograms. These normal interferograms were subsequently subtracted from each other to arrive at a final MAI interferogram. The setup of this processing chain is such that raw data is required to start with. Since the main interferometric processor used in this project is DORIS, which assumes SLC data focussed in zero-Doppler, the aforementioned splitting of the raw bandwidth cannot be applied. For this reason another approach has been chosen to get to the azimuth SD interferogram.

SD in azimuth is implemented as a Matlab routine. From the master or slave image a patch of 1500 lines with full width is taken and Fourier transformed to obtain the frequency distribution of that patch. An example of such a Fourier transformed patch is visible in Figure 4.2 (A).

The band pass filters designed to split the bandwidth in two parts are build from a Gaussian window function. An example of the band pass filters to obtain the upper- and lower band images are displayed is Figure 4.1 (A). These are 'squared' by their corresponding part of the azimuth spectrum to remove the antenna pattern. This can be seen in Figure 4.1 (B). The remaining spectra patches after filtering are shown in Figure 4.2. The Gaussian weighting is clearly visible in (B) where the top (around y-axis = 800) and bottom side (around y-axis = 1500) of the spectrum are less strong.

For computational efficiency Φ_{SD}, the SD phase, is not obtained by applying Equation 3.8:

$$\Phi_{SD} = imag\left(c_1^A c_2^{A*}(c_1^B c_2^{B*})^*\right) \tag{3.8}$$

but by a slightly altered version as can be seen in Equation 4.1:

$$\Phi_{SD} = imag\left(c_1^A c_1^{B*}(c_2^A c_2^{B*})^*\right) \tag{4.1}$$

This enables the possibility of deriving the results of $c_1^A c_1^{B*}$ and $(c_2^A c_2^{B*})$ in the same script. When both the sub band interferograms c_1^{AB} and c_2^{AB} are made, the final azimuth SD interferogram is obtained by subtracting these two.

The left image in Figure 4.3 shows an example of the outcomes of this SD processing (6/7 January 1999 pair). The image is unfiltered and appears very noisy. By means of a 32x32 moving average filter this noise is reduced, making the misregistration visible. In the particular case shown, the streaks running from

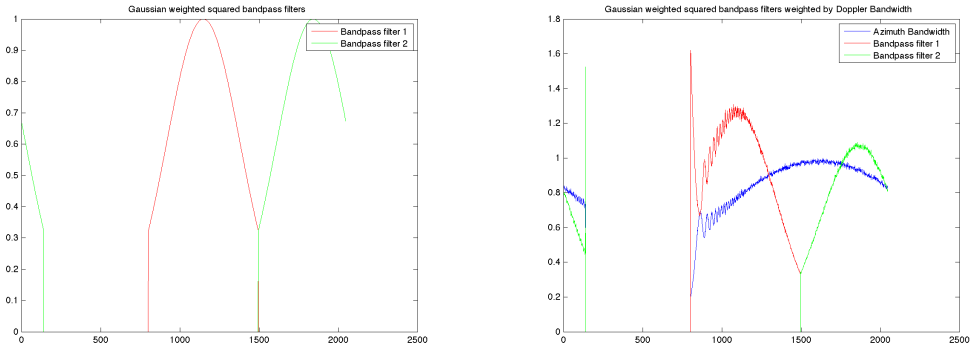

(A) (B)

FIGURE 4.1: (A) shows two Gaussian weighted band pass filters. In (B) the two filters of (A) are applied to the full Doppler bandwidth to achieve the neccessary band split of factor 2. Both filters are squared by the azimuth bandwidth to remove the antenna pattern.

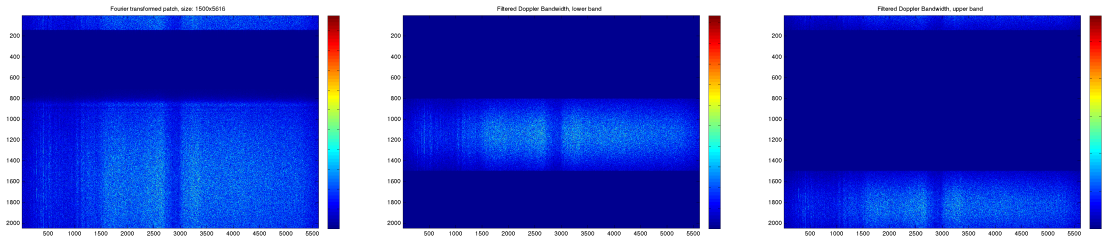

(A) (B) (C)

FIGURE 4.2: The band pass filtering, as shown in Figure 4.1, is applied to the full common band filtered Doppler bandwidth. In this figure the images shown are Fourier transformed amplitude patches. (A) corresponds to the blue curve in Figure 4.1. (B) and (C) are the two obtained band pass images.

Southwest to Northeast (in radar coordinates) can be interpreted as anomalies due to distortions in the ionosphere. The offset values range from $-0.5\,\mathrm{m\,d^{-1}}$ to $0.5\,\mathrm{m\,d^{-1}}$. The interpretation and removal of these ionospheric streaks, which are considered as low frequency noise, is dealt with in Section 4.3.

The signal of interest is the movement of the glacier. In the image displayed in Figure 4.3, this is the yellow patch located between rangepixels 3500 - 4500 and azimuthlines 5000 - 10000. The offset values are in the order of $1\,\mathrm{m\,d^{-1}}$, which is expected based on field observations during the surge.

As discussed in Chapter 3, Jung et al. [2009] implemented corrections for the perpendicular baseline difference between the upper- and lower band interferogram. These perpendicular baseline differences were the result of slightly different satellite orbits within the synthetic aperture. By splitting the azimuth bandwidth, and thus reducing the synthetic antenna length, these differences appear as phase ramps in the interferogram. However, because these phase ramps are

not visible by eye in the derived azimuth SD interferograms, the baseline corrections have not been applied.

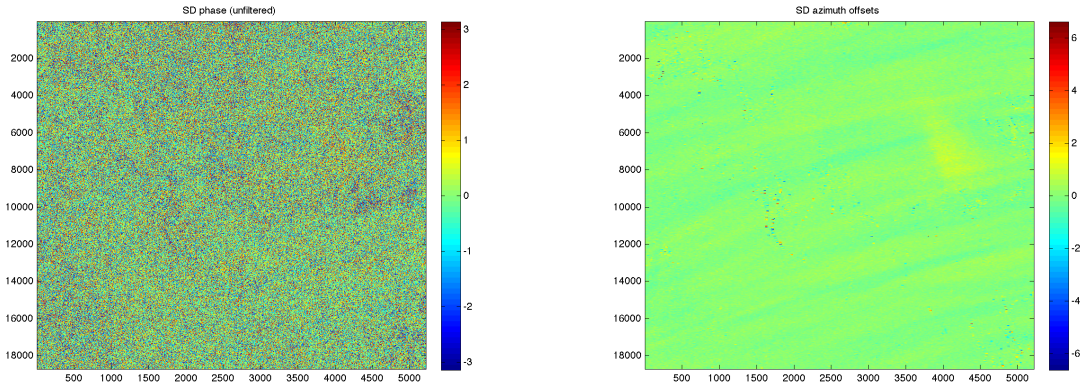

(A) (B)

FIGURE 4.3: The SD phase result $[-\pi$ to $\pi]$ of the interferometric pair from 6/7 January 1999 in radarcoordinates (range on the horizontal axis and azimuth on the vertical axis). (A) shows the original output (no multilooking), (B) shows (A) filtered with a 32x32 moving average filter, and converted to offsets.

4.1.2 Incoherent Cross Correlation

The ICC or speckle tracking results are obtained by executing another *fine* coregistration after resampling of the slave onto the master. Fine coregistration is a standard step in the processing with DORIS to obtain the offset vectors with a subpixel level accuracy. The offset is computed in the space domain on the magnitude images. Constant patch sizes of 32x32 are taken and cross correlated between the resampled, azimuth common band filtered (ACB) slave and the ACB filtered master. The coordinates of the center pixel are chosen such that there is no overlap between the neighboring shifting windows when cross correlating the two images. By multiplying the offset outcomes with the azimuth pixelspacing, which is given in the outputfile *$MASTER_DATE.slc.rsc.hst* of the focussing procedure performed with ROI_PAC, the pixel patch offsets in meters are obtained. An example of the speckle tracking outcomes can be found in Figure 4.4 (B).

The implementation of the cross correlation procedure requires an odd window size to make the center of the correlation window to be defined as a pixel. This is automatically forced by the algorithm. As a measure for the quality of the cross correlation, a correlation coefficient Γ is calculated. According to the DORIS

manual, the correlation between two images is defined by:

$$\Gamma = \frac{cov(c_1, c_2)}{\sqrt{var(c_1)var(c_2)}} = \frac{E(c_1 \cdot c_2^*) - E(c_1)E(c_2^*)}{\sqrt{\left(E(c_1 \cdot c_1^*) - E(c_1)E(c_1^*)\right) \cdot \left(E(c_2 \cdot c_2^*) - E(c_2)E(c_2^*)\right)}} \quad (4.2)$$

where $E(.)$ denotes the expected value. As Equation 4.2 shows, the mean is first subtracted. This distinguishes the computation of the correlation coefficient from the interferometric coherence. An example of a correlation file is displayed in Figure 4.4 (A).

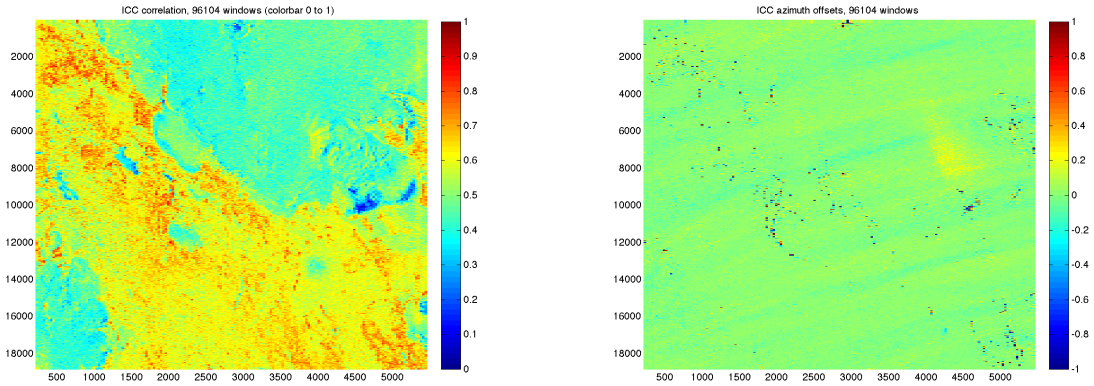

(A) (B)

FIGURE 4.4: The ICC result [m] of the interferometric pair from 6/7 January 1999. (A) shows the correlation for each window, (B) shows the output of the cross correlation operation with a 32x32 window.

4.1.3 Gross statistics and performance comparison between Spectral Diversity and Incoherent Cross Correlation

ICC is the method most frequently used to obtain azimuth offsets and can deliver estimates that can be used in combination with LOS interferograms. Since the introduction of SD and the renewed attention due to the publications about MAI, questions have arisen what the most preferable method is in terms of accuracy and applicability to obtain offsets in azimuth direction.

The application of both SD and SD on real data is introduced in respectively Subsection 4.1.1 and Subsection 4.1.2. The settings for both methods are chosen in such a way that they are comparable. An overview of these input parameters is listed below:

- *SD*: split bandwidth with a sub band size of $B_{a_{CBF}}/2$ after resampling of the slave onto the master to obtain misregistration phases

- *SD*: the result is filtered by a square 32 pixel moving average filter
- *SD*: the azimuth SD phases are converted to offsets in meters using Equation 3.9, 3.10 and 3.11.
- *ICC*: another fine coregistration procedure after resampling of the slave onto the master to obtain misregistration offsets in pixel offsets
- *ICC*: conversion to offsets using Equation 3.28 and the same pixelspacing as taken in the conversion of SD phases to meter offsets.

The outcomes of both methods are shown in Figure 4.5 (A) for SD and (B) for ICC. The third column shows the difference between SD and ICC. For this, both processing outcomes are converted to offsets in meters. In the ICC images the signal of interest is indicated by a red box.

The same pixels that are used as the center pixels for the cross correlation windows are selected from the SD image. By subtracting the ICC offsets from the SD offsets, residuals are obtained. These residuals are shown in Figure 4.5 (C).

In all the images, white areas are present due to the masking of pixels with offsets below the correlation threshold (fixed at $\Gamma < 0.3$) or above the offset threshold of $5\,\mathrm{m\,d^{-1}}$. The masking is necessary in order to obtain reliable estimates of the performance of both methods to make a sound comparison.

Conclusions
Based on the theoretical findings, the discussed processing methodology and the results presented in Figure 4.5, conclusions can be drawn. When observing the outcomes in Figure 4.5, several differences and similarities can be noticed. First, **both methods, SD and ICC give very similar results.** Although a considerable amount of pixels is masked out, the difference in noise level is still visible. In the results at the top row (corresponding to the 6/7 January 1999 data) the noise is more prevalent in the ICC results, compared to the SD image.

In the second and last row (corresponding to the 10/11 February 1999 and 26/27 January 2000 image pairs), the difference image shows residual offsets. In both cases **the ICC results have slightly higher values compared to the SD results, but fewer details are visible**. This can have two reasons. *One*: the lower precision of the ICC results, values rounded to $\pm$ 0.5, compared to 5 decimal places in case of SD. *Two*: the statistical dependence between neighboring pixels within the estimation window is different for the cross correlation procedure and the moving average filtering.

From theory it is expected that SD outperforms ICC if only for the fact that ICC lacks the use of the phase component. Reducing the amount of information reduces the method accuracy. Gross statistics of the derived products are obtained by the generation of histograms with corresponding mean and standard deviations values. The standard deviations are calculated for all available pixels (so, including deforming regions, but excluding regions that need to be unwrapped)

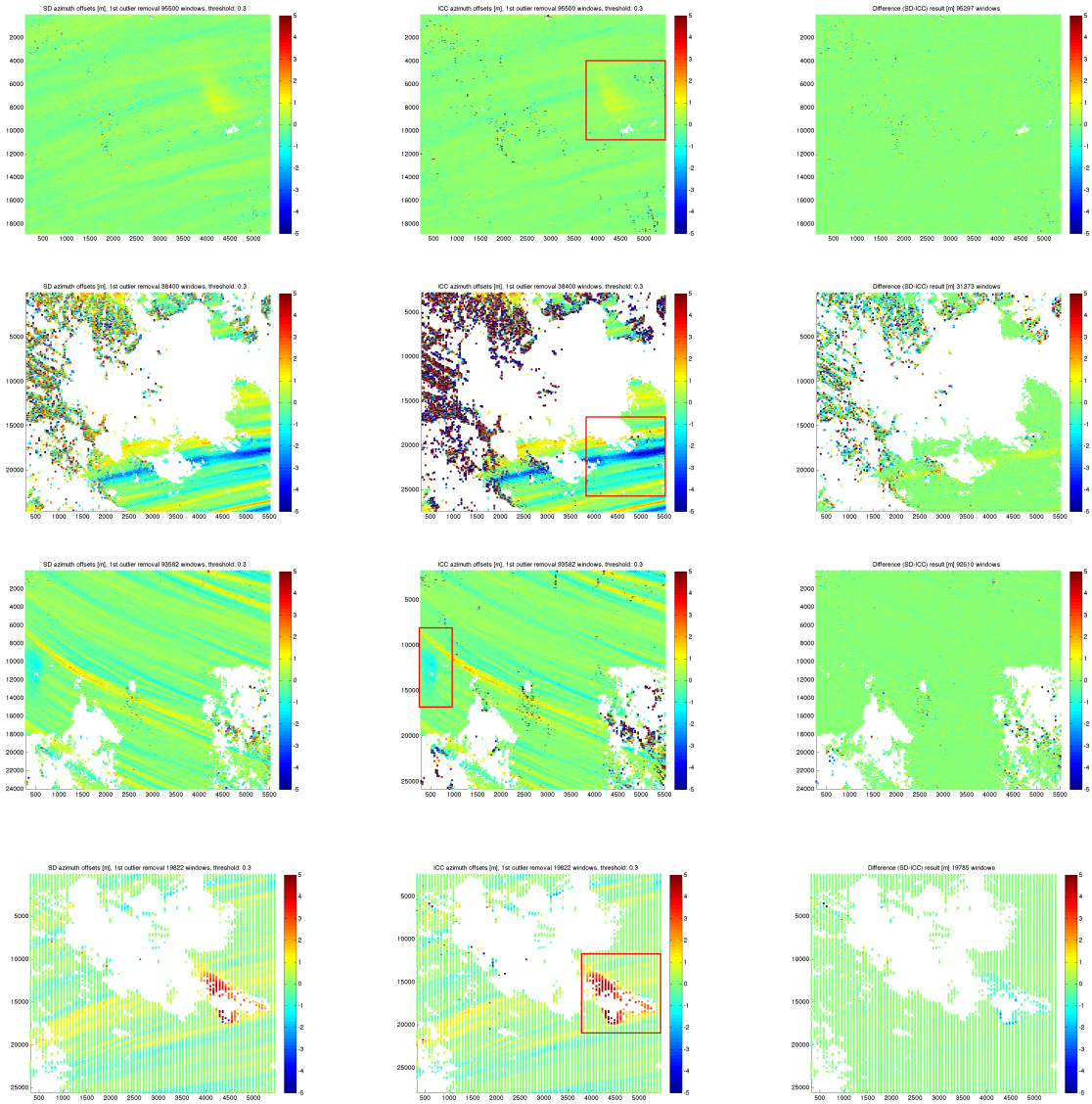

(A) SD (B) ICC (C) Residuals: (A) - (B)

FIGURE 4.5: The outputs of SD and ICC in meters for all pairs (6/7 January 1999, 10/11 February 1999, 27/28 February 1999 (descending) and 26/27 January 2000 respectively) are displayed in (A) and (B) respectively. The red boxes in the ICC results show the location of the signal of interest. (C) shows the difference of SD with ICC. The pixels that are masked out are below the correlation threshold of 0.3 or above the offset threshold of $5\,\mathrm{m\,d^{-1}}$.

in case a square 32-pixel window is used for the cross correlation and a equally sized window for the moving average filter. The values can be found in Table 4.1. **For all cases, SD outperforms ICC by a factor of 1.6 at minimum**.

In Figure 4.6 histograms are plotted for SD and ICC both before and after outlier removal. These are normalized using:

$$z = \frac{X - E(X)}{\sigma(X)} \tag{4.3}$$

Where X is the random variable of interest, in this case X is representing all the pixel values. $E(X)$ is the expected value, or mean, whereas $\sigma(X)$ equals the standard deviation valid for all available pixels. By subtracting the mean from the population and dividing it by the standard deviation, z, the standardized form of the original random variable, is derived.

In the left pair the influence of outliers on the performance of ICC is obvious. The histogram is sharply peaked in the center and has a wide bin range on the horizontal axis. By removing the clear outliers, simply by using a threshold on the motion of maximum $5\,\mathrm{m\,d^{-1}}$, the histograms are more comparable. **After outlier removal SD outperforms ICC by a factor of minimum 1.1**. By setting the threshold on the offsets, the areas where motion is large enough to be wrapped are masked out as well, thereby avoiding unequal comparison of the standard deviations.

InSAR pair	σ_{SD} $[\mathrm{m\,d^{-1}}]$	σ_{ICC} $[\mathrm{m\,d^{-1}}]$	σ_{SD} OR $[\mathrm{m\,d^{-1}}]$	σ_{ICC} OR $[\mathrm{m\,d^{-1}}]$
6/7 January 1999	0.269	0.946	0.260	0.287
10/11 February 1999	1.715	9.023	1.411	1.734
27/28 February 1999	0.506	2.272	0.463	0.516
26/27 January 2000	0.590	0.918	0.577	0.633

TABLE 4.1: This table shows the different standard deviations for all data pairs using either SD or ICC before and after outlier removal (OR) of all offsets larger than $5\,\mathrm{m\,d^{-1}}$. Note that SD outperforms ICC in all cases.

In accordance with the theoretical findings in Chapter 3, SD performs better in terms of accuracy than ICC. However, after outlier removal the accuracy of speckle tracking improves significantly. De Zan [2013] states that the performance degradation $\sigma^2_{ICC}/\sigma^2_{CCC} = 1.8$ in the limit $\gamma \to 1$. From Table 4.1 can be read that ICC performs better than the theoretical value of 1.8, even though the coherence is not equal to one. One explanation could be that the particular implementation of SD reduces the performance of the split bandwidth results. The execution differs from the original published method by taking an interferometric pair that is processed as a whole before the band split is applied, contrary to splitting the raw files and processing two separate interferometric sub pairs. A different explanation is the specific implementation of the sub band filters, e.g. the Gaussian weighting.

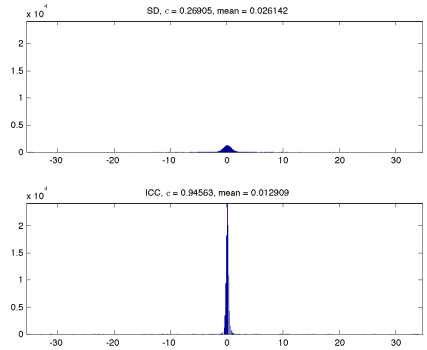

(A) Histogram of SD (top) and ICC (bottom)

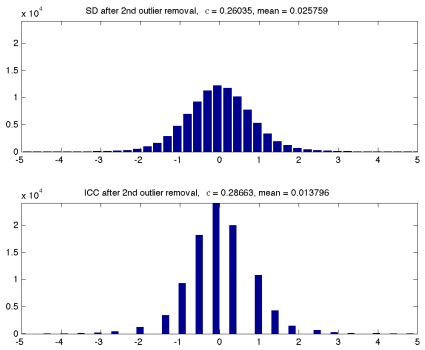

(B) Same as (A), but after outlier removal based on a maximum displacement of 5 m.

FIGURE 4.6: The histograms of SD and ICC are displayed for the entire image, both before (A) and after outlier removal (B). Note that the horizontal axis in (A) is different for SD and ICC. The standard deviation of ICC improves significantly by setting a maximum allowed displacement. However, it is not correct to state that ICC outperforms SD. The precision of the ICC results (rounded off to 0.5) is much worse than SD. The results of the latter come with a precision of 5 decimal places.

Apart from the optimal performance measured by the comparison of accuracies, **SD has an advantage over ICC by the speed of processing and pixel density**. Both methods have been processed on the same engine. The execution of the SD scripts took $\pm$ 60 s and the original pixel density ($5515 \cdot 19803$) is maintained, whereas speckle tracking took about 1.5 hours to be processed for 102090 windows. On the other hand, the splitting of the bandwidth comes with the price of a reduced resolution. To what extent the original azimuth resolution is reduced, is dependent on the implementation of the band filtering, i.e. what portion of the bandwidth is preserved and what the influence of the Gaussian weighting of the sub band filters is. Another disadvantage of SD is the necessity to unwrap if the motions in the differential interferogram are above the fringe threshold of 2π. As discussed in Chapter 3, Section 3.1, with a Doppler bandwidth of 1211.91 Hz and a Doppler centroid difference of 410.69 Hz, a phase difference of 2π results in $\pm$ 13.25 m d^{-1}.

4.2 Smart Pixel Selection

Feature tracking is a method often applied to coregister two images. Within the domain of remote sensing it can also be used to quantify deformation on a surface. In optical remote sensing specifically, techniques like the Kanade-Lucas-Tomasi (KLT) feature tracker (Tomasi and Kanade [1991] or Scale Invariant Feature Transform (SIFT) by Li et al. [2008] are well known tools. KLT only

makes use of spatial intensity information to find the best match, whereas SIFT uses distance, orientation and scale to find a good fit.

When estimating displacements on a glacier, there is a need for extracting only the pixels where there is actual movement. The edge of the glacier with respect to its surroundings has to be found. Edge detection algorithms, for example used in Liu and Jezek [2004], are an appropriate first choice.

The application of InSAR on a fast moving glacier has it downsides. The environment is often subject to precipitation, which causes decorrelation between the images. Also, due to foreshortening and shadowing effects caused by steep topography, the edge of the glacier can be difficult to extract. The aforementioned methods are therefore not applicable to this research area.

A new approach to pixel selection is introduced here. A combination of a phase gradient filter and coherence thresholding leads to masked areas. The phase gradient filter uses the phase difference between neighboring pixels to mask or keep a pixel. The neighborhood can be of any size, but a square 3- or 5-pixel window has proven to give satisfiable results. If a neighbor has a phase difference larger then the input threshold (0.5π), the window center-pixel is masked. By moving the window over the entire image a phase gradient mask is obtained, see Figure 4.7 (A).

Generally a coherence map is derived during interferometric processing. By setting a minimum coherence value a second mask can be produced, of which an example is visible in Figure 4.7 (B). When the phase gradient and coherence map are combined (Figure 4.7 (C)) the result can be buffered using a square 3-pixel moving average filter, see Figure 4.7 (D).

To obtain a final mask, as visible in Figure 4.7 (D), small patches and holes have to be removed or closed respectively. Applied to a wrapped LOS interferogram, the algorithm masks out noisy and deforming patches. The final output can be used for a variety of applications, including masking for interpolation (Section 4.3). When inverted and appropriately adjusted, it can be used as window selector for cross correlation operations.

4.3 2D directional Fast Fourier Transform Interpolation technique for ionopsheric phase filtering

When acquiring data using spaceborne SAR, the radio signal travels through the atmosphere where it gets delayed or defracted [Hanssen, 2001]. As part of the atmosphere, the ionosphere is a layer between 60 and 600 km height. Within this shell, *ionozation* is taking place due to extreme ultraviolet and X-radiation from the Sun [Rees, 2001]. A measure for the intensity of the ionization is the total amount of electrons per square meter. This parameter is called the Total Electron Content (TEC). One TEC unit is equal to 10^{16} electrons/m^2. The total

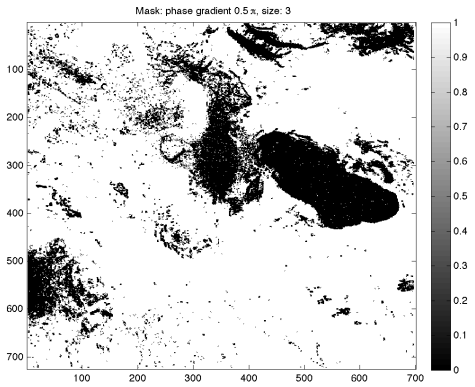

(A) Phase Gradient mask (size: 3)

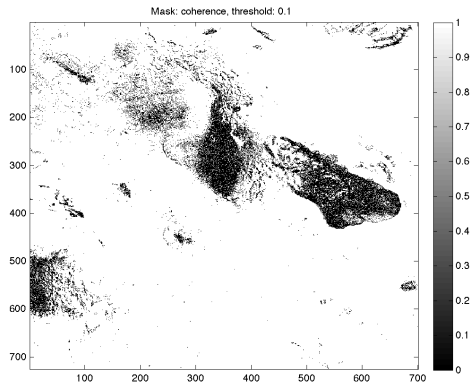

(B) Coherence mask (threshold: 0.1)

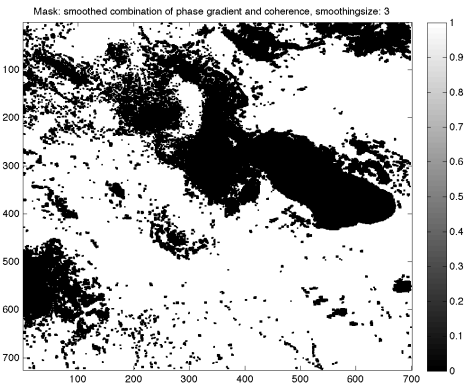

(C) Buffered version of (A) and (B)

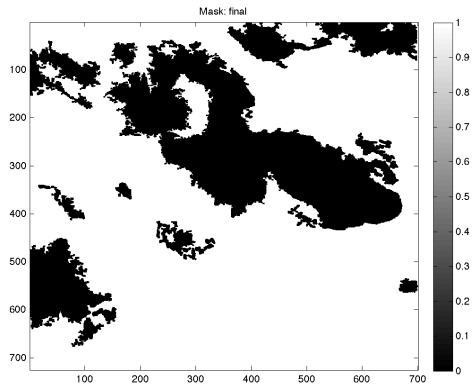

(D) Final mask

FIGURE 4.7: Different stages of the masking procedure. (A) shows the result of a square 3-pixel gradient mask with a threshold between neighboring pixels of 0.5π. (B) shows the result of a mask based on a coherence threshold of 0.1. (C) is the combination of (A) and (B), buffered using a 3-pixel moving average filter. Many small patches are distributed over the image and large masked areas still contain holes. These are removed or closed respectively, according to a threshold on the patch area. The end result can be seen in (D).

signal delay due to ionosphere can then be estimated by integrating the TEC value over the entire path length in slant range, according to [Hanssen, 2001]:

$$\delta_{iono} = \frac{-40.28}{f^2} M(\theta) TEC, \tag{4.4}$$

where δ_{iono} gives the slant range delay in meters, f is the frequency of the signal and $M(\theta)$ a mapping function to convert the signal zenith delay to slant range delay. This mapping function is dependent on the incidence angle θ, that can vary per acquisition.

The SAR and InSAR community focusses mainly on the influence of tropospheric disturbances in the LOS direction. However, it has been shown by several

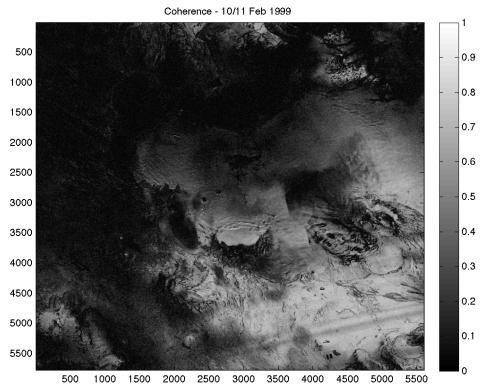

FIGURE 4.8: The coherence of the 10/11 February 1999 interferogram is reduced, e.g. in the lower right corner of the image, because of azimuthal shift errors due to ionospheric streaks. The strongest disturbances visible in the SD outcomes for this pair correspond to the areas where there is reduced coherence.

(e.g. Gray et al. [2000],Wegmuller et al. [2006] and Jung et al. [2009]) that ionospheric electronic density variations along the synthetic aperture causes positional shifts in azimuth. The application of cross correlation and split-bandwidth methods to SAR data in the along track direction make these *streaks* visible.

Gray et al. [2000] were the first to link the presence of the distortions to variations in the magnetic field when processing interferometric data with ICC. Since the magnetic field is related to ionospheric activity, the streaks are directly linked to the ionosphere. Magnetometers located nearby the edges of the satellite swath showed activity correlating to disturbances visible in acquired ERS1-2 tandem data. Gray et al. [2000] also note the presence of the phase 'scintillation' specifically in high latitude- or auroral zones. This is later confirmed by i.a. Meyer [2010]. However, the appearance and the shape of the ionosphere fluxes in these regions is not investigated in great detail.

With the use of Equation 4.4, the ionospheric delay can in theory be estimated for the forward and backward looking interferogram, as retrieved by SD processing, separately. For this, Global Ionopsheric Maps (GIM) are needed to quantify the TEC values. The resolution of GIMs is 5° in longitude and 2.5° in latitude. This is too coarse for estimating a difference over the entire azimuth bandwidth, making a separate estimation of the ionospheric delay for band split interferograms impossible. Wegmuller et al. [2006] identified similar errors in L-band imagery used for glacier motion monitoring in the arctic. The effect is larger when larger wavelengths are used, because of the dependence of Equation 4.4 on the frequency of the SAR system. Apart from identifying the anomalies, Wegmuller et al. [2006] proposed to correct speckle tracking results by means of directional filtering and spatial interpolation. The interpolation is applied on regions masked by a coherence threshold combined with LOS motion data. Hu et al. [2012b] uses SD to obtain azimuth offsets and interpolates rejected pixels in the area of interest through directional Kriging. A full overview of correction methods in low-frequency SAR signals is given by Meyer [2010].

The ionospheric streaks distort the signal of interest in the data pairs previously introduced in Section 4.1. If the ionospheric mis shifts are large enough, the interferometric coherence is affected by it, as is visible for the 10/11 February 1999 pair in Figure 4.8. In order to get an error free estimation of the glacier flow field, the disturbances have to be removed. However, the sparse availability

of coherent, non-moving pixels in the available data creates large gaps. The aforementioned interpolation methods, like Kriging, are not capable enough to cope with this shortage of usable pixels. Consequently, a *directional 2D Fast Fourier Transform (FFT) interpolation* method is introduced that filters out the low frequency data using the spectral properties of the signal. A method is designed that can cope with the scarcity of useable pixel patches.

The interferometric and consecutive SD processing is adapted from the method of Bechor and Zebker [2006]. Instead of band splitting raw data and carrying out two interferometric processes for the upper- and lower band images separately, a SD interferogram is obtained by splitting the azimuth bandwidth when the whole master and slave are processed according to the standard DORIS steps until the slave is resampled onto the master. For a more extensive discussion on the (pre-)processing, see Chapter 2 and Subsection 4.1.1.

Perpendicular baseline differences between the upper- and lower band interferograms leading to flat-Earth or topographic phase residuals, are not corrected. Any phase ramps corresponding to this geometrical difference cannot be seen in the data, so corrections suggested by Jung et al. [2009] are not necessary.

An overview of the processing steps after generating a SD interferogram in azimuth can be found below. They correspond to the subfigures visible in Figure 4.9.

1. *Spatial averaging of different looks* (Figure 4.9 (A)): first, heavy phase filtering is needed to obtain a smooth SD interferogram. By 'taking looks' or applying a moving average filter with a windowsize of 40 (azimuth) by 8 (range), a large component of the random noise apparent in the interferogram is removed.

2. *Application of a phase filter* (Figure 4.9 (B)): Goldstein filtering [Goldstein and Werner, 1998] is subsequently needed to obtain a clear image with visible ionospheric streaks. The filtering intensity factor α (range 0 - 1) varies from 0.5 to 0.9 dependent of the presence of random noise in the different SD interferograms.

3. *Smart Pixel Selection masking procedure* (Figure 4.9 (C) and (D)): The areas with low coherence ($\gamma < 0.3$) and obvious displacement are masked to zero by applying the masking procedure as discussed in Section 4.2. The LOS interferogram is needed in the Smart Pixel Selection procedure to mask out unusable pixels.

4. *Application of the 2D directional FFT interpolation method* (Figure 4.9 (E)): After zeropadding the image in the time domain the result is transformed into the frequency domain. A lowpass filter is implemented, the strength of which is dependent on the size of the zeropadded input image, according to Equation 4.5. This Butterworth filter has shown to give satisfiable results for the particular application of removing the streaks. Dependent on the

desired outcome, this can be changed to a more appropriate filter.

$$|H(D)|^2 = \frac{1}{1 + \left(\frac{D}{D_0}\right)^{2n}} \tag{4.5}$$

Where $|H(D)|^2$ equals the squared magnitude response. D represents the distance of every pixel in the filter matrix to the center, where the main lobe is located. D_0 is a constant value to size up or scale down the strength of the filter. Exponent n describes the order of the filter. A higher order results in a sharper main lobe. This parameter can also be used to tweak the filter, but is generally 1. Directionality is taken into account by rotating the filter according to the main angle of the streaks with respect to the range direction. The filter is applied to the noisy data by multiplication in the frequency domain. The depadded result returns only the low frequency components and interpolates the masked areas.

5. *Obtaining the final corrected SD inferogram* (Figure 4.9 (F)): The full image containing the interpolated ionospheric streaks is subtracted from the original Goldstein filtered image to obtain a corrected SD interferogram.

The 2D directional FFT interpolation algorithm as introduced is applied to the other data pairs to test its behavior. Ionospheric streaks are apparent in all four pairs, however with different intensity. By applying the method we are able to eliminate the major distortions as visible in Figure 4.10.

Limitations of the method are obviously displayed in Figure 4.10, where an overview of the application of the filter on the other interferometric pairs is given. These are:

- Bended streaks as visible in Figure 4.10 (E) are hard to filter out completely. A solution would be to apply the algorithm on patches assuming linear behavior within the patch.
- When coherent or non-moving pixels are sparsely available this results in large masked areas. These are difficult to interpolate. Figure 4.10 (D) shows the resulting erroneous behavior. A maximum allowable size of the masked patch is not derived due to its dependence on the filter settings.
- Boundary issues - masked areas near the edge of the image - as present in Figure 4.10 (F) can be solved by mirroring, translating and flipping. To obtain a better interpolation the streaks need to continue on the other side of the edge.

By applying the 2D directional FFT interpolation the reduction of ionospheric features is clearly visible by eye. To support this, a gross statistical analysis is presented here. From the 26/27 January 2000 pair a subregion of 200 by 400 multilooked pixels is selected. This region is assumed to be stable taking the

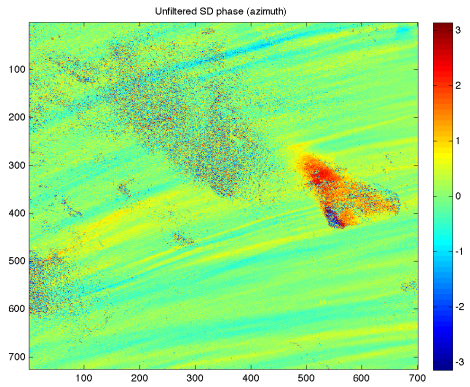

(A) Spatial averaged SD phase

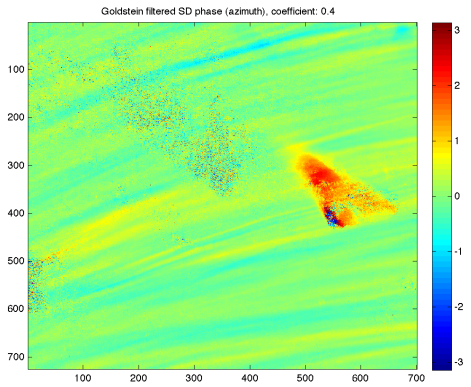

(B) Goldstein filtered SD phase

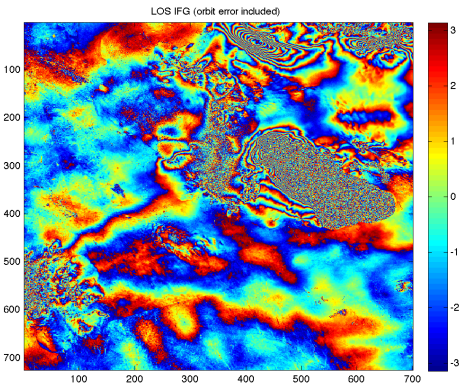

(C) LOS Interferogram

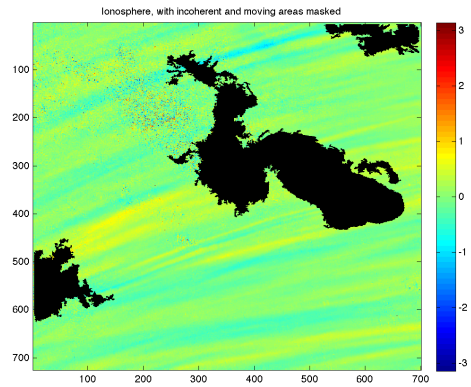

(D) Mask applied to (B)

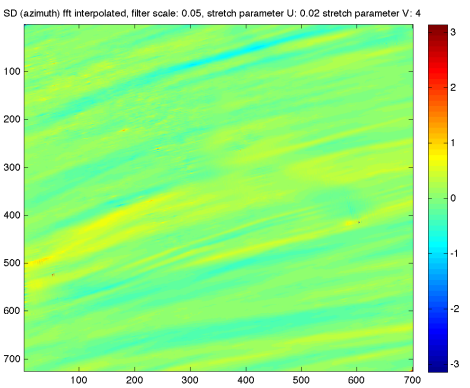

(E) 2D directional interpolated ionospheric streaks

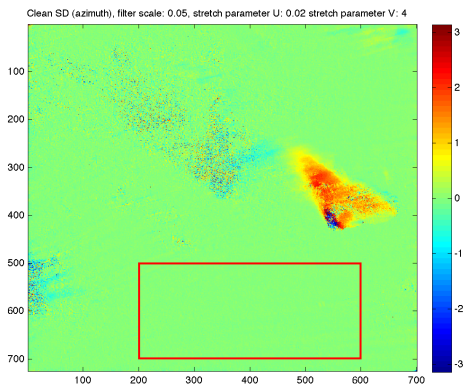

(F) Corrected SD phase: ((E) subtracted from (B)

FIGURE 4.9: Overview of filtering method as applied to ERS SD data with a temporal baseline of 1 day. Step 1 is to filter the outcomes of SD processing (A) with a Goldstein filter (B). Based on the LOS interferogram displayed in (C), a mask is applied to (B) leading to (D). The masked areas are interpolated (E) using the 2D directional FFT interpolation method. This leads to a corrected SD phase, displayed in (F). The red box in the latter indicates the cutout region used to determine gross statistics, as can be seen in Figure 4.11 and Figure **??**. All figures show interferometric phases (LOS or SD) of modulo 2π.

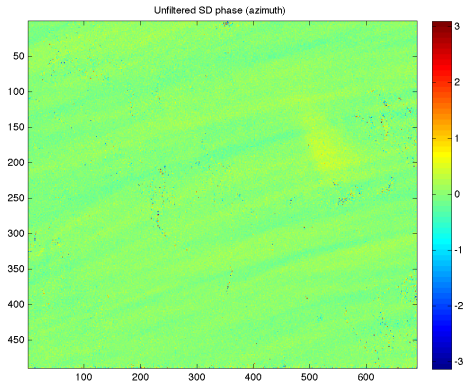

(A) 6/7 January 1999 - multilooked SD phase

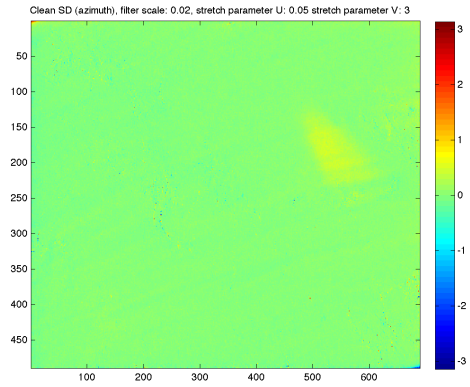

(B) 6/7 January 1999 - corrected SD phase

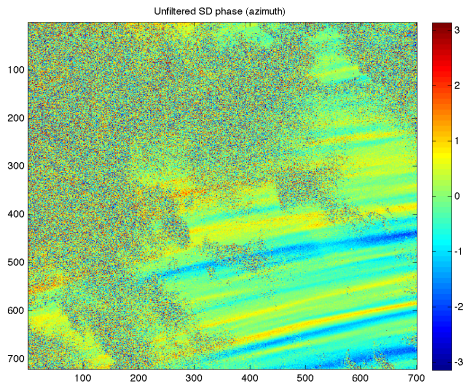

(C) 10/11 February 1999 - multilooked SD phase

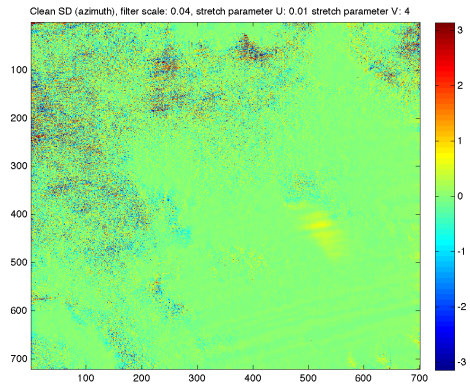

(D) 10/11 February 1999 - corrected SD phase

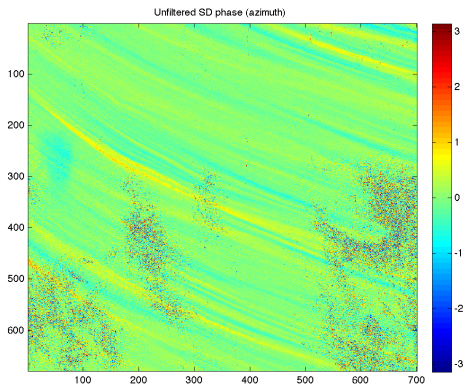

(E) 27/28 February 1999 (descending) - multilooked SD phase

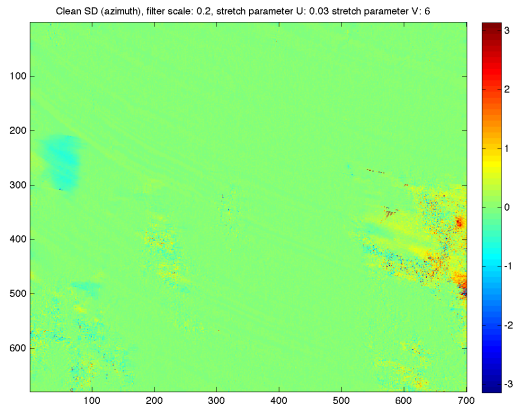

(F) 27/28 February 1999 (descending) - corrected SD phase

FIGURE 4.10: Applying the 2D directional FFT interpolation filter to the other data pairs will lead to the results displayed here. The figures on the left side (A), (C), and (E) show the multilooked outcomes of the SD processing. The figures on the right, (B), (D) and (F), give the corrected results. All figures show SD phases of modulo 2π.

1-day temporal baseline into account. In Figure 4.11 (A) the area is displayed in three different stages of the filtering process. The top figure shows the unfiltered SD phase, processed from the original output with a square 32 pixel moving average window. The corresponding histogram shows a very good fit with the predicted Gaussian distribution. A σ_{unfilt} of 0.24 radian is found and is reduced by Goldstein filtering to 0.18 rad. The ionospheric streaks are the most prominent source of error, with an intensity limit of maximum half a fringe. This holds for all the data pairs. When the distortions are removed by the 2D directional FFT interpolation filter, the standard-deviation improves almost two orders of magnitude to 0.045 rad.

After each filtering step, the removed noise can be isolated by subtracting the filtered result from the outcome of the previous step. By doing this, three different noise levels can be identified. When the SD outcomes are mutlilooked or spatially averaged, the overall noise level is reduced significantly (see Figure 4.3). This 'speckle'-alike noise is filtered out more by applying the Goldstein filter. The ionospheric streaks are now clearly visible and will filtered out by the 2D directional FFT interpolation. The remaining Gaussian distributed noise is insignificant with a standard deviation in the order of 0.001 - 0.05 rad, and will therefore remain in the SD interferogram. The value of the remaining noise will be used in Chapter 6 to test a glaciology method with synthetic data.

* * *

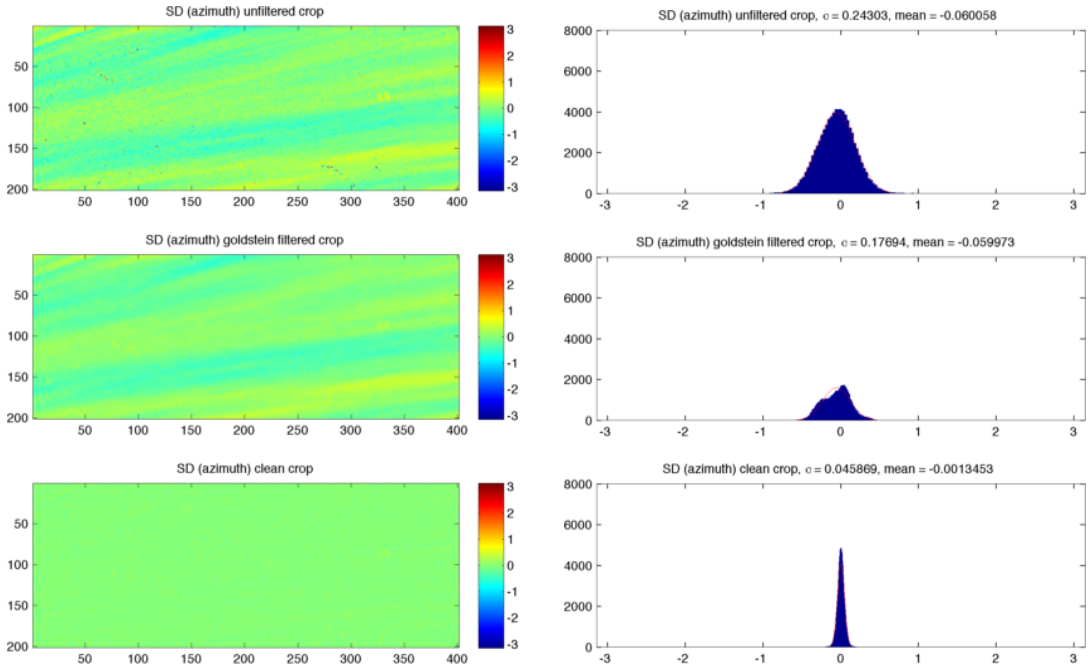

FIGURE 4.11: A cutout of the SD interferogram, Figure 4.9, has been made to test the noise reduction in different stages of the filtering method. All figures show SD phases of modulo 2π. A high coherent region is selected where there no deformation present. (A) displayes the cutouts that have been made. The top shows the unfiltered SD phase. The result after Goldstein filtering is displayed in the middle. The lower plot shows the cutout after the 2D directional FFT interpolation filter. (B) shows the corresponding histograms. The reduction in standard-deviation is obvious. From (A) to (B) the standard-deviation improves $\pm 33\%$. From (B) to (C) the standard-deviation almost improves an order of magnitude.

Part III

GLACIOLOGY

Chapter 5

Adaption and testing of a Markov Random Field method optimized with Simulated Annealing for deriving 3D glacial flow

In this chapter a model is introduced that is used to derive 3D motion fields of glaciers. The physical background behind and adaptations made to the model will be discussed in Section 5.1. Before applying it to real data sets, as will be done in Chapter 6, the model is evaluated for its limitations using synthetic data. To test the functionality of the algorithm, artificial input data is generated in close accordance with the real data that is used in this thesis. The derivation of the simulated data can be found in Section 5.2. With the simulated data the model is tested for its response to several problems that occur when dealing with real data. The setup of the testing procedures and the assessment of the outcomes will be presented in Section 5.3.

5.1 Background to the glaciologic optmization technique

To investigate the influence of subglacial water flow on the motion of a temperate glacier, Magnússon et al. [2010] and Magnússon et al. [2011] used a minimum energy model to derive 3D flow fields. MRF regularization optimized with Simulated Annealing was implemented to iterate to a solution. In MRF an image is interpreted as a network of random variables, where the value of each pixel in an image is only dependent on its nearest neighbors. To find the optimal value for each pixel, i.e. a global optimum for given functions and boundary conditions, Simulated Annealing [Metropolis et al., 1953] is implemented.

The naming of the Simulated Annealing method is based upon the procedure of the annealing of solids, a process where a material is heated past the melting point and cooled gradually to alter the form or the structural properties of the material. To better understand the basic principle of the method, an analogy with a ball that bounces over a mountainous area is used. The landscape is defined by the different energy states of the combination of equations that describe

the physical process, to which a solution can converge. The goal is to find the deepest valley, or the state where there is the least energy in the system. The procedure starts with a high temperature, causing the ball to make very high, random, bounces. In this way, the ball is able to explore the landscape easily in search of the deepest valley. By gradually lowering the temperature, the ball bounces less en less high, eventually converging to a solution. Simulated annealing solves the optimization problem by allowing worse moves, to escape from local minima according to an acceptance distribution, which is defined probabilistically. The height of the bounces and the allowance of lesser quality moves is dependent on the temperature. By lowering it according to a cooling schedule, the system converges to a optimal solution.

The ball in the case of the derivation of 3D flow fields is the value of a pixel, which is randomly changed during the optimization procedure. The size of the random change is dependent on the temperature and the cooling rate that are input variables in the algorithm. The landscape is equal to all possible solutions of the MRF optimization problem, but constrained by the different energy functions that describe glacial flow, which will be discussed hereafter. It is important to note that when a pixel value has changed, the neighboring pixels in the MRF are affected too. More details on the particular implementation of the glaciology method can be found in Magnússon [2008] and Gudmundsson [2002].

In the initial design of the aforementioned model the input consisted of multiple InSAR observations. A combination of ascending and descending LOS data provided two out of a minimum of three equations to constrain 3D motion. Gourmelen et al. [2011] recently used the reinvented MAI-technique to derive 3D motion fields of the Hofsjökull and Langjökull ice cap, both located in Iceland. This triggered the possibility of extending the MRF method to be able to use both the LOS as well as the azimuth displacements from one interferometric pair. By applying Spectral Diversity in azimuth direction in combination with normal LOS interferometry, two components of the necessary three velocity vectors can be solved for with one InSAR pair. Areas that are sparsely monitored by satellite acquisitions and thus suffering from a lack of combined ascending- and descending image tracks, can now be examined.

Using the equations for decomposing LOS-, v_{los}, and azimuth velocities, v_{azi}, into three separate velocity vectors in East-, North- and Up-direction, respectively v_e, v_n, v_u, the following underdetermined system of equations can be written:

$$\begin{bmatrix} v_{los} \\ v_{azi} \end{bmatrix} = \begin{bmatrix} \cos\alpha \sin\theta & \sin\alpha \sin\theta & \cos\theta \\ \cos\left(\alpha + \frac{\pi}{2}\right) & \left(\alpha + \frac{\pi}{2}\right) & 0 \end{bmatrix} \begin{bmatrix} v_e \\ v_n \\ v_u \end{bmatrix} \tag{5.1}$$

where α represents the azimuth look angle measured relative to the east, and θ the incidence angle. To solve this system of equations for one InSAR pair, constraints have to be added.

One possible constraint is the principle of mass conservation, as shown in Equation 5.2. Since the assumption has been made that there is nothing added or taken away during time interval separating two acquisitions, there is no part

of the formula related to accumulation, runoff or melting. Simulations with synthetic data in Section 5.3 will shine more light on the correctness of the mass continuity postulation. The principle of mass conservation is expressed as:

$$v_e \frac{\partial Z_s}{\partial x} + v_n \frac{\partial Z_s}{\partial y} - v_u = \frac{\partial (FHv_e)}{\partial x} + \frac{\partial (FHV_n)}{\partial y} \tag{5.2}$$

where F is the ratio between the average horizontal velocity in a vertical ice column and the surface velocity. A value of 0.8 means pure deformation is assumed, a value of 1.0 means pure basal sliding according to Cuffey and Paterson [2010]. H equals the ice-thickness, which is the difference between the surface elevation and the bedrock DEM. The right hand side of the equation is referred to as the flow divergence, which is the sum of all extensions and compressions in the ice flow [Cuffey and Paterson, 2010].

In the MRF with Simulated Annealing algorithm energy functions are used to converge to an optimal solution. Formulas 5.1 - 5.2 are expressed in energy functions as follows:

$$E_{v_{los}}(v_e, v_n, v_u) = (v_e \cos\alpha \sin\theta + v_n \sin\alpha \sin\theta - v_u \cos\theta - v_{los})^2 \tag{5.3}$$

$$E_{v_{azi}}(v_e, v_n) = \left(v_e \cos\left(\alpha + \frac{\pi}{2}\right) + v_n \sin\left(\alpha + \frac{\pi}{2}\right) - v_{azi}\right)^2 \tag{5.4}$$

and:

$$E_{mc}(v_e, v_n, v_u) = \left(v_e \frac{\partial Z_s}{\partial x} + v_n \frac{\partial Z_s}{\partial y} - v_u - filt_{box}\left(\frac{\partial (FHv_e)}{\partial x} + \frac{\partial (FHV_n)}{\partial y}\right)\right)^2 \tag{5.5}$$

The flow divergence in Equation 5.5 is filtered using a 500 m box-filter. This filtering is required because of errors in the bedrock topography causing spikes in the flow divergence. To avoid the propagation of these errors in the 3D flow estimation, the flow divergence is filtered. A value of 500 m is reasonable taking computational efficiency into account. A smaller value is no option since variations in the flow divergence over a length scale less then the ice thickness are physically unlikely [Magnússon, 2008].

Next to the mass continuity equation other constraints are added. Two energy functions are added to the overall energy function to obtain spatially smooth results. The second derivative of the horizontal and vertical flow with respect to the grid resolution has to be minimized. They can be seen in Equation 5.6:

$$E_{diff}(v_e, v_n, v_u) = \left(\frac{\partial^2 v_e}{\partial x^2}\right)^2 + \left(\frac{\partial^2 v_e}{\partial y^2}\right)^2 + \left(\frac{\partial^2 v_n}{\partial x^2}\right)^2 + \left(\frac{\partial^2 v_n}{\partial y^2}\right)^2 + \\ + \left(\frac{\partial^2 v_u}{\partial x^2}\right)^2 + \left(\frac{\partial^2 v_u}{\partial y^2}\right)^2 \tag{5.6}$$

To prevent the ice flow from going up slope a flow directionality constraint is implemented. The horizontal flow direction ψ is estimated using the gradient of a smoothed DEM and is measured counter clockwise to the east. Unit velocities $v_x = \cos\psi$ and $v_y = \sin\psi$ are derived to be used as reference for the estimated flow direction in Equation 5.7.

$$E_{dir}(v_e, v_n) = \left(v_n v_x - c_{dir} v_e v_y\right)^2 \tag{5.7}$$

where c_{dir} is a switch strongly discouraging flow up-slope by enabling a value of -10 when the flow is against the pre-estimated flow direction, and 1 otherwise.

With all the input equations and constraints now defined, the sum of all the components is displayed in Equation 5.8. This total energy has to be minimized to find the most optimal solution.

$$\begin{aligned} E(v_e, v_n, v_u) = E_v^{los}(v_e, v_n, v_u) + w_{azi} E_v^{azi}(v_e, v_n) + w_{mc} E_{mc}(v_e, v_n, v_u) + \\ + w_{dV} E_{diff}(v_e, v_n, v_u) + w_{dir} E_{dir}(v_e, v_n) \end{aligned} \tag{5.8}$$

Not all components in Equation 5.8 have equal importance. The individual energy equations are weighted by the azimuth coefficient w_{azi}, the smoothness coefficient w_{dV} and directionality factor w_{dir}. In the implementation of this method w_{mc} can be either 1 or 0, corresponding to using or discarding the mass continuity equation as an extra constraint. w_{azi} weighs the azimuth component based on the noise level apparent in the SD results. For all initial computations this factor is assumed to be 1. An assessment of the influence of all coefficients is discussed in Section 5.3.

5.2 Simulating input data

To test the functionality of the glaciology model, simulated input data of a glacier is created. The implementation of a velocity field covering all possible directions is key to measure the specific response of the model in the directions parallel to the LOS- and azimuth directions. The satellite geometry is copied from the ERS satellites, using an ascending orbit where the SAR system is right looking. Assumptions that are made are listed below:

- a maximum $1\,\mathrm{m\,d^{-1}}$ of horizontal ice motion, corresponding to the expected ice flow of the 6/7 January 1999 pair, is assumed radially. This implies velocities of $0\,\mathrm{m\,d^{-1}}$ at the top and margin of the glacier
- a simple cone with a height of 300 m and a square base of 112x112 pixels is assumed as DEM, Z_s. Each pixel has a size of 100x100 m, since the model assumes a resolution cell size of 100x100 m. The resulting slope is about 3°
- flat bedrock is assumed. So the ice thickness H equals Z_s

- F is approximated as 0.9, assuming an equal contribution of pure basal sliding and pure ice deformation
- where there is noise added to the phase in azimuth direction, simple Gaussian distributed noise with a standard deviation of $0.3\,\mathrm{m\,d^{-1}}$ is applied. This corresponds to the noise level of the 6/7 January 1999 real data
- A grid of individual incidence angles θ, varying between 20° (first pixel) and 22° (far range) is defined. For simplicity an azimuth angle α of 0° is set

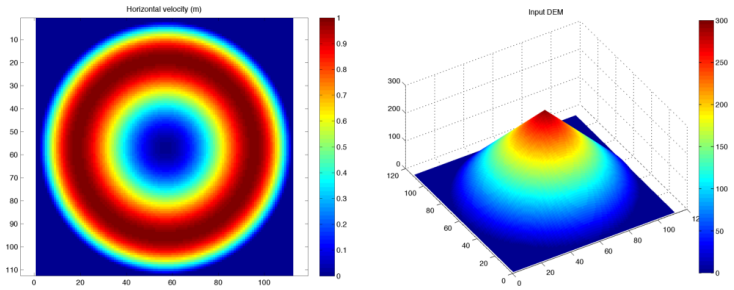

(A) v_{hor} (B) DEM

Figure 5.1: Two initial assumptions to derive LOS and azimuth phases for simulation purposes are visible in this figure. (A) shows the assumed horzontal velocity field v_{hor} with a maximum flow of $1\,\mathrm{m\,d^{-1}}$. In (B) the simple input DEM with a height of 300 m can be seen.

The up-component is calculated using the mass-continuity equation (5.2), expressed in the unknown v_{up}. The DEM needed for this can be seen in Figure 5.1 (B). The resulting three velocity components can be seen in Figure 5.2. Subsequently, the LOS and azimuth velocities are found by applying Equation 5.1. These are converted into phase using the MAI formula, assuming a perfect square band filtering with a split bandwidth factor $n = 0.5$.

$$d_{los} = -\frac{\lambda}{4\pi}\Phi_{los} \qquad \text{(Equation ??)}$$

and

$$d_{az} = \frac{1}{n}\frac{l}{4\pi}\Phi_{azi} \qquad (3.24)$$

respectively. The resulting unwrapped LOS and azimuth phases can be seen in Figure 5.3.

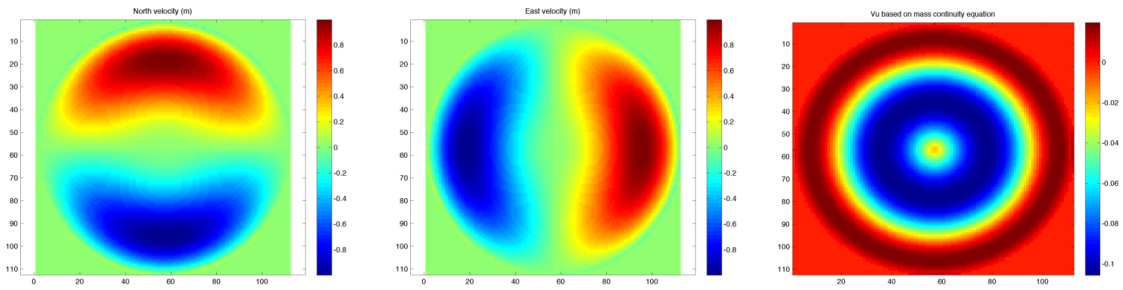

(A) v_n (B) v_e (C) v_u

Figure 5.2: The three velocity components deduced from the horizontal input velocities (Figure 5.1 (A)) are displayed here in meters per day. (A) represents the north component, (B) the east component and (C) the up component of the 3D flow field.

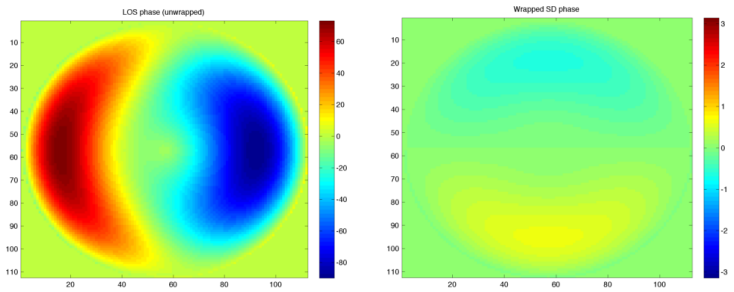

(A) LOS phase (B) azimuth SD phase

Figure 5.3: The LOS phase, (A), and the azimuth SD phase, (B), to be used as input for testing the glaciology model.

5.3 Assessment of method output data and corresponding performance indication

Using the simulated data introduced in Section 5.2, the MRF with Simulated Annealing is tested to constrain real input data. For this reason basic properties of real data are taken as a starting point to test the glaciology method. As Equation 5.8 shows, the total energy equation consists of several separate contributions each weighted according to their importance. How the different parts should be weighted is part of the performed tests. Also, it is suspected that the algorithm has difficulties solving for motion parallel to the LOS direction when the mass continuity equation is not applied. In case Equation 5.5 is left out of the full energy equation, it is not possible to distinguish between the vertical and horizontal component when the horizontal motion is parallel the LOS. The random character of the method results in a 'growing' effect on the vertical and/or the horizontal component. To what angle from the LOS direction this issue is present is tested by applying different angular masks. Lastly, to test the error

propagation properties of the model, a random noise level is added to the azimuth component of the signal. This Gaussian distributed signal equals the total noise level present in the real data of 6/7 January 1999.

In the following overview the different testing procedures are listed:

1. Test to determine the influence of the different weighting options on the derived outcomes. This is done by adjusting w_{mc} to be either 0 or 1, corresponding to the use or disregard of the mass continuity equation as extra motion constraint. w_{dir} is varied from 0.1 to 1 by steps of 0.2 when $w_{mc} = 0$ and 0.01 to 0.05 when $w_{mc} = 1$. w_{dV} is changed from 0.1 to 1.0 by steps of 0.2, irrespective of the use of the mass continuity equation.

2. Test to determine to which angle the input phases have to be masked to avoid unlimited growth of the horizontal and vertical motion in the direction parallel to the satellite's LOS. The setup involves the implementation and application of a 5° and 10° angular mask to the simulated data. The same testing parameters as discussed under item 1 will be used.

3. Test to determine how potential errors in the input data propagate to the model outcomes. A Gaussian noise signal equal to $0.3\,\mathrm{m\,d^{-1}}$ is added to the azimuth SD phase. With a predefined maximum velocity of $1\,\mathrm{m\,d^{-1}}$ this leads to a SNR of 3.33. Results with and without the mass continuity equation turned on and with the same set of testing parameters as discussed under 1 and 2, will be derived.

Results of testing procedures using 'clean' input data

When 'clean' (no noise is added) phase data is put into the model, the output of the model is in very good agreement with the input data. In Figure 5.4 the results can be found in the column most left, compared with the input data in the middle column. The third and most right column shows the residuals, or the difference between the original and the derived velocities. The different weighting coefficients applied to the total energy equation are: $w_{mc} = 1$, $w_{dir} = 0.03$ and $w_{dV} = 0.1$. In the residuals a ring with a thickness of 2-3 pixels can be distinguished. During the run of the model a mask is applied to make sure no NaN's remain that can distort the execution of the model. Thus, the area of the input data is a little larger than the output of the model. So, by ignoring this ring in the interpretation of the figures, it can readily be seen that **the derived velocity components are in good agreement with the simulated velocities**.

When the mass continuity equation is turned off, as discussed before, it is impossible to distinguish between the horizontal and vertical component when the flow is parallel to the LOS. Leakage from the horizontal component into the vertical velocity vector occurs. This effect can be seen in the column far left in Figure 5.5, where both components are displayed. The horizontal velocity plot

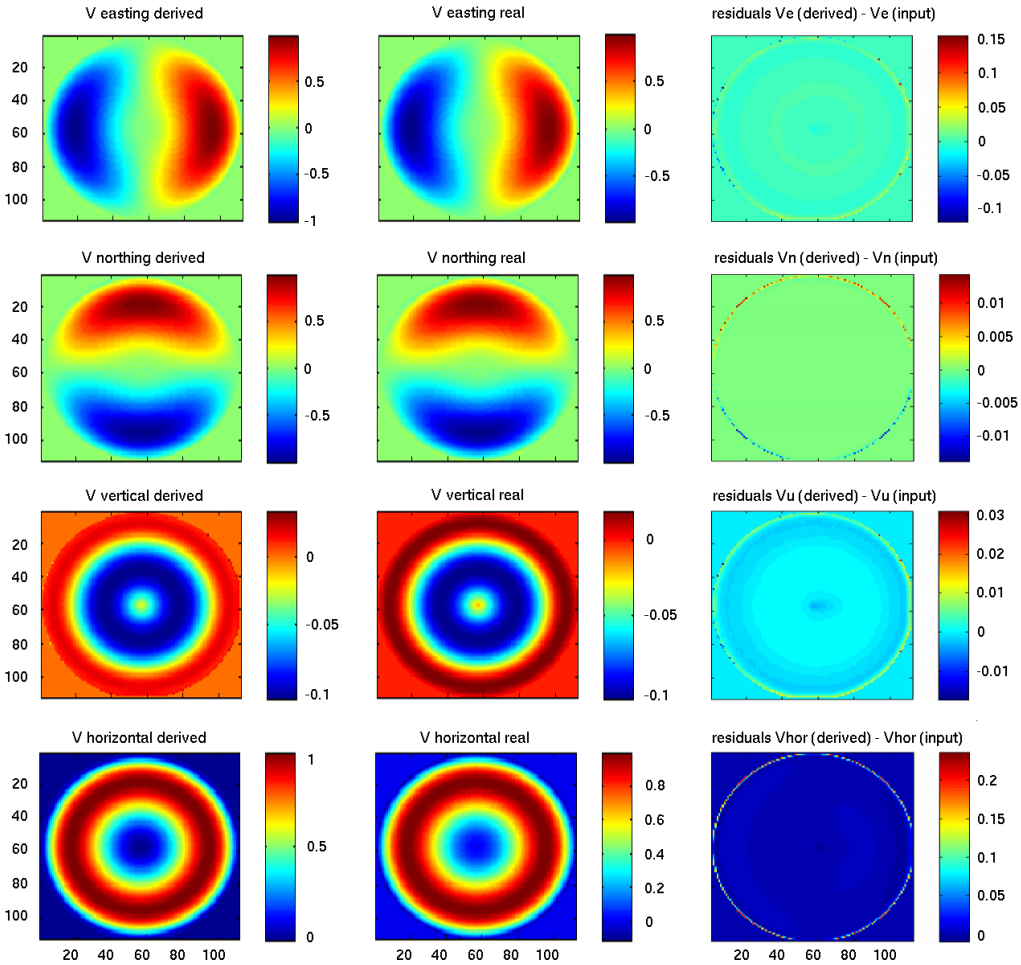

Figure 5.4: An overview of the model outcomes, in meters per day, by running it with the synthetic input data presented in Section 5.2. In the left column the derived velocities are displayed. The original input data can be seen in the middle column with the corresponding residuals of the input and derived data in the column on the right. Apart from some pixels at the edge (visibile because of a circular mask applied during the model execution), the residuals velocities are in the order of . The weight coefficients corresponding to Equation 5.8 are: $w_{mc} = 1$, $w_{dir} = 0.03$ and $w_{dV} = 0.1$.

shows a data distortion, or gap, on the west and east side of the simulated glacier. At the same locations in the vertical velocity plot higher values are found. Figure 5.6 shows the residuals belonging to Figure 5.5. With these two figures the influence of masking certain phase directions can be assessed. Angular masks of 5 and 10° from the LOS direction (purely east) are applied to the input SD and LOS phases.

Based on the outcomes of the simulations the conclusion can be drawn that **when the mass continuity constraint is not applied, an angular mask equal to or larger than 5° from the pure LOS direction is sufficient to mask out the main error**. A larger mask of 10° erases most of the error. When working with data where movement is expected to be in the LOS direction, a trade off has to be made between keeping slightly erroneous phases in to retain enough data or to mask all the distorted phases out. Generally, masking of phases within 10° would suffice.

To test the effect of the weight coefficients on the outcomes, simulations are carried out when the mass continuity equation is turned off an on. In the first case **the residuals are smaller when the weighting of the smoothing function, w_{dV}, is set to small values (± 0.1)**. This can be explained by errors introduced due to oversmoothing when there is no noise apparent in the model and a high weighting on the smoothing function is applied. **A small value for the flow directionality constraint, weighted by w_{dir}, results in smaller residuals** according to the Figure 5.7 (A). In this example the motion is well enough constrained by the input data to conclude that the flow directionality constraint, which serves as a substitute for mass continuity equation when turned off, forces the flow too much down slope. A smaller weight factor is therefore suitable.

When the mass continuity equation is turned on, by setting w_{mc} to 1, the influence of the weight coefficients is less determinable. This has most probably to do with a large weight of the mass continuity in the total energy equation, making the other constraints less influential. **Results show that the smoothing coefficient w_{dV} behaves similarly irrespective of leaving the mass continuity equation in or out**. Since both the mass continuity and the flow directionality constraint force the flow radially, a high weighting for both would distort the results. Thus, **in case of applying the mass continuity equation, the flow directionality constraint has to be an order of magnitude smaller** (e.g. $w_{dir} \approx 0.03$ instead of $w_{dir} \approx 0.3$).

Results of testing procedures using a fixed noise level

When noise is added to the input phases, the outcomes of the simulations results show that the weighting coefficients have to be set differently than discussed in the previous Subsection. The results without the mass continuity constraint are of bad quality, forcing the application of angular masking to prevent a combination of random noise and noise introduced by the lack of convergence (see Figure 5.5 and 5.6).

The residuals are smaller when a higher smoothing weight coefficient w_{dV}

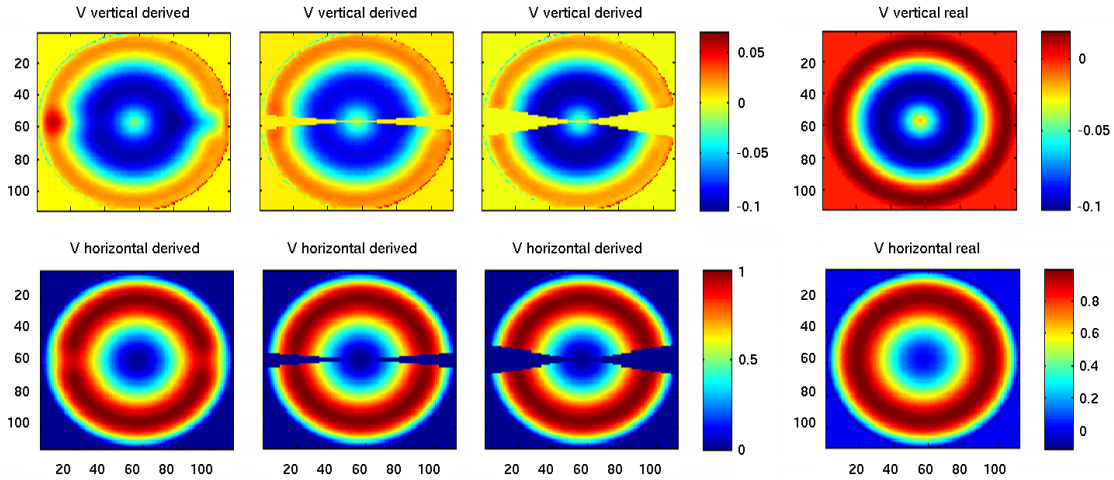

Figure 5.5: In this figure, the derived vertical and horizontal velocities with angular masking are displayed and compared to the original simulated input data. The three columns on the left show respectively no-, a 5°- and a 10° angular mask. Especially in the case where there is no mask applied, one can see erronous behavior in the direction of LOS. The corresponding residuals can be found in Figure 5.6. The weight coefficients are: $w_{mc} = 0$, $w_{dir} = 0.9$ and $w_{dV} = 0.1$.

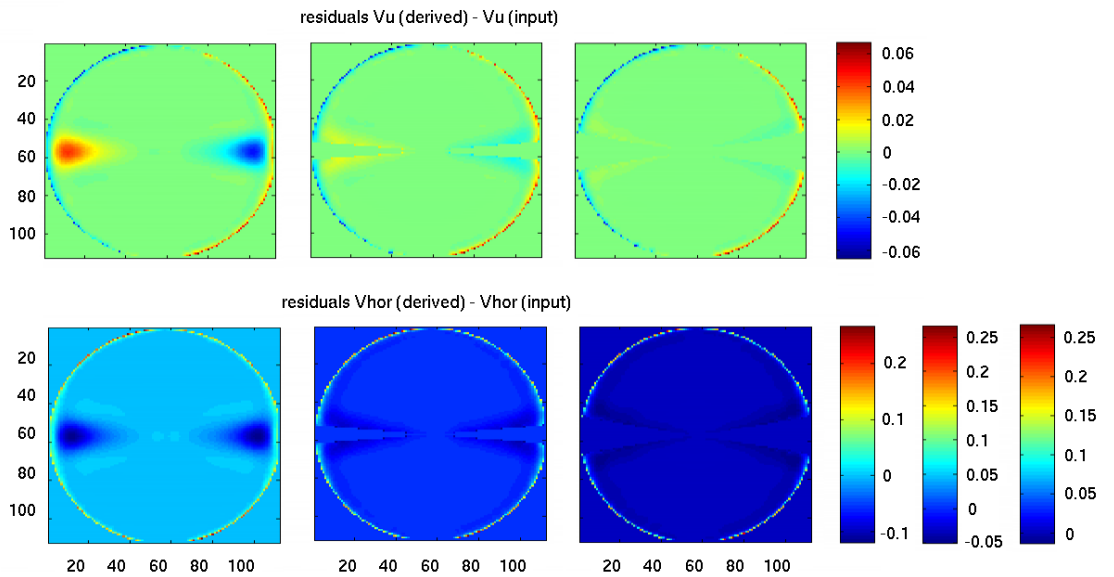

Figure 5.6: The residuals corresponding to the masking tests shown in Figure 5.5, are presented here. The influence of the masking procedure can be clearly observed. After applying a mask of minimum 5°, the effects are less explicit and almost dissapear when applying an ever larger angluar mask. A tradeoff has to be made between keeping data with some edge effects, or leaving all erronous data out.

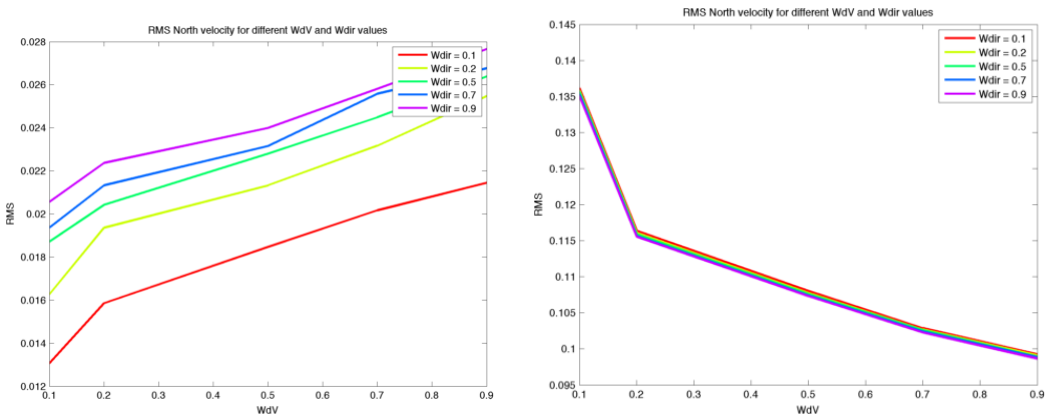

(A) without noise (B) with noise

Figure 5.7: RMS errors in $\mathrm{m\,d^{-1}}$ for synthetic data derived without (A) and with (B) Gaussian distributed noise ($\sigma = 0.05\ \mathrm{m\,d^{-1}}$) added to the azimuth component of the input data. The two graphs show opposite behavior for the smoothing weight factor w_{dV}.

is set, as is visible in Figure 5.7 (B). When enlarging the influence of the second derivative, the noise is smoothed out. Next, it has been found that **keeping the flow directionality factor w_{dir} low results in considerable less erroneous outcomes**. When the SNR is low, it is hard to distinguish between motion and noise. This results in wrong outputs when the weighting coefficient of the flow directionality is large.

The results for a run with the mass continuity equation added is shown in Figure 5.8. Corresponding to the simulations without noise, the impact of w_{dV} and w_{dir} is less profound, making it harder to draw conclusions. For comparison the same settings are used as in the 'no noise' simulations (Figure 5.4), resulting in applied weight coefficients of: $w_{mc} = 1$, $w_{dir} = 0.3$ and $w_{dV} = 0.1$.

As visible in Figure 5.8 the noise, which is only added to the azimuth component of the input phases, is influencing the result of all three motion components. This points to non-linear interdependency during the propagation of the error, of course related to the equations discussed in Section 5.1.

The standard deviations of the differences visible in Figure 5.8 are listed in Table 5.1. They show that the North component has almost the same standard deviation as the input noise ($0.189\ \mathrm{m\,d^{-1}}$). The application of the smoothing Equation 5.6 results in a somewhat lower value.

$\sigma_{v_{e,residuals}}$	0.038 m	RMSE v_e	0.023 $\mathrm{m^2}$
$\sigma_{v_{n,residuals}}$	0.156 m	RMSE v_n	0.109 $\mathrm{m^2}$
$\sigma_{v_{u,residuals}}$	0.016 m	RMSE v_u	0.010 $\mathrm{m^2}$

Table 5.1: Noise statistics corresponding to the residuals that are showed in Figure 5.8. The input error is Gaussian distributed noise with a standard deviation of $0.189\ \mathrm{m\,d^{-1}}$.

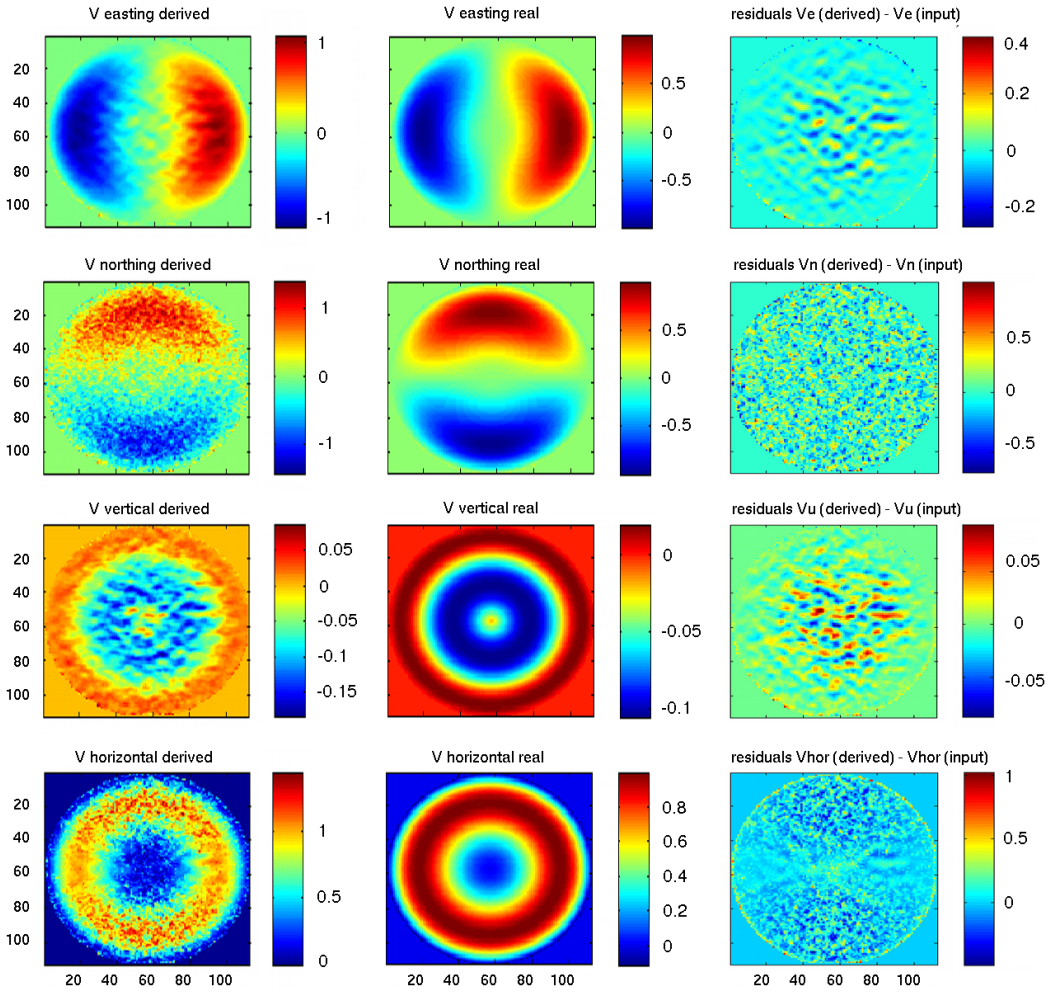

Figure 5.8: By adding noise to the azimuth SD phase, the model can be evaluated for its error propagation characteristics. Gaussian noise of $0.3\,\mathrm{m\,d^{-1}}$, equivalent to the total noise level in the real SD interferograms, is added. Similar to Figure 5.4, the left column shows the derived velocities, the middle one shows the intended results and the right one shows the residuals of the former two, all in meters per day. The applied weight coefficients are: $w_{mc} = 1$, $w_{dir} = 0.3$ and $w_{dV} = 0.1$.

* * *

Chapter 6

Derivation of 3D flow fields to assess the subglacial hydrology during surges

The contents of this chapter follow the work as presented in preceding chapters. The Markov Random Field (MRF) method with Simulated Annealing, as presented in Chapter 5, is used with previously (see Chapter 4) filtered (In)SAR data to derive 3D velocity components of a glacier in surge.

First, some background on surge dynamics is given. This is followed by an overview of ongoing research and corresponding findings of the most recent surge of Dyngjujökull, the glacier under investigation, in Section 6.2. The outcomes and corresponding interpretations of the model runs with the available real input data, are presented in Section 6.3.

6.1 Overview of surge dynamics

Glaciers come in many different shapes, sizes and locations. The ice masses on Iceland have areas smaller than 50.000 km^2 and can therefore be classified as *ice caps*. They are temperate glaciers [Björnsson and Pálsson, 2008], meaning that the glacier is at the pressure melting point from its base to its surface. Most of them are lying on top of active volcanoes and geothermal active areas. Despite the presence of ice and underlying geothermal activity, the combination between them is never seen as a main reason for the occurrence of *surges*. During a surge ice velocities can increase more than 100 times the velocities which are normal in a more quieter period. On average, the increased flow causes the glacier to advance several kilometers. Taken the periodic repetition of surges into account, these events are thought of as efficient long-term ablation mechanisms.

Many of the large outlet glaciers of Iceland's main ice cap Vatnajökull have a history of regular surges [Björnsson et al., 2003], [Adalgeirsdottir et al., 2005]. Björnsson et al. assessed all mayor surging outlet glaciers in Iceland with remotely sensed- or fieldwork data from the last century.

Observations of glacier surges on Vatnajökull in the 1990's showed accelerating surface velocities 2-3 years before any visible signs of surging. The first visible sign is a thickening of the glacier in the so called *enhanced velocity zone*,

typically 10 km long. The surge is unquestionable onset when this *bulge*, generally several meters high, starts moving down slope with propagation velocities measured from $20-80\,\mathrm{m\,d^{-1}}$ [Björnsson et al., 2003]. Usually it takes less than 6 months to reach the terminus of the glacier. By then, the glacier starts moving forward. For most Icelandic surge-type glaciers, the advancing lasts several months. Other signs of starting surges are muddying of glacial rivers, an increased number of hydraulic outlets at the glaciers terminus and extensive crevasse formation.

Kamb [1987] was the first to introduce a physically sound explanation for the mechanism behind surges. During non-surging, or quiescent periods, the subglacial hydrology system is thought to be a *tunnel* system. Runoff and meltwater is discharged through a network of large semicircular tunnels. This is a very efficient way of transporting rain- or meltwater through the glacier towards the glacial outlet river(s). A key parameter is the water pressure. When flow rates are high, the local water pressures are low, pulling all the higher pressure water units towards these large outflow tunnels. When a surge is ongoing, the water outlet of the glacier changes drastically from several rivers into very many small streams [Cuffey and Paterson, 2010], which is related to a *system of linked cavities*. This second type of drainage system can be visualized best as an interconnected system of small chambers where water is collected [Björnsson, 1998]. The water is transported through small channels in the bed. Within the distributed cavity system, there is little or no tendency for these small channels to grow and develop a tunnel system because of the influence of the effective water pressure. This is further discouraged by the increased movement of the glacier. It is easy to imagine that a water flux is dispersed much more easily in a tunnel system than in a system of linked cavities. The drainage along the bed is slow and spatially spread causing the hydraulic system to conduct water with difficulty. As water pressure varies directly with the water flux, high pressures are required to drive water towards the outlets at the terminus of the glacier. This high pressure results in the distribution of water across the entire bed of the glacier, facilitating sliding of the glacier at the base by enhanced lubrication of the bed. At the end of the surge the glacial outlets show normal behavior again, indicating a restored tunnel flow. The formation of a tunnel system reduces the lubrication of the bed and thus reduces the rate of basal slip.

In short, as stated by Björnsson [1998], the hypothesis is that glacial surges may occur when the normal, rapid subglacial drainage is disrupted and a linked-cavity system spreads out beneath the glacier and persists for some time.

6.2 The surge of Dyngjujökull, 1997-2000

Dyngjujökull is one of the two major outlet glaciers on the Northern side of the largest ice cap of Iceland and is located between the active volcanoes Bárðarbunga (Western side) and Kverkfjöll (Eastern side). As all the large, 'flat' glaciers in Iceland, the bedrock is assumed to be soft in the receiving area (observations

after retreat of the glacier show softbed) and most probably hard more up slope (personal communication with E. Magnússon). It measures a length of about 40 km and a width of 25 km, leading to a total surface area of about 1040 km^2. Its surface elevation lies between 700 and 1650 m, with an average slope of 1.6°. The second longest river in Iceland, Jökulsá á Fjöllum, springs off next to Dyngjujökull and for the most part it is supplied by the glacial meltwater.

Surges have taken place around ± 1900, 1934, 1951, 1977 and 1999, indicating a quiescent interval of 20-30 years. The most recent surge of Dyngjujökull thus occurred in 1997 - 2000. This event was monitored before, during and after and is documented extensively by Pálsson et al. [2002], Björnsson et al. [2003], Fischer et al. [2003] and Adalgeirsdottir et al. [2005].

Short diary of events

Since 1993 surface velocities and mass balance have been measured regularly. During the years prior to the surge and even prior to any visible signs of an imminent surge, <1995, measured surface velocities were about 25-70% of the velocities necessary to maintain a balance between accumulation and ablation [Adalgeirsdottir et al., 2005], which is typical behavior of surge-type glaciers in their quiescent period. Consequently, a build-up of snow in the reservoir area and heavy ice losses in the ablation area took place. The glacier rose about 10 m in the accumulation area but lowered 60 –70 m in the receiving area.

During 1996 and 1997 unusually crevassed areas were observed and increased velocities were measured, indicating the onset of a surge event. In spring 1998 no visible signs of surging were detected, but during the summer velocities increased rapidly at different measurement sites. This was followed by increasingly crevassed areas visible during the fall. The velocities exceeded 40 m per day at the surge wave front in 1999 [Adalgeirsdottir et al., 2005]. The maximum LOS motion (found with the same SAR data as is used in this thesis) is reached near the equilibrium line at about 1300 m a.s.l. [Fischer et al., 2003]. The surging was nearly finished in January 2000 according to Adalgeirsdottir et al..

The surging led to a 70 m drop in elevation in the reservoir area and 100 m increase in the receiving area, see Figure 6.1. The glacier terminus advanced 1.9 km in the Eastern part and about 1.5 km in the more Western part. The total area affected by the surge event was 800 km^2. The glacier suffered a mass loss of 13 km^3 in the reservoir area but gained 9.8 km^3 in the ablation zone over a period of two years (1998-2000). Uncertainty in the airborne radar survey data of 2 m causes an uncertainty in the volume estimates of 1.6 km^3. From these mass loss/gain figures can be concluded that ice volume transported to the ablation area is only about three-quarters of the mass lost in the accumulation area. The difference is mainly due to enhanced melting rates because of a larger surface area caused by the many crevasses. Increased turbulent fluxes above the surface and increased frictional melting at the bed during the surge are other reasons that explain the partial mass transport.

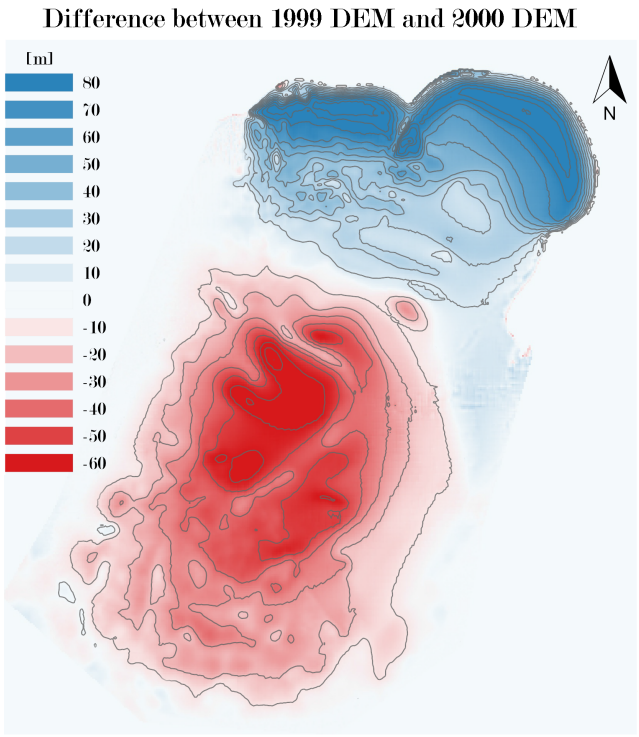

FIGURE 6.1: By subtracting the two available DEM's, (see Subsection 2.2.2 and [Pálsson et al., 2002]) from 1999 and 2000 from each other, the drop in elevation in the accumulation area and the increase in the ablation area are visible. The contourlines denote 10 m elevation differences.

A more detailed diary of events is presented in a report about the surge of Dyngjujökull by Pálsson et al. [2002].

6.3 Results and interpretation of the derivation of 3D flow fields

Retrieving information about the vertical component of the ice motion during the surge is of main interest when deriving 3D flow fields. Vertical anomalies, or bulls-eye patterns, can point to subglacial accumulation or depletion of water, which in turn can relate to the subglacial hydrologic system. The research presented in this section can be seen as solving an observational part of the puzzle that leads to confirmation of the mechanism that drives glacial surges. To achieve this goal, the glaciology method, MRF optimized with Simulated Annealing, is tested (see Chapter 5). Based on a variety of tests, a reliable extension of the method is created by the implementation of the possibility to take along-track shift estimates in the process of deriving 3D flow fields. For more information on the background of the model see Section 5.1.

In the testing procedures the concept of MAI is used. Since it is shown in Section 3.1 that MAI and SD are equal, the glaciology method extended with MAI functionality is converted to the use of SD as along-track input option. This makes the code dependent on pairwise parameters, which are output by the script used to get azimuth SD interferograms (`splitaz.m`). These variables are the azimuth CBF bandwidth B_a, the pixel spacing and the Doppler centroid difference between backward-, or upper-, and forward-, or lower interferogram:

$\Delta f_{Dc} = f_c^A - f_c^B$. In this way, every individual interferometric pair can be converted to offsets in meters using the unique parameters:

		B_a [Hz]	Δf_{Dc} [Hz]
Pair 1:	6/7 January 1999	1211.91	410.69
Pair 2:	10/11 February 1999	1229.24	422.55
Pair 3:	27/28 February 1999	1199.99	400.78
Pair 4:	26/27 January 2000	1283.79	462.62

TABLE 6.1: Parameters given for each data pair, to convert from SD phase to offsets in meters.

In Subsection 6.3.1 the input data for the derivation of 3D flow fields with the glaciology method will be discussed. Subsection 6.3.2 will give an overview of the results of the different runs with the glaciology method. Finally, in Subsection 6.3.3 interpretations of the outcomes will provide a linkage with the previous subsections to come to conclusions and potential future work.

6.3.1 Discussion on input data and settings to run the glaciology method

To be able to use the MRF method, optimized with Simulated Annealing, several input files have to generated. The introduction of the data and the subject of the settings of the algorithm to derive comparable 3D flow fields, is dealt with in this subsection. The input data for the glaciology method consists of:

- unwrapped LOS phase
- azimuth SD phase (corrected for ionospheric distortions)
- a bedrock DEM (subglacial topography [Björnsson, 2009])
- a surface DEM, either from 1999 or 2000 dependent on the acquisition date of the interferometric pair
- incidence angles for the scene of interest
- azimuth angle for the scene of interest
- an ice thickness grid

Both the incidence- and azimuth angles are different for each data pair and derived from the original interferometric data and known orbits. The thickness grid is produced by subtracting the bedrock DEM from the surface DEM and is visible in Figure 6.2. It shows that the thickness of the ice is very distinct for different areas of the Vatnajökull ice cap. The Northern side (where Dyngjujökull

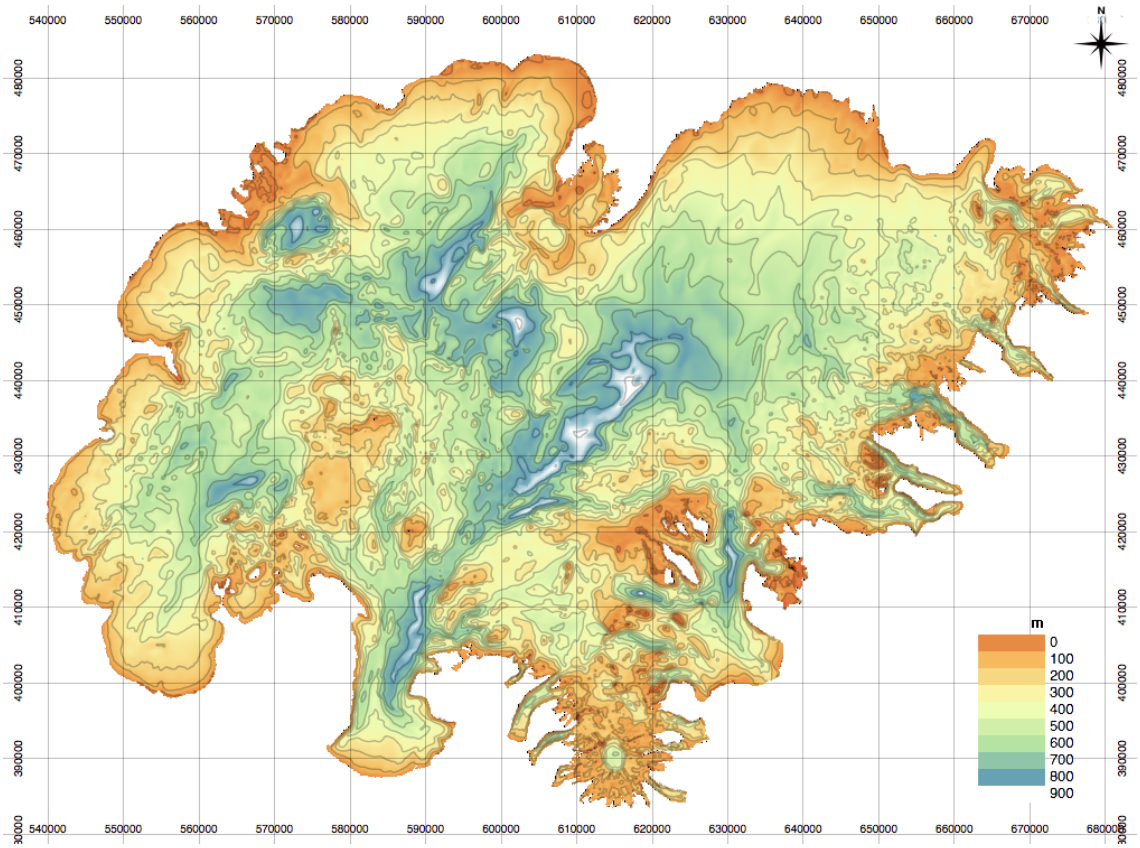

FIGURE 6.2: Thickness grid of Vatnajökull ice cap in 1999, as an example of real input data for the glaciology method. The thickness is obtained by subtracting the bedrock DEM [Björnsson, 2009] from the surface DEM. Isolines are shown every 100 m.

is located) has a rather smooth profile, whereas ice thicknesses up to a kilometer can be found in the middle part of Vatnajökull. Over a year (1999-2000), the surface of the ice cap changed significantly due to the surge, as is visualized for a cutout of Dyngjujökull in Figure 6.1. For this reason two input data sets are used. The first one is based on the situation in 1999 (using a surface DEM from 1999), the other one is based on the state of the ice cap in 2000 (using a surface DEM from 2000) to enable the processing of the 26/27 January 2000 data. For more information on the surface DEMs, see Section 2.2.

The LOS interferograms are derived by E. Magnússon (HI) for all ascending scenes (see Section 2.2 and Appendix A). Improvements in the processing of raw data enabled the possibility of using the descending pair of 27/28 January 1999. This interferogram is unwrapped and shown in Figure 6.3 (A). Unwrapping is done by means of SNAPHU [Chen and Zebker, 2002]. A phase bowl is apparent in the unwrapped scene, which is possibly due to atmospheric (ionosphere, troposphere) errors. Any phase distortions caused by it are not removed since the glacier is located in a region where the distortion is assumed to be stable. The rewrapped and geocoded (to ISN93 Lambert coordinates) interferogram is shown in Figure 6.3 (B).

During acquisition of the descending scene, the flying direction of the satellite

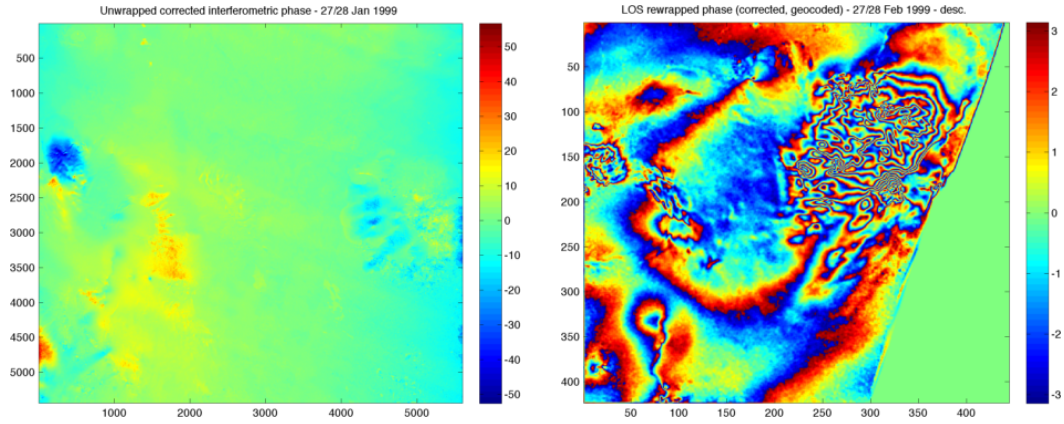

(A) (B)

FIGURE 6.3: (A): Unwrapped interferogram of the 27/28 February 1999 data pair in radar coordinates. Unwrapping is done by means of SNAPHU, [Chen and Zebker, 2002]. The glacier is located around the blue area on the left side of the image. From left to right a bowl formed ramp is visible. This distortion is not removed, because only a cutout of the glacier is used in further processing. In the cutout the ramp is assumed to be constant. (B): geocoded (to ISN93 Lambert coordinates) cutout of (A).

was parallel (but opposite) to the direction of the presumed flow. The application of SD therefore constraints a major part of the horizontal flow direction. This means that the LOS phase only contains a small portion of the total phase for East-West motion. Consequently, the main component visible in the rewrapped LOS phase (B) is caused by vertical motion.

It is important to note that if the glacial velocities are too large, the fringe density in the LOS phase will be too high or completely decorrelated. Since this leads to unwrapping issues, the affected pixels are masked and will not be used in further derivations of the 3D flow fields. As a result, the outcomes of processing with the glaciology method will contain areas where no data is present (see for example Figure 6.7).

The glaciology method has weight parameters incorporated that can be used to tweak the final outcomes to converge to a optimal solution. One of the 'switches' is the option to in-, or exclude the mass continuity from the set of equations. For tranquil moving glaciers monitored by InSAR having a short temporal baseline, the assumption can be made that the mass continuity equation holds [personal communication with E. Magnússon]. One can argue if this is still true when applying it to glaciers in surge state when high velocities are present. Residual errors in the derived flow fields will indicate whether or not the mass continuity equation will hold when running the glaciology method with and without it.

Next to the weight factor of the mass continuity equation, w_{mc}, other parameters are available for tweaking the algorithm. As introduced in Chapter 5, these are the smoothness coefficient w_{dV} and directionality factor w_{dir}. Based on the outcomes of the testing procedures and personal communication with E. Magnússon, the processing parameters are chosen to be $w_{mc} = 1$, $w_{dir} = 0.05$, $w_{dV} = 0.1$

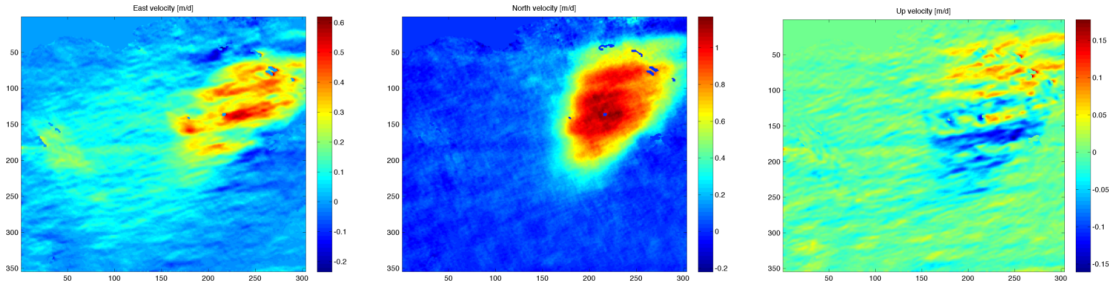

(A) East (B) North (C) Up

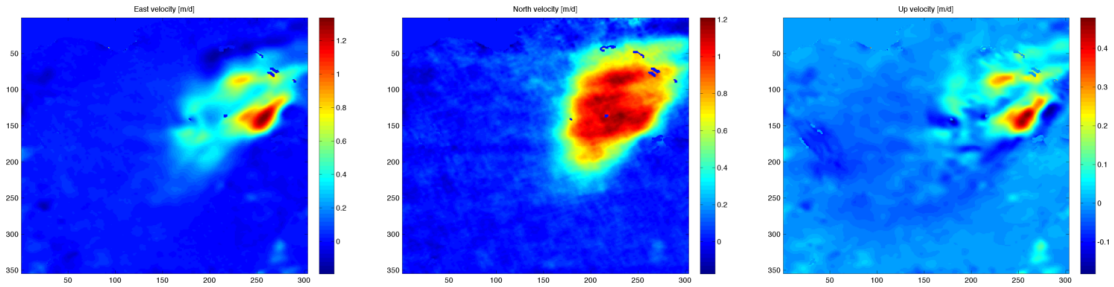

(D) East, $w_{mc} = 0$ (E) North, $w_{mc} = 0$ (F) Up, $w_{mc} = 0$

FIGURE 6.4: An overview of derived 3D velocity components, both with the mass continuity equation included, (A), (B) and (C), and excluded, (D), (E) and (F). Based upon data of 6/7 January 1999. The North-component is in both cases well constrained by the input of the SD phase. The East (D) and Up (F) velocties are wrong when the mass continuity is not used. This is due to an incorrectly assumed horizontal flow direction in the regions of high motion. (A) to (C) are derived using: $w_{mc} = 1$, $w_{dir} = 0.05$ and $w_{dV} = 0.1$ whereas (D) to (F) are derived using $w_{mc} = 0$, $w_{dir} = 0.5$ and $w_{dV} = 0.1$.

and $w_{mc} = 0$, $w_{dir} = 0.5$, $w_{dV} = 0.1$. Thus a minimum of two runs with the glaciology method is carried out for each pair. The quality of the 10/11 February scene SD outcomes is such that the result is not usable in the derivation of 3D flow fields. To compensate for this missing constraint, a high flow directionality weight factor is used in combination with the mass continuity equation: $w_{mc} = 1$, $w_{dir} = 0.5$ and $w_{dV} = 0.1$.

The iterations start with flow field that is equal to zero. The algorithm used two consecutive iterations, with different settings for the Simulated Annealing, to converge to a solution. The first iteration takes the zero-velocities flow field and uses a high energy state to find an initial solution. The initial solution is then used as input flow field for the second iteration, where the convergence parameters are tweaked to achieve a finer, thus more optimal, final solution.

6.3.2 3D flow fields and corresponding quality figures

Using the settings as noted down in Subsection 6.3.1 the glaciology method is ran. The pair with the least ionospheric distortions, 6/7 January 1999, is taken as

an example to discuss the derived 3D flow fields. The outcomes of the remaining pairs will be dealt with later in this subsection.

3D flow fields and corresponding quality figures of 6/7 January 1999
In Figure 6.4 (A), (B) and (C) the results of the glaciology processing, with the mass continuity equation enabled, are shown. In the East- (A) and Up- (C) components distortions are clearly visible. These patches can be explained by too heavy or too light settings of the 2D directional interpolation filter that is applied to remove the ionospheric noise. In the corrected SD data the streaks are not visible by eye anymore. However, since there is interaction between the East-, North-, and Up-component when running the glaciology method, some residual distortions are leaking from the azimuthal input data to the East,- and Up-component. However, despite the irregularities in the flow caused by the removal or remainder of the ionosphere, Figure 6.4 (C) shows correctly what is expected. Positive Up-velocities, corresponding to likely compressive strain, can be seen in the lower (or receiving) part of the glacier, while negative values, corresponding to alleged tensile strain, are found in the upper part of the glacier.

Figure 6.4 (D) to (F) show the outcomes without the mass continuity switched on. The results appear smooth, but looks can be deceiving. There are two parts of the glacier where velocities are peaking, as is visible in (D) and (F). The flow speeds of the Up-component in these regions are too high with respect to the corresponding East-West motion, indicating erroneous behavior due to the absence of the mass continuity constraint. The anomalies in the regions of high motion are present due to an incorrectly assumed horizontal flow direction, (ψ). This constraint is estimated using the gradient of a smoothed surface DEM. In other words, the flow of the glacier is assumed to follow the slope of the smoothed surface DEM, which is apparently not true in all cases. For this reason, the 3D flow fields of the other data pairs (presented in Figure 6.7) are derived with the mass continuity equation included.

In Figure 6.5, the Root Mean Square (RMS) errors corresponding to the different energy equations discussed in Section 5.1 are shown for the 3D flow fields of the 6/7 January 1999 pair (Figure 6.4 (A) to (C)). These figures give an indication of the quality of the flow field derivations. When there is a lot of melt or precipitation the mass continuity equation will show wrong results, resulting in high RMS errors for U_c (A). Melting is not an issue because the images are all acquired in wintertime. In case of snow or rain events the interferometric coherence will be affected. In the derivation of the motion fields low coherent pixels will be masked out, so precipitation will not influence the quality of the derived velocity estimates.

By ruling out weather influences, large residuals can be introduced due to three main causes. The first error source that has a severe effect on the accuracies of the results, and most important in pinpointing areas where water accumulation or depletion is present, is whether or not the mass continuity equation will hold. In Figure 6.5 (A) the residuals show no clear anomalies. The mass continuity equation can thus explain the observed flow completely. The second major influence that can inhibit the derivation of an accurate solution is if there are

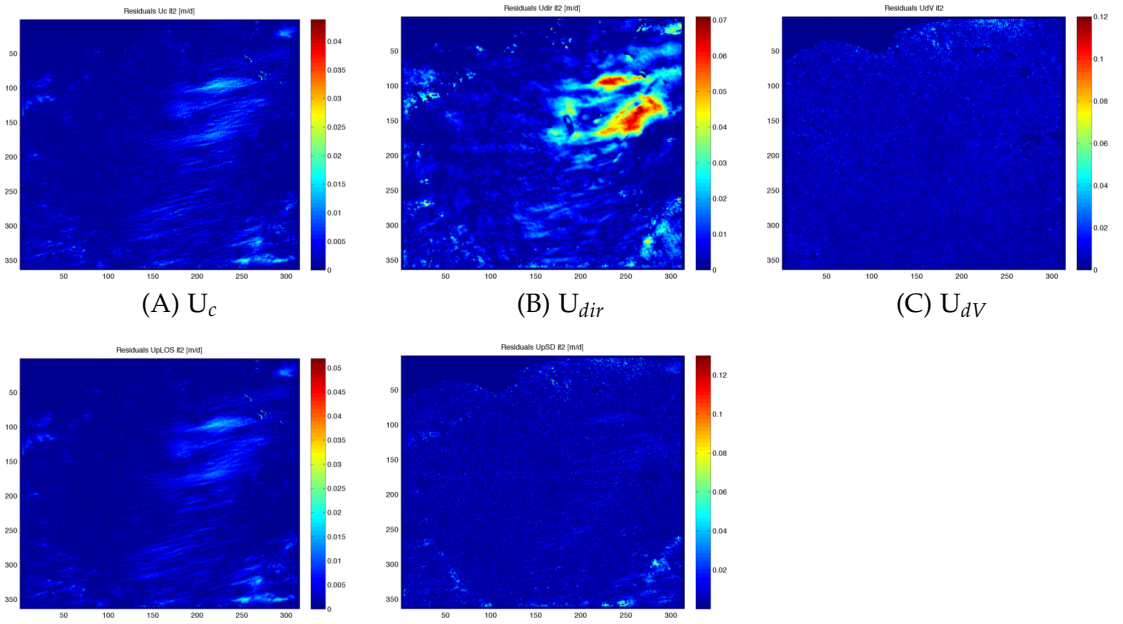

(A) U_c (B) U_{dir} (C) U_{dV}

(D) U_{LOS} (E) U_{azi}

FIGURE 6.5: RMS errors [m d^{-1}] belonging to the 3D velocities of the 6/7 January 1999 pair and displayed in Figure 6.4 (A) to (C), are shown here. Each image corresponds to a different energy equation, which are introduced in Section 5.1. High residuals in (B), corresponding to the directionallity constraint, are due to an incorrect assumption of the horizontal flow direction.

errors in the input phase data. Most input errors are likely to be caused by the SD input, particularly by the aforementioned influence of the ionospheric filtering. An example of this effect on the residuals is visible in Figure 6.5 (A) and (D) where directional oddities can be seen. The third, but less prominent option is the possibility of errors in the bedrock DEM of which the error propagates through to the 3D flow fields.

In Figure 6.5 (B) a clear pattern of residuals is visible, which is similar to the anomalies shown in Figure 6.4 (D) and (F). This confirms that the mass continuity equation has to be included in the derivation of the 3D flow fields using this data. By plotting the horizontal flow magnitude and direction in vectors, as is done in Figure 6.6, this is visualized clearly.

As can be seen in Figure 6.6, the glacier moves as a whole, corresponding to the hypothesis of distributed water pockets introduced in Section 6.1 as a subglacial hydrologic mechanism. The white vectors indicate the assumed horizontal flow direction (no magnitude) based on the filtered surface DEM. The black arrows denote the derived direction and magnitude of the horizontal flow. If the motion is smaller than 5 cm per day the arrow is not shown. The background is a map showing the derived horizontal flow magnitude for the whole scene. The anomalies caused by the assumed flow direction (w_{dir}) are resolved by applying the mass continuity equation. The source of the anomalies can be seen from the difference in direction between the white and black arrows in the affected area.

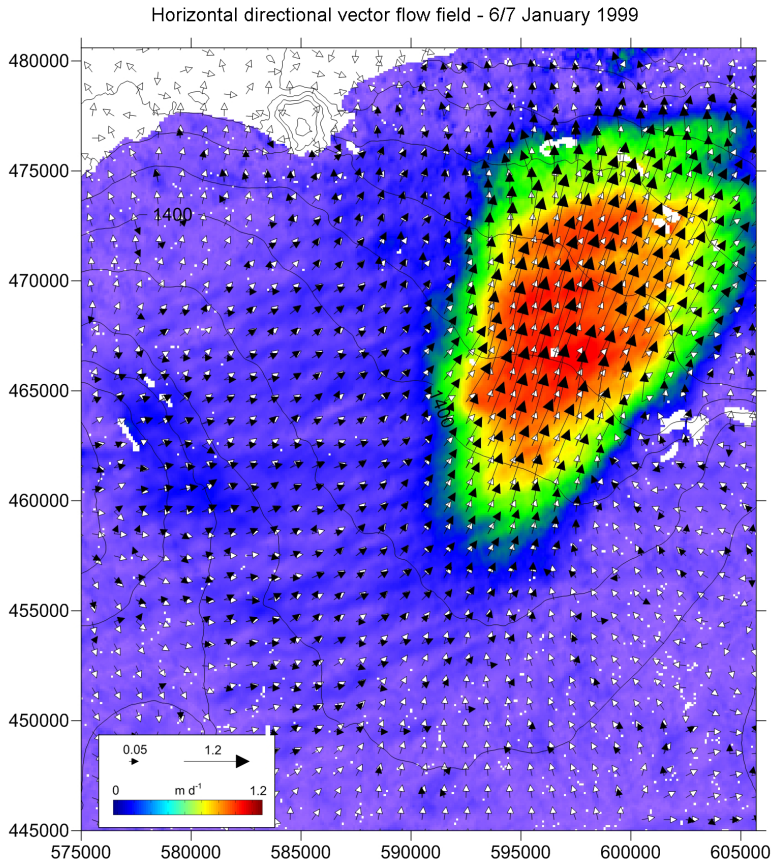

FIGURE 6.6: This plot shows the horizontal flow direction and magnitude. The black arrows indicate the direction and the magnitude of the velocities. The white arrows are indicative for the flow direction when it is derived from the slope of the glacier. The maximum horizontal motion is $1.2\,\mathrm{m\,d^{-1}}$. The anomalies present in Figure 6.4 (A) and (C), and Figure 6.5 (B), are also visible here. The black- and white arrows deviate in direction on the Eastern side of the glacier.

3D flow fields derived for all remaining data pairs

The results for the remainder of the data pairs are shown in Figure 6.7. For 10/11 February 1999 the flow components are presented in (A), (B) and (C). Approximately the same area as in January 1999 is affected. This pair is not processed with SD results included due to the bad quality of the derived SD interferogram. The ionospheric distortions where so heavy that they completely masked the movement of the glacier. To compensate for this, the pair is processed with the following parameters: $w_{MC} = 1$, $w_{dir} = 0.5$ and $w_{dV} = 0.1$. Since the directional flow- and the mass continuity constraint both give a measure for the horizontal flow, they can influence each other. Because of these mutual interferences this 3D motion solution is not to be trusted. Adding to this, the vertical flow, visible in (C), is almost completely downwards, which is not to be expected given the solution of January 1999.

For the descending scene of 27/28 February 1999 , the full solution is given in Figure 6.7 (D), (E) and (F). The similarity with the outputs of the January 1999

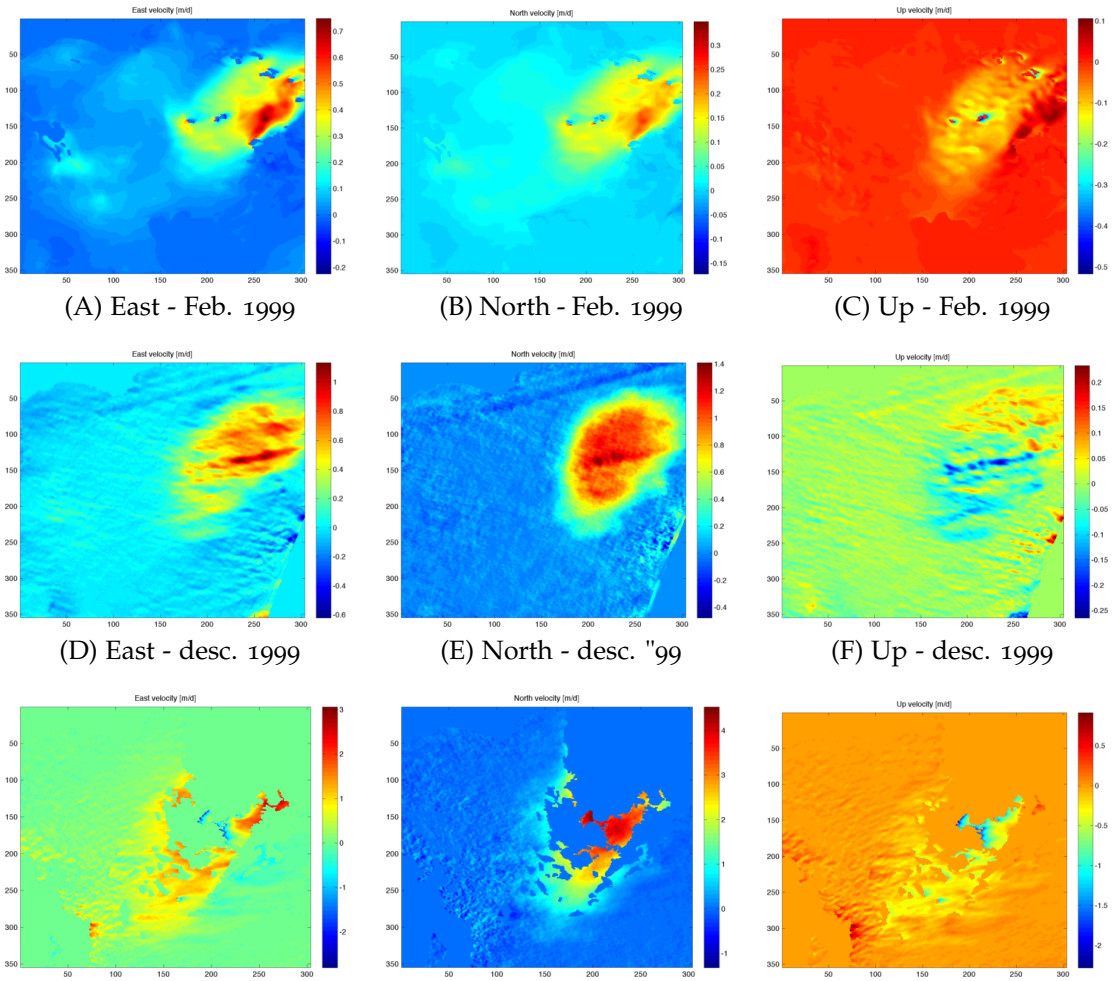

(A) East - Feb. 1999 (B) North - Feb. 1999 (C) Up - Feb. 1999

(D) East - desc. 1999 (E) North - desc. "99 (F) Up - desc. 1999

(G) East - Jan. 2000 (H) North - Jan. 2000 (I) Up - Jan. 2000

FIGURE 6.7: An overview of the 3D flow components, North, East and Up, for all remaining data pairs. (A), (B) and (C). show results for 10/11 February 1999. This pair is not processed with an extra constraint on the North-South motion because of a bad quality SD interferogram. To compensate for this, the pair is processed with the following parameters: $w_{MC} = 1$, $w_{dir} = 0.5$ and $w_{dV} = 0.1$. (D), (E) and (F) show results for the descending scene of 27/28 February 1999. (G), (H) and (I) show outcomes for 26/27 January 2000. Many pixels are masked because of unwrapping difficulties in the LOS interferogram. Just as 6/7 January 1999, see Figure 6.4, the two latter pairs are processed with $w_{MC} = 1$, $w_{dir} = 0.05$ and $w_{dV} = 0.1$.

example is obvious. First, the North-South motion is well constrained by the SD input. Second, streaks because of the filtering algorithm are clearly present in the East Figure 6.7 (D) and Up (F)-components. The Up-component shows downward motion in the upper part and upward motion in the receiving area of the glacier, which is also in accordance with the results of January 1999. The two high value spots in the center of the glacier, visible in the East component (D), are thought to be magnified due to remaining ionospheric influences.

The output for 26/27 January 2000 is visible in Figure 6.7 (G), (H) and (I). As mentioned in Subsection 6.3.1, many pixels are masked because of very large motions (over $10\,\mathrm{m\,d^{-1}}$) in this fully developed surge. The pixels that are available already show more than $3\,\mathrm{m\,d^{-1}}$ of horizontal flow. One particular region in the middle of the glacier, where dark pixels are visible near the edges, shows odd behavior. Sudden westward motion is suspicious, knowing that the other pairs show a full flow field oriented East. However, it is difficult to assess the (in)correctness of unwrapping in this area due to the small amount of useful pixels around that area. A similar issue can be seen in the Up-velocity. Streaking due to the filtering algorithm is less clear, but still visible in the South-East part of the image. Compared to the extent of the surge in 1999, it is obvious that the area affected by the surge grew significantly up-slope towards the South-West.

Quality figures of all remaining data pairs

The quality of the derived figures for 10/11 February 1999 are shown in Figure 6.8. These residuals confirm the wrong results presented in Figure 6.7. By adding the RMS errors in the mass continuity-, the horizontal flow- and the LOS phase components together, residuals over $0.3\,\mathrm{m\,d^{-1}}$ on a maximum flow of $1.5\,\mathrm{m\,d^{-1}}$ are found. One solution to get more accurate results would be to take the derived horizontal flow field from the January 1999 scene as a constraint, instead of the one derived from a smoothed surface DEM.

The quality figures of the descending 27/28 February 1999 scene, see Figure 6.9, demonstrate behavior similar to the January 1999 pair, including some remains of ionospheric streaks or filtering in the U_c and U_{LOS} images. All the residual show small values, in the order of 0.02 - $0.05\,\mathrm{m\,d^{-1}}$. The directionality RMS image shows similar problems as the corresponding image in Figure 6.5. Thus, there are areas where the assumed horizontal flow direction does not hold. Since all data pairs, except the February 1999 scene, are processed with a low weight on the horizontal directionality of the flow, this behavior is not visible in the derived 3D velocity components.

For the results of 26/27 January 2000, visible in Figure 6.10, applies the same as for the January 1999 and the descending pairs. The directional flow shows motion errors over $0.55\,\mathrm{m\,d^{-1}}$, which are also visible in U_c and U_{LOS}. This happens especially in the area in the middle of the glacier, where it is surrounded by masked pixels. Due to the amount of excluded pixels, the outcomes are not very useful yet. As mentioned before, offset tracking results in the LOS direction may provide more useful areas to work with, albeit at a reduced resolution.

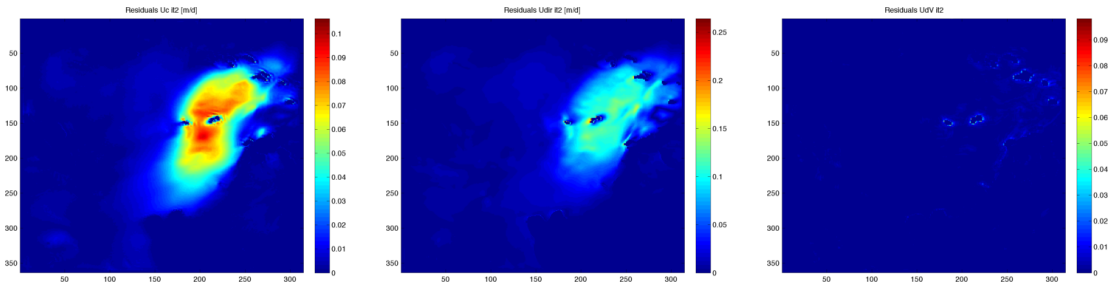

(A) U_c (B) U_{dir} (C) U_{dV}

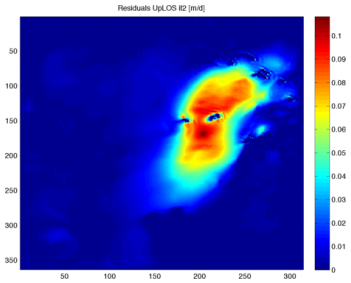

(D) U_{LOS}

FIGURE 6.8: RMS errors [$m\,d^{-1}$] belonging to the 3D velocities of the 10/11 February 1999 pair and displayed in Figure 6.7 (A) to (C) are shown here. Each image corresponds to a different energy equation, which are introduced in Section 5.1. The high residuals in U_c, U_{dir} and U_{LOS} are indicative of wrong results presented in Figure 6.7.

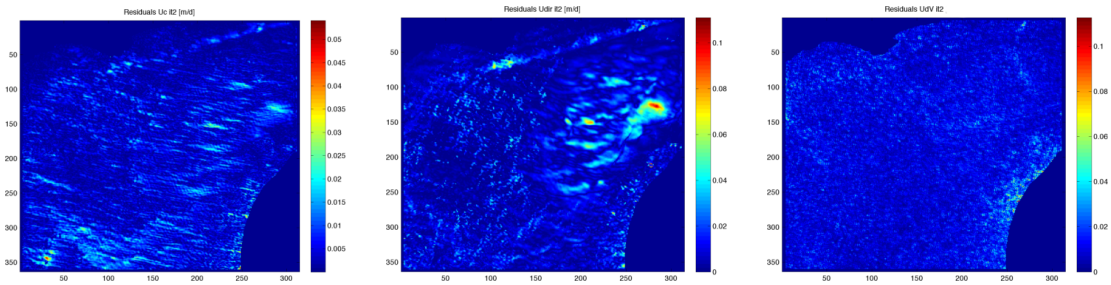

(A) U_c (B) U_{dir} (C) U_{dV}

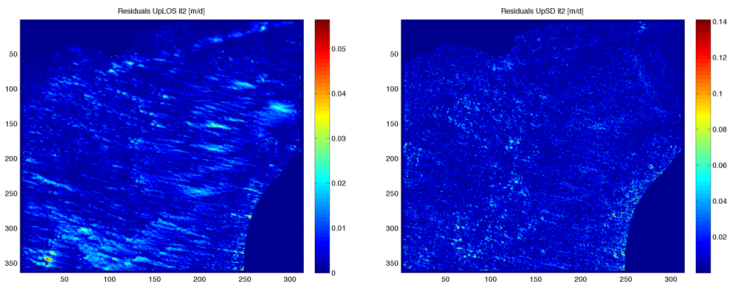

(D) U_{LOS} (E) U_{azi}

FIGURE 6.9: RMS errors [$m\,d^{-1}$] belonging to the 3D velocities of the 27/28 February 1999 pair and displayed in Figure 6.7 (D) to (F) are shown here. Each image corresponds to a different energy equation, which are introduced in Section 5.1. The residuals show similar behavior to the January 1999 pair.

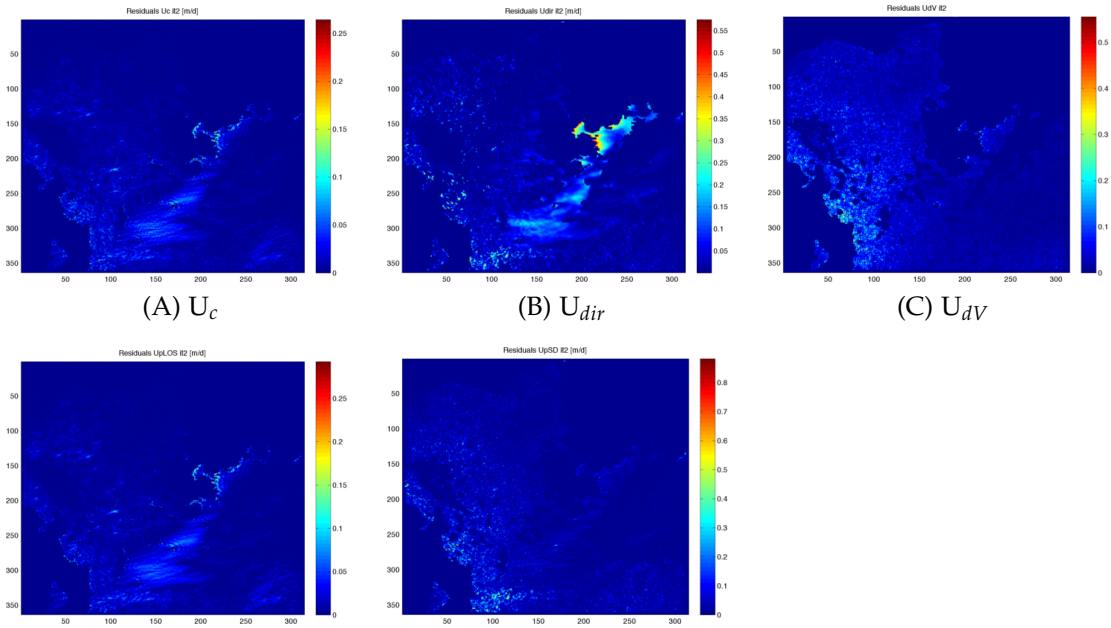

(A) U_c (B) U_{dir} (C) U_{dV}

(D) U_{LOS} (E) U_{azi}

FIGURE 6.10: RMS errors [m d^{-1}] belonging to the 3D velocities of the 26/27 January 2000 pair and displayed in Figure 6.7 (G) to (I) are shown here. Each image corresponds to a different energy equation, which are introduced in Section 5.1. The residuals show similar behavior to the January 1999 and the descending pairs, altough the velocities are much higher and the extend of the area affected by the surge is much larger.

6.3.3 Glaciologic interpretation and conclusions

The extension of the glaciology method with the ability to use along track SD phase has proven to work with real input data. No clear bulls eye patterns or other anomalies are visible in the residuals, indicating that **for all pairs the observed flow can be explained by the mass continuity equation**. It does not imply that there is no vertical motion related to the water pockets in the subglacial hydrology. **The vertical motion caused by a system of linked cavities is just not large enough to be detected with this method**.

The movement of the glacier as a whole indicates a process similar to a system of linked cavities, but does not prove or disprove the theory as introduced by Kamb [1987]. The sliding of the glacier on its bed is facilitated due to the distribution of water across the entire bed, causing the glacier to move as a 'block', as can be seen in Figure 6.6 and Figure 6.11. The rates approximately correspond to the the total gain or loss estimated over the whole surge [Pálsson et al., 2002], if the derived Up-velocities would be extrapolated to the duration of the event. In the former figure it is clear why **the mass continuity equation is needed during the derivation of 3D flow fields** when the current four interferometric pairs are used as input data. The anomalies caused by the assumed flow direction (w_{dir}) are resolved by applying the mass continuity equation. This is indicated by the difference of the assumed horizontal flow direction (white arrows), based on the

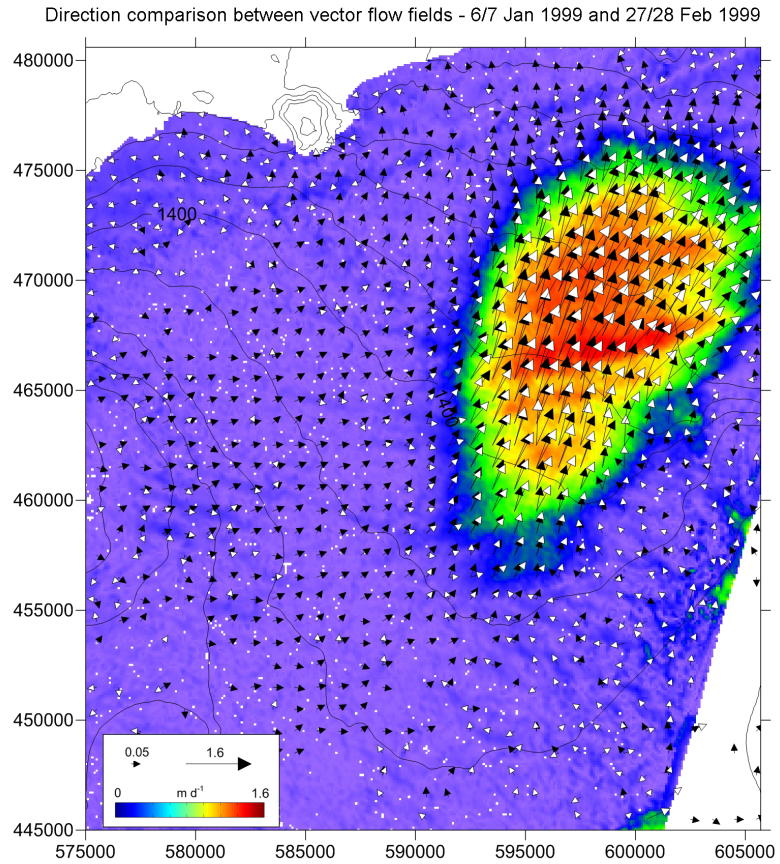

FIGURE 6.11: A comparison of vector fields showing horizontal flow magnitude and direction between the 6/7 January 1999 and the descending 27/28 February 1999 data pairs. The black arrows show the horizontal flow field of January 1999, whereas the white arrows present the descending 1999 horizontal velocity. The background is the full flow field of the latter. Distortions due to remaning ionospheric distortions are visible in the area with peak velocities of $1.6\,\mathrm{m\,d^{-1}}$. The flow vectors also deviate from the direction indicated by the January 1999 arrows, where only minor ionospheric noise is present.

local slope of the glacier, and the derived horizontal flow direction (black arrows) in Figure 6.6. Thus, **a valid assumption for the horizontal flow direction is key to solve for the Up-velocity accurately**.

The up- and downward motion of the glacier in the Up-components of the January 1999 and the descending 1999 scenes, look as expected. Since the pairs are acquired within a time frame of two months, some uniformity between the flow fields is likely. Figure 6.11 shows a comparison of horizontal flow magnitude and direction in vectors on a background of the full horizontal motion field of the descending scene. **The two flow fields are consistent with each other**. The area affected by the surge has not been changed significantly. Deviations in the direction and overestimations of the velocities in the descending scene are due to residuals of ionospheric distortions, which are still contaminating the signal after filtering.

The anomalies present in the Up- and East velocity figures are caused by the 2D directional FFT interpolation filtering algorithm. The error propagates from the SD input, where the remaining distortions are hardly visible by eye, through to the final outcomes. **The strong presence of the directional distortions indicates that the azimuth input component has a prominent role in the derivation of the 3D flow fields**. One way to work the around this, is by rerunning the glaciology method with a weight coefficient on the energy equation related to the SD phase. In this way, the SD influence is less present in the whole optimization process and consequently the use of the LOS phase is favored more. Another way to diminish the effect is by changing the interpolation filter to find the settings that cause the least distortions in the eventual 3D flow fields.

The current results look promising, but improvements need to be made on, inter alia, the filtering of the ionosphere, the weighting of the azimuth component and the comparison with the parallel flow assumption. Potential future work will discussed in Chapter 8.

* * *

Part IV

conclusions and recommendations

Chapter 7

Key findings and significance

During 1997-2000 Dyngjujökull, one of the major outlet glaciers of the main Icelandic ice cap Vatnajökull, surged. This event was captured by ERS 1 and 2 satellites flying in tandem mode, enabling the use of InSAR to monitor the motion of the glacier. Since a major limitation of InSAR is its sensitivity to deformation in only one dimension, the research presented in this M.Sc. thesis searched the most accurate method of extracting azimuthal deformation using InSAR. Starting from a theoretical framework, the available methods are explored and corresponding measurement uncertainty formulas are derived. Currently available software enables the possibility to underpin the theoretical findings by performing different tests to compare two methods that are widely used in the InSAR community. Results show the presence of azimuthal shifts corresponding to TEC variations in the Earth's ionosphere, which partly distort the along-track deformation. To solve this, the nature of this signal is studied and a filtering method is designed. Consequently, the corrected azimuth interferograms are used jointly with LOS interferometric data in a Markov Random Field minimum energy method, optimized by Simulated Annealing to derive 3D flow fields of the Dyngjujökull glacier in surge. This glaciology method is tested for its response behavior using synthetic data. The testing involved mainly noise propagation and assessing the influence of different weighting factors in the optimization of the 3D flow outcomes. Knowing the limitations of the glaciology method, 3D flow fields are derived with real input data accordingly. The results show both horizontal- and vertical velocities corresponding to observational data. Finally, the presence of a system of linked cavities is partly confirmed as the subglacial hydrologic mechanism of surging glaciers.

The key findings that are obtained, the issues that are resolved, and other interesting remarks will be presented here. Aligned with the project setup, these conclusions are presented classified according to the three parts that make up this research project: *1. Theoretical similarity assessment* of azimuthal deformation extraction methods, *2. Improvements on the extraction of along-track deformation* and applicational similarity assessment, *3. Simulation and derivation of 3D velocity fields during glacial surges*.

PART I - Theoretical similarity assessment

Within this theoretical framework, the methods that are investigated on their underlying assumptions, drawbacks and characteristics, include Spectral Diversity (SD), Multiple Aperture InSAR (MAI), Coherent Cross Correlation (CCC) and Incoherent Cross Correlation (speckle tracking) (ICC). In azimuth, the Doppler bandwidth and corresponding central frequency play an important role in the extraction of along-track shift estimates for the former two spectral methods. The algorithms behind SD and MAI are dependent of the properties of these parameters. An assessment is made on the similarity between SD and MAI, but also between SD and CCC.

1. MAI is proven to be a particular instance of SD in azimuth with a band split equal to half of the full azimuth bandwidth.
2. SD and CCC are comparable in terms of accuracies. However, a detailed comparison of the accuracy formulas show that they are not completely equal. CCC reaches the Cramer-Rao bound, whereas SD approaches this boundary by a 6% offset. This implies, if properly implemented, that both methods will yield the same results.
3. The derived accuracy formulas are only applicable to compare methods, not to apply to real data. The derivations assume circular white Gaussian processes, while real data never meets this criterion. The presence of features and apparent residual phases due to limitations in the implementation of the different methods, are sources of error when comparing real data to theoretical assumptions.

PART II - Improvements on the extraction of along-track deformation

By conducting a comparison between applicational results of SD and ICC, the theoretical findings of Part I are supported. Besides that, settings of the SD and ICC method are found to allow for proper comparison of the two. The alleged similarity of SD and CCC is not tested due to residual phases (flat-Earth and topographic phases) that need to be removed from both master and slave separately, before applying the cross correlation procedure. An interesting unexpected finding during processing led to implementation of a interpolation algorithm to filter out positional shift errors due to ionospheric electronic density variations along the synthetic aperture.

4. Based on application of SD and ICC to four different InSAR pairs, it can be concluded that the methods are comparable in outcomes. SD shows more accurate results with a minimal standard deviation comparison factor of 1.1. This performance difference is expected because ICC uses only the

magnitude part of the complex signal and thereby utilizing only a portion of the available information. However, the theoretical variance comparison factor of 1.8 is not reached. The most prominent explanation for this is the presence of image features in the data that bias the outcomes of pure speckle tracking. The execution of SD is much quicker than ICC, and the pixel density for SD is much higher since the original image size is maintained. SD offsets are thus calculated for all pixels, contrary to a low pixel density for ICC to avoid excessive computational times. However, in case of a deformation signal larger than modulo 2π ICC is advisable over SD because direct offsets are obtained and unwrapping of SD phases is avoided.

5. To compare the results of SD and ICC in a correct manner, the following settings need to be taken into consideration:

   - *SD*: split the common band filtered Doppler bandwidth $B_{a_{CBF}}$ with a sub band size of: $b = B_{a_{CBF}}/2$ after resampling of the slave onto the master to obtain misregistration phases
   - *SD*: the result is filtered by a moving average filter where N_L independent samples are being averaged (e.g. square window of 32 pixels)
   - *SD*: the azimuth SD phases are converted to offsets in meters by multiplication with the $B_{a_{CBF}}$ and the original pixelspacing

   - *ICC*: perform another fine coregistration with a window equal to the one used in SD after resampling of the slave onto the master to obtain misregistration in pixel offsets
   - *ICC*: conversion to offsets in meters using the same pixelspacing as taken in the conversion of SD phases to meter offsets

6. The 2D directional FFT interpolation filter has proven to be a useful method to remove ionospheric streaks when data is sparsely available, as can be shown both visually and from the improvement in quality. The methods utilizes a Butterworth low pass filter to separate low frequency signals from the SD interferogram. Limitations of the method are the difficulty to cope with bended streaks and large masked areas. No values can be given to these bounds since they are dependent on the settings of the filter. Boundary problems, like interpolating masked areas close to the image edge, are currently unresolved. To mask out low coherent and deforming areas a masking procedure is implemented. This Smart Pixel Selection uses a phase gradient filter within a local neighborhood and a coherence threshold to determine interpolation areas.

PART III - Simulation and derivation of 3D velocity fields during glacial surges

Using the filtered along-track and conventional InSAR results from Part II as input in a Markov Random Field (MRF) minimum energy method, optimized by

Simulated Annealing, 3D flow fields of the Dyngjujökull glacier in surge are obtained. In MRF an image is interpreted as a network of random variables, where the value of each pixel in an image is only dependent on its nearest neighbors. Simulation annealing relates to the heating and cooling of a system to derive a minimum energy level contained in that system. The results of tweaking the weighting functions in the energy equation, with and without noise added to the synthetic input data, leads to an 'optimal' configuration and more knowledge about the method performance. The outcomes are used to constrain the derivation of 3D velocity fields using real input data.

7. The incapability of the method to distinguish between the up- and range component when the motion is parallel to the LOS results in an misestimation of the outcomes. This only occurs when the mass continuity equation is not applied as constraint in the total energy equation. An angular mask equal to or larger than 10° from the LOS direction is found to sufficient to mask out the main error.

8. The residuals obtained by comparing the output data to the synthetic data, are smaller when the weighting of the smoothing function within the total energy equation, is set to small values. This factor behaves similarly irrespective of leaving the mass continuity equation in or out. A low value for the flow directionality constraint also results in smaller residuals. In case of applying the mass continuity equation, the value of w_{dir} has to be an order of magnitude smaller.

9. When noise is added to the synthetic input data, it can be concluded that a large smoothing weight coefficient results in smaller residuals. This is expected since smoothing is generally implemented to reduce the influence of noise in the outcomes. Additionally, a small weight coefficient for the flow directionality also results in less erroneous outcomes.

10. For all derived 3D flow fields the observed flow can be explained by the mass continuity equation. The vertical motion caused by a system of linked cavities is not large enough to be detected with this method. This does not mean that the alleged subglacial hydrologic system is not present. Movement of the glacier as a 'block' may be due to a process similar to a system of linked cavities as the distribution of water across the bed enhances basal sliding, but the 3D flow field results do not prove or disprove the presence of this particular linked cavities system.

11. The up- and downward motion of the glacier in the Up-components of the January 1999 and the descending 1999 scenes, look as expected. The rates correspond to the the total gain or loss estimated over the whole surge, if the derived Up-velocities would be extrapolated to the total duration of the event. The horizontal flow fields of both pairs are consistent with each other and with expected velocities based on field observations.

12. The mass continuity equation plays an essential role in refraining the Up-component in relation to the horizontal flow direction. The use of this

constraint or a valid assumption for the horizontal flow direction is key to accurately solve for the Up-velocity.

The derived 3D flow fields of Dungjujökull and their corresponding residuals show that the extension of the glaciology method with the ability to use along track SD phase works with real input data.

* * *

Chapter 8
Recommendations and future work

During the execution of this research project, the main focus has been on answering the main question as introduced in Chapter 1. Due to the variety of topics treated in this thesis, many extra questions or challenges emerged along the way. Every additional subject or 'nice to do' was assessed in terms of timing, relevance and importance. The following lists comprise all recommendations and/or potential future work ordered based on their importance to continue research on, and divided over three main themes.

PART I - Theoretical similarity assessment

To give a full overview of the theoretical framework, the influence of several adaptations to the algorithm on the performance of both the band split and cross correlation methods has to be investigated. These different implementation strategies are listed here:

- Find optimal settings for the split bandwidth method in terms of accuracy and resolution. *Theoretical derivations of split bandwidth when using different weighting schemes or bandwidth gaps* are part of this.
- *Investigate the theoretical influence of interdependency of neighboring pixels when applying cross correlation with different windows*. For example a cross-correlation operation of a master pixel patch with a moving average window vs. cross correlation of a master pixels patch with a similar slave window patch may have different statistical properties.
- An important addition to add is the theoretical foundation for feature tracking, and the influence of point scatterers in cross-correlation operations. In real data, bright features will generally be present in the images. By performing ICC some patches will be correlated on the apparent features instead of the speckle pattern.

PART II - Improvements on the extraction of along track deformation

Many questions are raised concerning the wide range of improvements that can be made on the extraction of azimuth offsets. The theme is therefore divided into

two lists of important enhancements of the current methods. These methods are related to improvements in the extraction of along-track offsets to create a better foundation to support the current conclusions of the similarity assessment, and related to the nature and removal of ionospheric effects in InSAR data.

1. Applied similarity assessment:

- *Implementation of CCC* in the DORIS processing software gives the opportunity to combine the advantages of SD and cross correlation procedures. This also yields the possibility of comparing SD and CCC both theoretically as well as applied to both simulated and real InSAR data. An assessment like that will give more insight in the alleged similarity between the available along-track deformation extraction methods.
- *Implementation of SD in range* will give the possibility to combine conventional interferometry with split-bandwidth interferometry. The splitting of the bandwidth can for example be used for better and quicker coregistration, albeit at the cost of reduced resolution.
- *Investigating the difference in azimuth SD interferogram formation between Bechor and Zebker [2006], Jung et al. [2009],* where the Doppler bandwidth is split on image formation from raw data, *and the implemented version in StaMPS*, where the SD interferogram is obtained after processing one whole interferometric pair until resampling, *can yield information on the most accurate and quick method of obtaining azimuthal offsets*.
- The effects of *different weighting functions applied the sub band filters* on the outcomes of the split band processing will give information about the way the SD algorithm can be optimized to keep as much bandwidth as possible to get a more accurate estimation of the misregistration offsets.
- *Process SD and ICC with different windowssizes (16, 64, 128 etc.) to obtain information about the statistical dependence of the two methods on the windowsize*. The difference in statistical interdependence of pixels within the window neighbourhood for the cross-correlation and moving average filtering procedures, is not well understood.
- By estimating the misregistration offsets (e.g. ionospheric distortions) and separating them from regions with deformation, the *coregistration parameters can be updated to get improvements in the LOS phase after re-resampling and subsequent interferogram formation*. By making the misregistration estimation iterative, possible residuals offsets can be obtained leading to e.g. a complete removal of ionospheric effects, or a more accurate determination of the azimuth displacements.

2. Potential future research on ionospheric effects in azimuth SD interferograms and possible improvements on the 2D directional Fourier Interpolation filter:

- In general research on ionopsheric effects in high latitude areas as is done by Wegmuller et al. [2006] and Meyer [2010] can benefit from the split band method. The implementation of SD in both range and azimuth can provide an easy way to obtain sub band images where two times the subband width is smaller than the entire Common Band Filtered (CBF) Doppler bandwidth. *Small subband images, $2b < B_{a_{CBF}}$, derived using adapted SD processing, can provide detailed information on the ionospheric content of the SAR scenes*.

- In this thesis, the 2D directional FFT interpolation filter is designed for and used on real data. To create a filter with different options for different applications, *the ionospheric filter has to be tested on simulated data with different lowpass filter designs*. Within this series of testing, the option to investigate the usability with e.g. bended streaks and edge effects can be explored as well.

- The recently launched ESA SWARM satellites can provide valuable information about the Earth's ionosphere and magnetosphere. *A joint use of SWARM and InSAR data can give interesting new insights in the appearance of ionospheric streaks in InSAR data.*

PART III - Simulation and derivation of 3D velocity fields during glacial surges

The glaciology method, MRF optimized with Simulated Annealing, is tested for its behavior when different weighting factors apply to different parts of the total energy equation. The tests have been performed with and without a fixed noise level. The method can be enhanced by taking the following recommendations into account:

- *The estimation of error propagation in the currently used method is of great importance to quantify the accuracy of the derived 3D flow fields*. For this, many more simulations with synthetic data and different noise levels (for example ranging from extreme cases like SNR $= 1$ to SNR $= 100$) have to be carried out. A theoretical foundation of the propagation of noise into the outcomes would be highly relevant.

- Currently, the method as implemented uses no initial velocity estimates (corresponding to $v_e = 0$, $v_n = 0$ and $v_u = 0$). To improve i.a. convergence speed and quality of derived flow fields, *initial velocity estimates have to be derived using e.g. weighted least squares*.

- Using the advantages of both SD and speckle tracking (because of the appearance of features in real data), *it would be interesting to investigate to what extent a combination will improve the accuracy of derived 3D flow fields*.

- To decrease the influence of erroneous patches in the East- and Up velocities of the derived 3D flow fields, *it is advisable to add a weight coefficient on the SD input phase*. This is particularly practical if the main orientation of the glacial flow is in the along-track direction and if the obtained data is contaminated by ionospheric streaks.

- A logical application of the current results would be to *use the well-known parallel flow assumption in the derivation of the 3D flow fields to assess the differences between outcomes derived with the mass continuity equation and parallel flow assumption*. This can be easily implemented by setting the flow divide in the mass continuity equation to zero. Consequently, only reasonable estimates for the horizontal velocity of surging glaciers can be obtained.

- To improve the quality of the 3D flow fields of the 10/11 February 1999 interferogram, *the derived horizontal flow field of 6/7 January 1999 can be used as horizontal flow direction constraint*, instead of the slope of a smoothed surface DEM.

- *The possibilities of using speckle tracking results in the LOS direction should be explored* to be able to use more data in the derivation of 3D flow fields for the 26/27 January 2000 pair. Currently, no solution is obtained for many areas on the glacier, since the large motions cause severe decorrelation of the signal using conventional InSAR.

* * *

Bibliography

G. Adalgeirsdottir, H. Björnsson, F. Pálsson, and E. Magnússon. Analyses of a surging outlet glacier of Vatnajokull ice cap, Iceland. *Annals of Glaciology*, 98:23–28, 2005.

S.N. Anfinsen, P. Doulgeris, and T. Eltoft. Estimation of the Equivalent Number of Looks in Polarimetric SAR Imagery. *IGARSS 2008 - 2008 IEEE International Geoscience and Remote Sensing Symposium*, pages 487–490, 2008.

R. Bamler. Interferometric stereo radargrammetry: absolute height determination from ERS-ENVISAT interferograms. In *IGARSS 2000*, volume 2, pages 742–745, 2000. ISBN 0-7803-6359-0.

R. Bamler and M. Eineder. Split Band Interferometry versus Absolute Ranging with Wideband SAR Systems. *IEEE Transactions on Geoscience and Remote Sensing*, pages 980–984, 2004.

R. Bamler and M. Eineder. Accuracy of Differential Shift Estimation by Correlation and Split-Bandwidth Interferometry for Wideband and Delta-k SAR Systems. *IEEE Geoscience and Remote Sensing Letters*, 2(2):151–155, 2005.

R. Bamler and P. Hartl. Synthetic aperture radar interferometry. *Inverse Problems*, 14 (4):R1–R54, 1998.

I. Baran, M.P. Stewart, B.M. Kampes, Z. Perski, and P. Lilly. A modification to the Goldstein radar interferogram filter. *IEEE Transactions on Geoscience and Remote Sensing*, 41(9):2114–2118, 2003.

N.B.D. Bechor. *Extending Interferometric Synthetic Aperture RADAR measurements from one to two dimensions*. PhD thesis, 2006.

N.B.D. Bechor and H.A. Zebker. Measuring two-dimensional movements using a single InSAR pair. *Geophysical Research Letters*, 33(16), 2006.

H. Björnsson. Hydrological characteristics of the drainage system beneath a surging glacier. *Nature*, 395:771–774, 1998.

H. Björnsson. *Jöklar á Íslandi*. Bókaútgáfan Opna, Reykjavík, 2009.

H. Björnsson and F. Pálsson. Icelandic glaciers. *Jökull*, (58):365–386, 2008.

H. Björnsson, F. Pálsson, O. Sigurdsson, and G.E. Flowers. Surges of glaciers in Iceland. *Annals of Glaciology*, 36:82–90, 2003.

R. Brcic, M. Eineder, R. Bamler, U. Steinbrecher, D. Schulze, R. Metzig, K. Papathanassiou, T. Nagler, F. Mueller, and M. Suess. Delta-K Wideband SAR Interferometry for DEM generation and persistent scatterers using Terrasar-X. In *Fringe 2009 Workshop*, volume 2009, 2009.

Y.K. Chan and V.C. Koo. An introduction to synthetic aperture radar (SAR). *Progress In Electromagnetics Research B*, 2: 27–60, 2008.

C.W. Chen and H.A. Zebker. Phase unwrapping for large SAR interferograms: statistical segmentation and generalized network models. *IEEE Transactions on Geoscience and Remote Sensing*, 40(8): 1709–1719, 2002.

J. Chen and H.A. Zebker. Ionospheric Artifacts in Simultaneous L-Band InSAR and GPS Observations. *IEEE Transactions on Geoscience and Remote Sensing*, 50(4): 1227–1239, 2012.

J. Chen and H.A. Zebker. Reducing Ionospheric Effects in InSAR Data Using Accurate Coregistration. *IEEE Transactions on Geoscience and Remote Sensing*, pages 1–11, 2013.

K.M. Cuffey and W.S.B. Paterson. *The Physics of Glaciers*. 2010. ISBN 9780123694614.

F. De Zan. Accuracy of incoherent Speckle Tracking for Circular Gaussian Signals. *IEEE Geoscience and Remote Sensing Letters*, 2, 2013.

Delft Institute of Earth Observation (DEOS) and Space Systems. DORIS - Delft Object-oriented Radar Interferometric Software - User manual and technical documentation.

K.G. Derpanis. Cramer-Rao Bound. 2006.

E. Erten, A. Reigber, and O. Hellwich. Generation of three-dimensional deformation maps from InSAR data using spectral diversity techniques. *ISPRS Journal of Photogrammetry and Remote Sensing*, 65 (4):388–394, 2010.

A. Ferretti, A. Monti-Guarnieri, and C. Prati. *InSAR Principles - Guidelines for SAR Interferometry Processing and Interpretation*. Number February. 2007. ISBN 9290922338.

A. Fischer, H. Rott, and H. Björnsson. Observation of recent surges of Vatnajokull, Iceland, by means of ERS SAR interferometry. *Annals of Glaciology*, 37:69–76, 2003.

U.H. Fischer and G.K.C. Clarke. Review of subglacial hydro-mechanical coupling: Trapridge Glacier, Yukon Territory, Canada. *Quaternary International*, 86(1):29–43, 2001.

R.M. Goldstein and C.L. Werner. Radar Interferogram Filtering for Geophysical Applications. *Geophysical Research Letters*, 1998.

R.M. Goldstein, H. Engelhardt, B. Kamb, and R.M. Frolich. Satellite Radar Interferometry for Monitoring Ice-sheet Motion: Application to an Antarctic Ice Stream. *Science*, 262:1525–1530, 1993.

N. Gourmelen, S.W. Kim, A. Shepherd, J.W. Park, A.V. Sundal, H. Björnsson, and F. Pálsson. Ice velocity determined using conventional and multiple-aperture InSAR. *Earth and Planetary Science Letters*, 307(1-2):156–160, 2011.

A.L. Gray and K.E. Mattar. InSAR results from the RADARSAT Antarctic Mapping Mission data: estimation of glacier motion using a simple registration procedure. In *Geoscience and Remote Sensing Symposium Proceedings (IGARSS)*, number 1, pages 0–2, 1998. ISBN 0780344030.

A.L. Gray, K.E. Mattar, and G. Sofko. Influence of Ionospheric Electron Density Fluctuations on Satellite Radar Interferometry. *Geophysical Research Letters*, 27 (10):1451–1454, 2000.

A.L. Gray, N. Short, K.E. Mattar, and K.C. Jezek. Velocities and Flux of the Filchner Ice Shelf and its Tributaries determined from Speckle Tracking Interferometry. *Canadian Journal of Remote Sensing*, (613):193–206, 2001.

L. Gray, K.E. Mattar, and N. Short. Speckle Tracking for 2-Dimensional Ice Motion Studies in Polar Regions: Influence of the Ionosphere. In *Proceedings of the ESA Fringe meeting*, 1999.

S. Gudmundsson. Three-dimensional glacier surface motion maps at the Gjálp eruption site, Iceland, inferred from combining InSAR and other ice-displacement data. *Annals of Glaciology*, (34):315–322, 2002.

J.O. Hagberg, L.M.H. Ulander, and J. Askne. Repeat-pass SAR interferometry over forested terrain. *IEEE Transactions on Geoscience and Remote Sensing*, 33(2), 1995.

R.F. Hanssen. *Radar Interferometry: Data Interpretation and Error Analysis*. Kluwer Academic Publishers, Dordrecht, The Netherlands, 2001.

A.J. Hooper, D. Bekaert, K.H. Spaans, and M. ArÄśkan. Recent advances in SAR interferometry time series analysis for measuring crustal deformation. *Tectonophysics*, 514-517:1–13, 2012.

J. Hu, Z.W. Li, X.L. Ding, J.J. Zhu, L. Zhang, and Q. Sun. 3D coseismic Displacement of 2010 Darfield, New Zealand earthquake estimated from multi-aperture InSAR and D-InSAR measurements. *Journal of Geodesy*, 86(11):1029–1041, 2012a.

J. Hu, Z.W. Li, L. Zhang, X.L. Ding, J.J. Zhu, Q. Sun, and W. Ding. Correcting ionospheric effects and monitoring two-dimensional displacement fields with multiple-aperture InSAR technology with application to the Yushu earthquake. *Science China Earth Sciences*, 55 (12):1961–1971, 2012b.

I.R. Joughin. Ice-sheet velocity mapping: a combined interferometric and speckle-tracking approach. *Annals of Glaciology*, 34(1):195–201, 2002.

I.R. Joughin, R. Kwok, and M.A. Fahnestock. Estimation of ice-sheet motion using satellite radar interferometry: method and error analysis with application to Humboldt Glacier, Greenland. *Journal of Glaciology*, 42(142):564–575, 1996.

I.R. Joughin, R. Kwok, and M.A. Fahnestock. Interferometric Estimation of Three-Dimensional Ice-Flow Using Ascending and Descending Passes. *IEEE Transactions on Geoscience and Remote Sensing*, 36(1):25–37, 1998.

I.R. Joughin, B.E. Smith, and W. Abdalati. Glaciological advances made with interferometric synthetic aperture radar. *Journal of Glaciology*, 56(200):1026–1042, 2010.

H.S. Jung, J.S. Won, and S.W. Kim. An Improvement of the Performance of Multiple-Aperture SAR interferometry (MAI). *IEEE Transactions on Geoscience and Remote Sensing*, 47(8):2859–2869, 2009.

H.S. Jung, D.T. Lee, Z. Lu, and J.S. Won. Ionospheric Correction of SAR Interferograms by Multiple-Aperture Interferometry. *IEEE Transactions on Geoscience and Remote Sensing*, 2012.

H.S. Jung, Z. Lu, and L. Zhang. Feasibility of Along-Track Displacement Measurement From Sentinel-1 Interferometric Wide-Swath Mode. *IEEE Transactions on Geoscience and Remote Sensing*, 51(1): 573–578, 2013.

B. Kamb. Glacier surge mechanism based on linked cavity configuration of the basal water conduit system. *Journal of Geophysical Research*, 92(6):9083–9100, 1987.

B.M. Kampes, R.F. Hanssen, and Z. Perski. Radar interferometry with public domain tools. *Proceedings of FRINGE*, (2), 2003.

R. Kwok and M.A. Fahnestock. Ice sheet motion and topography from radar interferometry. *IEEE Transactions on Geoscience and Remote Sensing*, 34(1):189–200, 1996.

F. Li, G. Zhang, and J. Yan. Coregistration based on SIFT algorithm for Synthetic Aperture Radar Interferometry. In *XXXVII - International Society for Photogrammetry and Remote Sensing*, pages 123–128, 2008.

H. Liu and K.C. Jezek. Automated extraction of coastline from satellite imagery by integrating Canny edge detection and locally adaptive thresholding methods. *International Journal of Remote Sensing*, 25 (5):937–958, 2004.

D.G. Lowe. Object recognition from local scale-invariant features. *Proceedings of the*

Seventh IEEE International Conference on Computer Vision, pages 1150–1157 vol.2, 1999.

S.N. Madsen, H.A. Zebker, and J.M. Martin. Topographic mapping using radar interferometry: Processing techniques. *IEEE Transactions on Geoscience and Remote Sensing*, 31(1):246–256, 1993.

E. Magnússon. *Glacier hydraulics explored by means of SAR-interferometry*. PhD thesis, Leopold-Franzens Universität Innsbruck, 2008.

E. Magnússon, H. Björnsson, H. Rott, and F. Pálsson. Reduced glacier sliding caused by persistent drainage from a subglacial lake. *The Cryosphere*, (November 1996):13–20, 2010.

E. Magnússon, H. Björnsson, H. Rott, M.J. Roberts, F. Pálsson, S. Gudmundsson, R.A. Bennett, H. Geirsson, and E. Sturkell. Localized uplift of Vatnajokull, Iceland: subglacial water accumulation deduced from InSAR and GPS observations. *Journal of Glaciology*, 57 (203):475–484, 2011.

K.E. Mattar and P.W. Vachon. Validation of alpine glacier velocity measurements using ERS tandem-mission SAR data. *IEEE Transactions on Geoscience and Remote Sensing*, 36(3):974–984, 1998.

T. Meierbachtol, J. Harper, and N. Humphrey. Basal drainage system response to increasing surface melt on the Greenland ice sheet. *Science (New York, N.Y.)*, 341(6147):777–9, 2013.

N. Metropolis, A. W. Rosenbluth, M. N Rosenbluth, and A. H. Teller. Equation of State Calculations by Fast Computing Machines. *Journal of Chemical Physics*, 21 (6):1087–1092, 1953.

F. Meyer. A review of ionospheric effects in low-frequency SAR âĂŤ Signals, correction methods, and performance requirements. *2010 IEEE International Geoscience and Remote Sensing Symposium*, pages 29–32, 2010.

R. Michel, J.P. Avouac, and J. Taboury. Measuring ground displacements from SAR amplitude images: application to the Landers earthquake. *Geophysical Research Letters*, 1999.

J.J. Mohr and S.N. Madsen. Multi-pass interferometry for studies of glacier dynamics. In *Proceedings of the ESA Fringe '96 meeting*, pages 345–352, 1996.

J.J. Mohr, N. Reeh, and S.N. Madsen. Three-dimensional glacial flow and surface elevation measured with radar interferometry. *Nature*, 1984:273–276, 1998.

A. Monti-Guarnieri and C. Prati. An interferometric quick-look processor. *IEEE Transactions on Geoscience and Remote Sensing*, 37(2):861–866, 1999.

A. Moreira and R. Scheiber. A New Method for Accurate Co-Registration of Interferometric SAR Images. *IEEE Transactions on Geoscience and Remote Sensing*, pages 1091–1093, 1998.

NASA Land Processes Distributed Active Archive Center (LP DAAC). AsterDEM V2, 2001.

F. Pálsson, E. Magnússon, and H. Björnsson. The surge of Dyngjujökull 1997-2000 Mass transport, ice flow velocities, and effects on mass balance and runoff. Technical report, 2002.

P. Prats, A. Reigber, and J.J. Mallorqui. Interpolation-Free Coregistration and Phase-Correction of Airborne SAR Interferograms. *IEEE Geoscience and Remote Sensing Letters*, 1(3):188–191, 2004.

P. Prats, C. Andres, R. Scheiber, K.A. Camara de Macedo, J. Fischer, and A. Reigber. Glacier displacement field estimation using airborne SAR interferometry. *IEEE Transactions on Geoscience and Remote Sensing*, pages 2098–2101, 2007.

C.F. Raymond. How do glaciers surge? A review. *Journal of Geophysical Research*, 92 (1):9121–9134, 1987.

N. Reeh, S.N. Madsen, and J.J. Mohr. Combining SAR interferometry and the equation of continuity to estimate the three-dimensional glacier surface-velocity vector. *Journal of Glaciology*, 45(151):533–538, 1999.

N. Reeh, J.J. Mohr, S.N. Madsen, H. Oerter, and N.S. Gundestrup. Three-dimensional surface velocities of Storstrommen glacier, Greenland, derived from radar interferometry and ice-sounding radar measurements. *Journal of Glaciology*, 49(165):201–209, 2003.

W.G. Rees. *Physical Principles of Remote Sensing*, volume 37. 2001. ISBN 0521669480.

E. Rignot. Tidal motion, ice velocity and melt rate of Petermann Gletscher, Greenland, measured from radar interferometry. *Journal of Glaciology*, 42:476–485, 1996.

E. Rignot, J.L. Bamber, M.R. van den Broeke, C. Davis, Y. Li, W.J. van de Berg, and E. van Meijgaard. Recent Antarctic ice mass loss from radar interferometry and regional climate modelling. *Nature Geoscience*, 1(2):106–110, 2008.

F. Rocca. Perspectives of Sentinel-1 for InSAR applications. In *Proceedings for IGARRS 2012*, pages 3–5, 2012.

E. Rodriguez and J.M. Martin. Theory and Design of Interferometric Synthetic Aperture Radars. *IEE Proceedings F*, 139 (2):147–159, 1992.

P.A. Rosen, S. Hensley, I.R. Joughin, F.K. Li, S.N. Madsen, E. Rodriguez, and R.M. Goldstein. Synthetic Aperture Radar Interferometry. *Proceedings of the IEEE*, 88 (3):333–382, 2000.

P.A. Rosen, S. Hensley, G. Peltzer, and M. Simons. Updated Repeat Orbit Interferometry Package Released. *Eos, Transactions American Geophysical Union*, 85(5): 47, 2004.

R. Scheiber and A. Moreira. Improving Co-Registration Accuracy of Interferometric SAR Images using Spectral Diversity. *IEEE Transactions on Geoscience and Remote Sensing*, 1999.

R. Scheiber and A. Moreira. Coregistration of interferometric SAR images using spectral diversity. *IEEE Transactions on Geoscience and Remote Sensing*, 38(5): 2179–2191, 2000.

J. Shi and C. Tomasi. Good Features to Track. In *IEEE Conference on CVPR'94*, number June, 1994.

T. Strozzi, A. Luckman, and T. Murray. The Evolution of a Glacier Surge observed with the ERS Satellites. In *ERS-Envisat Symposium*, number September 1991, 2000.

C. Tomasi and T. Kanade. Detection and Tracking of Point Features. Technical Report April, 1991.

F.P. De Vries. Speckle reduction in SAR Imagery by various multi-look techniques. Technical report, TNO, 1998.

B. Wangensteen, D.J. Weydahl, and J.O. Hagen. Mapping Glacier Velocities at Spitsbergen Using ERS Tandem SAR Data. In *Geoscience and Remote Sensing Symposium (IGARSS) proceedings*, 1999.

U. Wegmuller, C.L. Werner, T. Strozzi, and A. Wiesmann. Ionospheric electron concentration effects on SAR and INSAR. *IEEE Transactions on Geoscience and Remote Sensing*, pages 3714–3717, 2006.

T.J. Wright. Toward mapping surface deformation in three dimensions using InSAR. *Geophysical Research Letters*, 31(1), 2004.

J. Yang, P. Gong, R. Fu, M. Zhang, J. Chen, S. Liang, B. Xu, J. Shi, and R. Dickinson. The role of satellite remote sensing in climate change studies. *Nature Climate Change*, 3(10):875–883, 2013.

H.A. Zebker and J. Villasenor. Decorrelation in Interferometric Radar Echoes. *IEEE Transactions on Geoscience and Remote Sensing*, 30(5):950–959, 1992.

H.A. Zebker, T.G. Farr, R.P. Salazar, and T.H. Dixon. Mapping the World's Topography Using Radar Interferometry: The TOPSAT Mission. In *Proceedings of the IEEE*, volume 82, pages 1774–1786, 1994a.

H.A. Zebker, C.L. Werner, P.A. Rosen, and S. Hensley. Accuracy of Topographic Maps Derived from ERS-1 Interferometric Radar. *IEEE Transactions on Geoscience and Remote Sensing*, 1(4):823–836, 1994b.

Appendix A

Rewrapped interferograms derived from ascending data

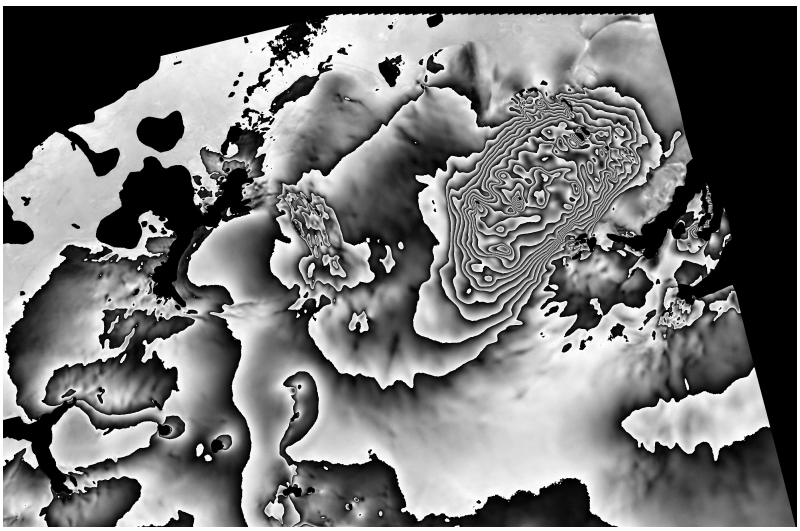

Figure 1: Rewrapped interferogram of datapair 6/7 January 1999, derived by Eyjólfur Magnússon.

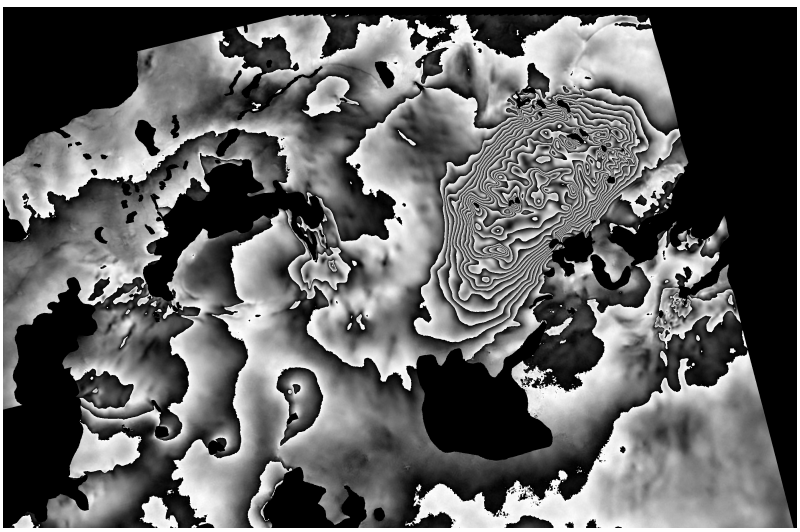

Figure 2: Rewrapped interferogram of datapair 10/11 Febuary 1999, derived by Eyjólfur Magnússon.

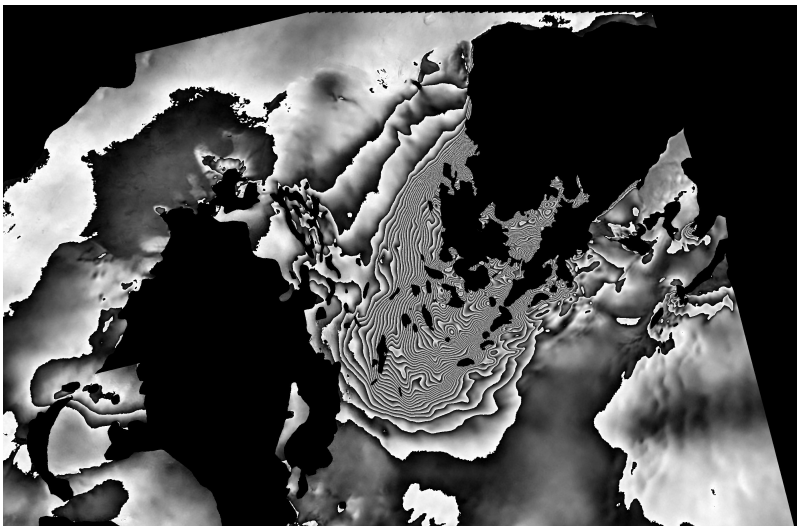

Figure 3: Rewrapped interferogram of datapair 26/27 January 2000, derived by Eyjólfur Magnússon.

Appendix B
Example of DORIS inputfile

```
c *****************************************************************
c * 11/2013 JELTE VAN OOSTVEEN - 19990106_07
c *****************************************************************
c
# comment  ___general options___
c
c SCREEN          debug                 // level of output to standard out
SCREEN          info                    // level of output to standard out
MEMORY          1024                    // MB
BEEP            error                   // level of beeping
OVERWRITE       ON                      // overwrite existing files
BATCH           OFF                     // non-interactive
PREVIEW         OFF                     // prevents copy of this file to log
c
PROCESS         M_SIMAMP
PROCESS         M_TIMING
PROCESS         COARSEORB               // no cards later
PROCESS         COARSECORR              // based on correlation
PROCESS         M_FILTAZI
PROCESS         S_FILTAZI
PROCESS         FINE                    // fine coregistration
PROCESS         RELTIMING               // relative timing error master-slave
PROCESS         DEMASSIST               // DEM assisted coregistration
PROCESS         COREGPM                 // estimate coregistration param.
PROCESS         RESAMPLE                // slave
PROCESS         INTERFERO
PROCESS         COMPREFPHA              // estimate flatearth param.
PROCESS         SUBTRREFPHA
PROCESS         COMPREFDEM              // synthetic phase from DEM
PROCESS         SUBTRREFDEM
PROCESS         COHERENCE
c
c
# comment  ___the general io files___
c
LOGFILE         log.out                 // log file
M_RESFILE       master.res              // parameter file
S_RESFILE       slave.res               // parameter file
I_RESFILE       parameter.out           // parameter file
c
c
# comment ___SIMAMP___
c
SAM_IN_FORMAT    i2
SAM_IN_DEM       /home/jvanoostveen/processing/RAW_offset/november2013/19990106_07
    /2/DEM/vatnaj99_final_qgis_-32768.tif
SAM_IN_SIZE      9612 23401
SAM_IN_DELTA     0.000277781462423 0.000277767247790
SAM_IN_UL        66.000200492217772 -20.000146197884821
SAM_IN_NODATA    -32768
SAM_OUT_FILE     master_sam.raw
SAM_OUT_DEM      dem_sam.raw
c
c
# comment ___COMPUTE MASTER TIMING ERROR___
c
MTE_METHOD      magfft                  // computes faster than magspace
MTE_NWIN        100                     // number of large windows
```

```
MTE_INITOFF     0 0                     // initial offset
MTE_WINSIZE     1024 512                // rectangular window
c
c
# comment ___COARSE CORR (COREGISTRATION)___
c
CC_METHOD       magfft                  // default
CC_NWIN         100                     // number of windows
CC_WINSIZE      1024 256                // size of windows
CC_INITOFF      orbit                   // use result of orbits for initial offset
c
c
# comment ___AZIMUTH FILTERING___
c
AF_BLOCKSIZE    1024
AF_OVERLAP      64
AF_HAMMING      1
AF_OUT_MASTER   master_afilt.slc
AF_OUT_SLAVE    slave_afilt.slc
AF_OUT_FORMAT   cr4
c
c
# comment ___FINE COREGISTRATION___
c
FC_METHOD       oversample
FC_NWIN         8000                    // number of windows
FC_IN_POS       window_pos_resample     // file containing position of windows
FC_WINSIZE      32 32                   // size of windows
FC_ACC          8 8                     // search window, 2^n
FC_INITOFF      coarsecorr              // use result of coarse to compute first
FC_OSFACTOR     32                      // oversampling factor
c
c
# comment ___REL TIMING ERROR___
c
RTE_THRESHOLD   0.4
RTE_MAXITER     10000
RTE_K_ALPHA     1.97
c
c
# comment ___DEM ASSISTED COREGISTRATION___
c
DAC_IN_DEM      /home/jvanoostveen/processing/RAW_offset/november2013/19990106_07
    /2/DEM/vatnaj99_final_qgis_-32768.tif
DAC_IN_FORMAT   i2
DAC_IN_SIZE     9612 23401
DAC_IN_DELTA    0.000277781462423 0.000277767247790
DAC_IN_UL       66.000200492217772 -20.000146197884821
DAC_IN_NODATA   -32768
DAC_OUT_DEM     dem_dac.raw
DAC_OUT_DEMI    demi_dac.raw
DAC_OUT_DEM_LP  demLP_dac.raw
c
c
# comment ___COMPUTE COREGISTRATION PARAMETERS___
c
CPM_THRESHOLD   0.4
CPM_DEGREE      2
CPM_WEIGHT      bamler
CPM_MAXITER     8000
c
c
# comment ___RESAMPLING SLAVE___
c
RS_METHOD       rc12p
RS_OUT_FILE     slave_resampled.slc
RS_OUT_FORMAT   cr4
c
c
# comment ___INTERFEROGRAM___
c
```

```
INT_OUT_CINT    ifg.raw                 // optional complex int.
INT_MULTILOOK   1 1                     // line, pixel factors
c
c
# comment ___REFERENCE PHASE COMPUTATION___
c
FE_METHOD       porbits
FE_DEGREE       3
FE_NPOINTS      201
c
c
# comment ___SUBTRACT REFERENCE PHASE___
c
SRP_METHOD      polynomial              // evaluate comprefpha poly
SRP_OUT_CINT    ifg.minrefpha.raw
c
c
# comment ___REFERENCE DEM___
c
CRD_INCLUDE_FE   OFF
CRD_OUT_FILE     refdem_1l.raw
CRD_OUT_DEM_LP   dem_radar.raw
CRD_IN_FORMAT    i2
CRD_IN_DEM       /home/jvanoostveen/processing/RAW_offset/november2013/19990106_07
    /2/DEM/vatnaj99_final_qgis_-32768.tif
CRD_IN_SIZE      9612 23401
CRD_IN_DELTA     0.000277781462423 0.000277767247790
CRD_IN_UL        66.000200492217772 -20.000146197884821
CRD_IN_NODATA    -32768
c
c
# comment ___SUBTRREF DEM___
c
SRD_OUT_CINT    ifg.minrefdem.raw
SRD_OFFSET       0 0                    // az,rg +ve shifts dem down and right
c
c
# comment ___COHERENCE___
c
COH_METHOD      include_refdem          // remove topographic phase also.
COH_OUT_COH     master_slave.coh        // optional real
COH_OUT_CCOH    master_slave.ccoh       // optional complex image
COH_MULTILOOK   1 1                     // same as interferogram
COH_WINSIZE     10 2                    // estimator window size
c
STOP
```

Appendix C
Example of DORIS speckle inputfile

```
# ******************************************************************
# ***   JELTE VAN OOSTVEEN
# ***   11-2013
# ******************************************************************

# comment  ___general options___

SCREEN          info                    // level of output to standard out
c SCREEN          debug                 // level of output to standard out
c SCREEN          error                 // level of output to standard out
MEMORY          1024                    // MB
BEEP            error                   // level of beeping
OVERWRITE       ON                      // overwrite existing files
BATCH           ON                      // non-interactive
LISTINPUT       ON                      // prevents copy of this file to log
HEIGHT          0.0
TIEPOINT        0.0 0.0 0.0
ORB_INTERP      POLYFIT 4
c
PROCESS         FINE
c
# comment  ___the general io files___
LOGFILE         speckle_new.log         // log file
M_RESFILE       master.res              // parameter file
S_RESFILE       slave.res               // parameter file
I_RESFILE       speckle_new.res         // parameter file
c
c
# comment ___FINE COREGISTRATION___
c
FC_METHOD       magspace                // ICC
c FC_NWIN         100000                // nr of randomly chosen windows
FC_IN_POS       window_pos_speckle      // window positions (make_speckle_input.m)
FC_OSFACTOR     1                       // no oversampling
FC_WINSIZE      32 32                   // size of windows
c
STOP
```

This thesis was typeset in LaTeX using Latexian 1.2.4.
All Figures, except when clearly stated, were created by the author.